Max-Planck-Institut
für Meteorologie

MAX-PLANCK-GESELLSCHAFT

International Max Planck Research School
on Earth System Modelling

The influence of precipitation and convective organization on the structure of the trades

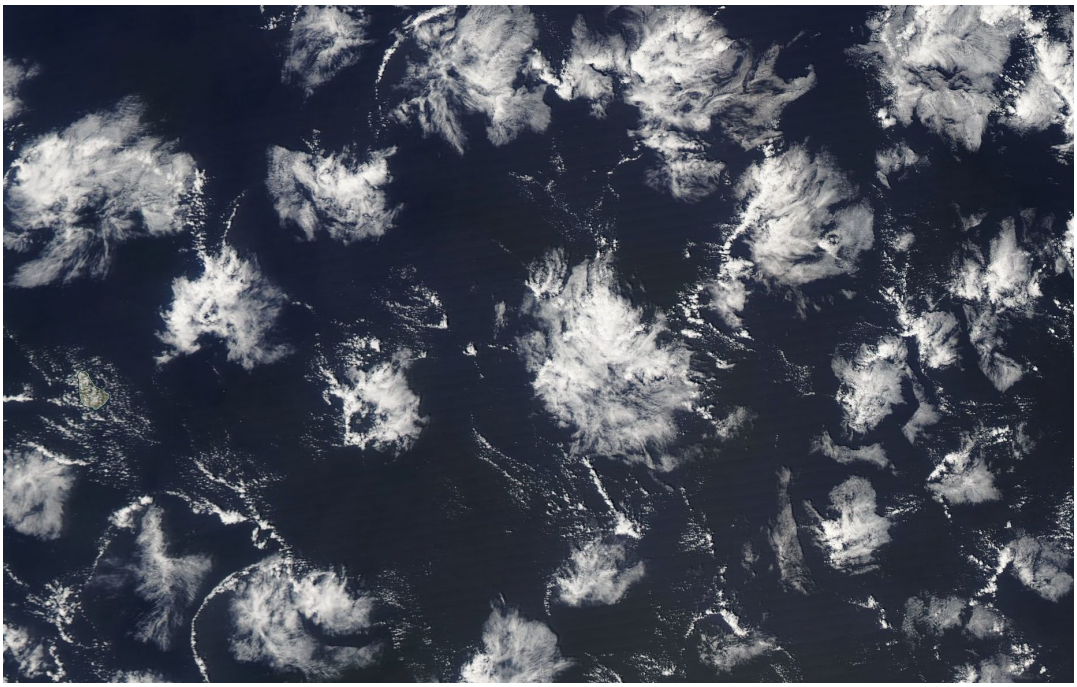

Raphaela Vogel

Hamburg 2017

Berichte zur Erdsystemforschung
Reports on Earth System Science

199
2017

Hinweis

Die Berichte zur Erdsystemforschung werden vom Max-Planck-Institut für Meteorologie in Hamburg in unregelmäßiger Abfolge herausgegeben.

Sie enthalten wissenschaftliche und technische Beiträge, inklusive Dissertationen.

Die Beiträge geben nicht notwendigerweise die Auffassung des Instituts wieder.

Die "Berichte zur Erdsystemforschung" führen die vorherigen Reihen "Reports" und "Examensarbeiten" weiter.

Notice

The Reports on Earth System Science are published by the Max Planck Institute for Meteorology in Hamburg. They appear in irregular intervals.

They contain scientific and technical contributions, including Ph. D. theses.

The Reports do not necessarily reflect the opinion of the Institute.

The "Reports on Earth System Science" continue the former "Reports" and "Examensarbeiten" of the Max Planck Institute.

Anschrift / Address

Max-Planck-Institut für Meteorologie
Bundesstrasse 53
20146 Hamburg
Deutschland

Tel./Phone: +49 (0)40 4 11 73 - 0
Fax: +49 (0)40 4 11 73 - 298

name.surname@mpimet.mpg.de
www.mpimet.mpg.de

Layout

Bettina Diallo and Norbert P. Noreiks
Communication

Copyright

Photos below: ©MPI-M
Photos on the back from left to right:
Christian Klepp, Jochem Marotzke,
Christian Klepp, Clotilde Dubois,
Christian Klepp, Katsumasa Tanaka

The influence of precipitation and convective organization on the structure of the trades

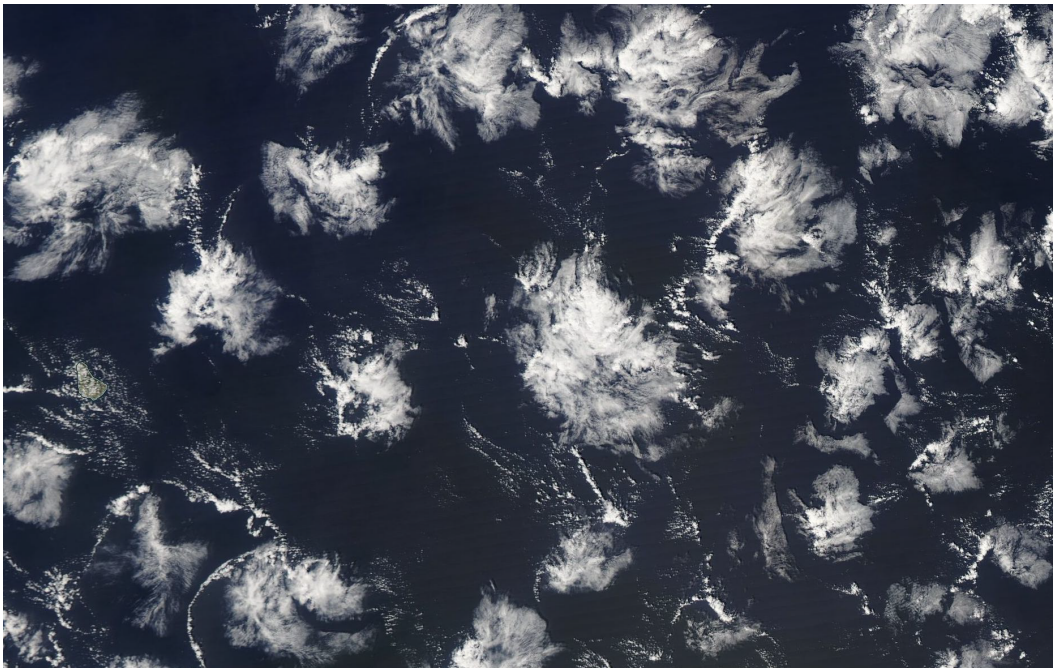

Dissertation with the aim of achieving a doctoral degree
at the Faculty of Mathematics, Informatics and Natural Sciences
Department of Earth Sciences of Universität Hamburg

submitted by

Raphaela Vogel

Hamburg 2017

Raphaela Vogel

Max-Planck-Institut für Meteorologie
Bundesstrasse 53
20146 Hamburg

Tag der Disputation: 19.06.2017

Folgende Gutachter empfehlen die Annahme der Dissertation:

Prof. Dr. Stefan Buehler
Dr. Louise Nuijens

Berichte zur Erdsystemforschung / Max-Planck-Institut für Meteorologie 199
Reports on Earth System Science / Max Planck Institute for Meteorology 2017

ISSN 1614-1199

Title image: open sharing by NASA Worldview

Abstract

This thesis investigates the influence of precipitation and shallow-convective organization on cloudiness and the thermodynamic structure in the trade-wind shallow cumulus regime by combining large-eddy simulations (LES) and ground-based observations from the Barbados Cloud Observatory (BCO).

In large-domain LES, precipitation limits the deepening of the trade-wind layer and induces the spontaneous organization of shallow convection into deeper and larger cloud clusters. Substantial precipitation and compensating subsidence induced by the deeper clusters leads to a shallower and drier trade-wind layer with a 33% relative decrease in cloud cover compared to a small-domain simulation without organization.

Numerical experiments are performed to explore how the organization and deepening of precipitating shallow convection modulates the response to forcing perturbations representative for climate change and the seasonal cycle. Under a uniform 4 K warming at constant relative humidity, cloud cover decreases slightly in all simulations independent of precipitation or shallow-convective organization. Cloud cover decreases in precipitating simulations because updrafts become more concentrated and because the weaker inversion reduces stratiform layers near cumulus tops. Overall the changes are small, owing to the robustness of cloud fractions near cumulus bases to the climate-change like perturbation.

The deepening of shallow convection in a summer-like simulation with 2 K larger sea-surface temperature and 20% weaker large-scale subsidence increases precipitation but weakens the inversion and reduces cloud cover compared to a winter-like simulation, resembling the observed seasonal changes at Barbados. The cloud layer in the winter-like simulation remains shallow and maintains a strong inversion with stratiform outflow layers. The thin stratiform layers develop when slightly deeper cloud clusters detrain condensate into the inversion layer, and strong long-wave cooling at cloud tops stabilizes the inversion and maintains saturation. Once sustained deeper convection weakens the inversion—for example in response to stronger winds, horizontal advective cooling, or under a drier free troposphere—the stratiform layers cease to develop, and cloud cover decreases.

BCO observations demonstrate that signatures of shallow-convective organization, as identified by cold pools, are present at Barbados on 70% of the days. Cold pools with stronger temperature drops are associated with higher precipitation frequencies, deeper clouds, a more well-mixed vertical humidity structure, and slightly lower cloud cover in the front compared to cold pools with weaker temperature drops. Although cloud cover decreases after a maximum at the cold-pool onset, cloud cover in the hour after the frontal passage remains strongly enhanced compared to the 5-year mean. The frequency with which cold pools are present highlights the relevance of precipitation and convective organization for the trades.

Zusammenfassung

Diese Dissertation untersucht den Einfluss von Niederschlag und der Organisation von flacher Konvektion auf die Bewölkung und die thermodynamische Schichtung in der Passatwindzone mithilfe von hochauflösenden Simulationen und Beobachtungen des Wolkenobservatoriums auf Barbados.

In Simulationen auf grossem Rechengebiet verringert die Niederschlagsbildung die Höhe der Wolkenschicht und induziert die Organisation der flachen Konvektion in grössere und tiefere Wolkencluster. Durch grosse Niederschlagsmengen und kompensierende Absinkbewegung von trockener Luft aus höherliegenden Schichten führen die tieferen Wolkencluster zu einer flacheren und trockeneren atmosphärischen Grenzschicht. Diese weist einen 33 % kleineren Wolkenbedeckungsgrad auf als eine vergleichbare Simulation auf kleinerem Rechengebiet, in welcher sich keine tiefen Wolkencluster bilden.

Als Reaktion auf eine uniforme Erwärmung der Atmosphäre von 4 K bei gleichbleibender relativer Feuchtigkeit verringert sich die Wolkenbedeckung unabhängig von Niederschlag und konvektiver Organisation. Die Wolkenbedeckung verringert sich aufgrund der schwächeren Passatinversion, welche den Anteil von stratiformer Bewölkung an der Wolkenoberkante verkleinert, und aufgrund sich zusammenziehender Auftriebskerne. Da sich aber die Bewölkung an der Wolkenunterkante nicht stark verändert, bleibt der Einfluss dieser für den Klimawandel repräsentativen Störung auf die Wolkenbedeckung relativ gering.

Das Tieferwerden der Konvektion in einer Simulation mit 2 K grösserer Meeresoberflächentemperatur und 20 % schwächerer grossskaligen Absinkrate (angelehnt an die Bedingungen im Sommer) führt zu stärkerem Niederschlag, aber auch zu einer schwächeren Inversion und geringeren Wolkenbedeckung im Vergleich zur Kontrollsimulation. Die Konvektion in der für den Winter charakteristischen Kontrollsimulation bleibt hingegen flach und behält eine starke Inversion mit stratiformer Bewölkung bei. Die dünnen stratiformen Wolkenschichten entstehen wenn Wolkenkondensat von grossen Wolkenclustern an der starken Inversion lateral ausströmt. Grosse Abkühlungsraten durch das Aussenden von langwelliger Strahlung an der Wolkenoberkante erhalten die Luftsättigung und verlängern die Lebenszeit der stratiformen Wolkenschichten. Anhaltende tiefere Konvektion—zum Beispiel als Reaktion auf stärkere Winde, Kaltluftadvektion oder eine trockenere freie Troposphäre—schwächt die Inversion und verhindert die Entstehung von stratiformer Bewölkung, wodurch der Bewölkungsgrad abnimmt.

Die Organisation von flacher Konvektion, identifiziert durch das Auftreten von konvektiven Kaltluftfronten in Bodenmessdaten auf Barbados, tritt an 70 % der analysierten Tage auf. Kaltluftfronten mit einer stärkeren Verringerung der Oberflächentemperatur gehen einher mit häufigerem Niederschlag, tieferen Wolken, einer stärker durchmischten ver-

tikalen Feuchtigkeitsstruktur und einer etwas reduzierten Wolkenbedeckung im Vergleich zu schwächeren Kaltluftfronten. Obwohl die Bewölkung nach einem Maximum zu Beginn der Kaltluftfront etwas abnimmt, bleibt die Bewölkung in der Stunde nach dem Frontdurchgang stark erhöht zum 5-jährigen Mittelwert. Das häufige Auftreten konvektiver Kaltluftfronten unterstreicht die Bedeutung von Niederschlag und konvektiver Organisation für die Passatwindzone.

Contents

Abstract I

Zusammenfassung III

1. Introduction 1
- 1.1. Trade-wind layer structure . . . 2
- 1.2. Precipitating shallow convection and its organization . . . 3
- 1.3. Large-scale cloud-controlling factors . . . 6
- 1.4. Research questions and strategy . . . 8

2. The role of precipitation and spatial organization in the response of trade-wind clouds to warming 9
- 2.1. Introduction . . . 10
- 2.2. Large-Eddy Simulation . . . 11
  - 2.2.1. LES Code . . . 12
  - 2.2.2. Model Setup and Experiment Design . . . 12
- 2.3. The Importance of Precipitation for Attaining an Equilibrium . . . 14
- 2.4. How Precipitation Modulates the Warming Response . . . 19
  - 2.4.1. Non-precipitating warming response . . . 20
  - 2.4.2. Precipitating warming response . . . 21
- 2.5. Impact of Deeper Convection . . . 23
  - 2.5.1. Influence of Deeper Convection on the Trade-Wind Layer Structure 23
  - 2.5.2. Warming Response . . . 29
- 2.6. Conclusions . . . 30

3. Changes in precipitation, cloudiness and trade-wind layer structure from the winter to the summer trades 33
- 3.1. Introduction . . . 34

3.2. Large-eddy simulation framework and experiments . . . 36
3.2.1. LES framework . . . 36
3.2.2. Numerical experiments . . . 37
3.3. Range of precipitation and cloud cover responses . . . 40
3.4. Sensitivity to large-scale forcings, initial and boundary conditions . . . 44
3.4.1. How drier atmospheres tend to precipitate more: the influence of radiation . . . 44
3.4.2. Enhanced precipitation and cloudiness in response to stronger surface forcing . . . 51
3.4.3. Larger subsidence can limit precipitation, but not necessarily the depth of the moist layer . . . 54
3.5. Conclusions . . . 57

4. Statistics of spatial organization as identified by cold pools 61
4.1. Introduction . . . 61
4.2. Data and Methods . . . 63
4.2.1. Data sources . . . 63
4.2.1.1. Surface meteorology data . . . 63
4.2.1.2. KATRIN cloud radar . . . 64
4.2.1.3. Ceilometer . . . 64
4.2.1.4. Raman lidar . . . 65
4.2.1.5. MRR . . . 65
4.2.2. Cold-pool detection algorithm . . . 65
4.3. Example cases . . . 66
4.3.1. 15 February 2012 . . . 66
4.3.2. 19 March 2013 . . . 69
4.4. Cold-pool statistics . . . 72
4.4.1. General statistics . . . 72
4.4.2. Temporal structure . . . 74
4.4.2.1. Cloudiness . . . 75
4.4.2.2. Vertical humidity structure . . . 80
4.5. Conclusions . . . 82

5. Conclusions 85

Appendix 89
A. Development of Deep Convection in the Absence of Cold Pools . . . 89
B. Robustness and uncertainties of LES studies . . . 94

Bibliography VII

Chapter 1

Introduction

Steady easterlies and extensive fields of shallow 'trade-wind' cumulus clouds characterize the trades. Shallow trade-wind cumuli play an important role in the climate system, both by reflecting solar radiation and by mixing heat, moisture and momentum throughout the trade-wind layer. The moisture and heat fluxes associated with shallow convection maintain the thermodynamic structure of the lower troposphere, and balance the tendencies due to large-scale advection and radiation (*Riehl et al.*, 1951; *Riehl and Malkus*, 1957; *Malkus*, 1958).

While the early motivation for studying shallow convection in the trades stems mostly from its influence on the atmospheric energy cycle, in the last decades the focus has changed towards its influence on Earths radiation budget and its response to climate change. Differing responses of low clouds to warming in regions of moderately subsiding and rising motion are the major cause of the spread in predicted climate sensitivity (e.g. *Bony et al.*, 2004; *Bony and Dufresne*, 2005; *Vial et al.*, 2013; *Boucher et al.*, 2013; *Brient and Schneider*, 2016). There is increasing evidence that the strength of low-cloud feedbacks depends on the strength of lower-tropospheric mixing by shallow convection (*Rieck et al.*, 2012; *Sherwood et al.*, 2014; *Zhao*, 2014; *Brient et al.*, 2015). Climate models with stronger convective mixing efficiently dry the trade-wind layer with warming, which leads to a reduced low-level cloudiness and a higher climate sensitivity (*Sherwood et al.*, 2014). How much a stronger convective mixing with warming reduces low clouds depends both on the coupling of surface latent heat fluxes with convective mixing and low-cloud radiative effects (*Vial et al.*, 2016), and on the present-day vertical distribution of low clouds (*Brient et al.*, 2015). Models with large cloud fractions only near the base of the cumulus layer tend to reduce cloudiness more strongly with warming, and have a higher climate sensitivity

(*Brient et al.*, 2015). Observations collected at Barbados indicate that climate models vary cloudiness near cloud base more readily with changes in the large-scale environment than is observed (*Nuijens et al.*, 2015a). This indicates that climate models might not realistically predict cloud feedbacks and climate sensitivity. A better understanding of the factors controlling the strength of shallow convective mixing is thus crucial to reduce uncertainties in predicting climate sensitivity.

In this thesis we use large-eddy simulation (LES) to study how precipitation and shallow-convective organization modulate the response of shallow convection to forcing perturbations representative for climate change and the seasonal cycle. Thereby, we are particularly interested in how the organization and deepening of precipitating shallow convection influences the thermodynamic structure of the trade-wind layer and the vertical distribution of cloudiness. Ground-based in situ and remote sensing observations from the Barbados Cloud Observatory (BCO) are used to analyse the statistics of spatial organization as identified by cold pools, which are a surface manifestation of precipitating convection. We investigate how frequently cold pools occur and with what changes in the surface meteorology and the overlying cloud and humidity structure they are associated.

The remainder of this introduction discusses the structure of the trade-wind boundary layer and the influence of shallow convection on the atmospheric energy cycle (Section 1.1). Our current understanding of the influence of precipitation on shallow convection and its organization is presented in Section 1.2. Section 1.3 focuses on how large-scale forcings, like wind speed and subsidence, and important processes like radiation control shallow convection. The last section raises the questions addressed in the subsequent chapters and provides an outline of the thesis.

1.1. Trade-wind layer structure

Much of our understanding of the characteristic vertical structure associated with the trades dates back to the analyses of aircraft observations by Joanne Malkus (*Malkus*, 1954; 1956; 1958). As illustrated in Fig. 1.1 b, the trade-wind layer consists of a well-mixed sub-cloud layer, a thin stable transition layer near the lifting condensation level, a conditionally unstable cloud layer, and an inversion layer which separates the turbulent and moist trade-wind layer from the stable and dry free troposphere.

The vertical transport of heat and moisture by shallow convection has a strong influence on the strength of the Hadley circulation (*Riehl et al.*, 1951; *Riehl and Malkus*, 1957; *Tiedtke*, 1989; *von Salzen et al.*, 2005; *Neggers et al.*, 2006). Moisture transported upward by shallow convection is accumulated under the inversion and transported downstream towards the intertropical convergence zone (ITCZ), where it fuels deep convection (Fig. 1.1 a). The entrainment of dry free-tropospheric air into the trade-wind layer helps

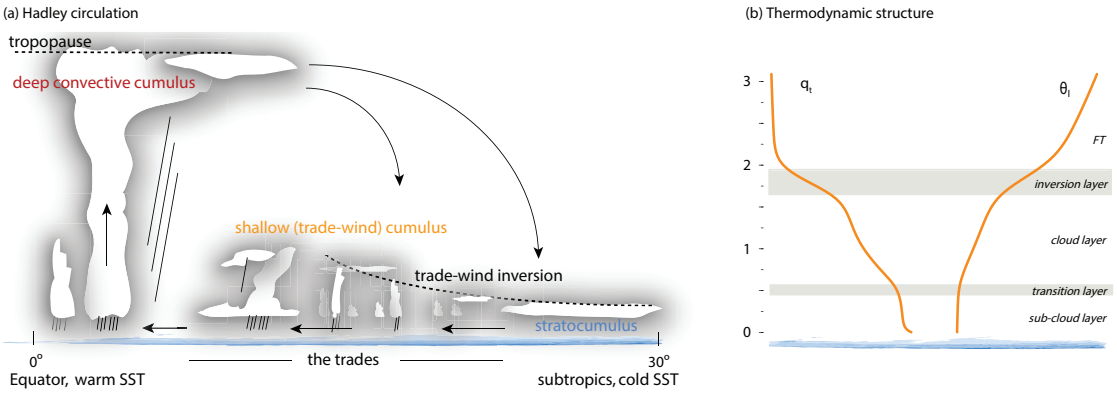

Figure 1.1.: (a) Schematic of the Hadley circulation with the different cloud regimes along the trade-wind trajectory (Courtesy: Louise Nuijens). (b) Illustration of the different layers characterizing the thermodynamic structure of the trade-wind boundary layer. Vertical profiles of total humidity q_t and liquid-water potential temperature θ_l are shown for the lowest 3 km of the troposphere. FT refers to the free troposphere.

maintain a high surface evaporation. Measurements from ship arrays during the BOMEX and ATEX field campaigns in the late sixties were used to quantify the heating and moistening effects of shallow convection (*Augstein et al.*, 1973; *Holland and Rasmusson*, 1973; *Nitta and Esbensen*, 1974). They showed that even in undisturbed conditions, the magnitude and location of the shallow-convective moisture source and heat sink near the top of the trade-inversion is highly variable. Furthermore, the heat and moisture budgets during more disturbed periods with organized convection are very different from the budgets during undisturbed periods (*Nitta and Esbensen*, 1974).

Heat and moisture budgets can be computed explicitly with LES, which resolves motions on the scale of the larger boundary layer eddies. But so far, LES has mostly been applied to cases with closely-balancing forcings, neglecting precipitation and the organization of shallow convection (e.g. *Siebesma and Cuijpers*, 1995). Hence, we still only poorly understand how changes in the large-scale forcing influences the heating and moistening due to shallow convection. Likewise, the role of precipitation and shallow convective organization in the heat and moisture budgets of the trades—and thus their influence on the export of moisture and heat to the deep convective regions downstream—is uncertain.

1.2. Precipitating shallow convection and its organization

Despite an early recognition that shallow trade-wind cumuli with tops between 1.5 and 2 km often precipitate (e.g. *Byers and Hall*, 1955; *Knight and Miller*, 1998; *Short and Nakamura*, 2000; *Nuijens et al.*, 2009), the influence of precipitation on the structure and the dynamics of the trade-wind layer have been ignored for a long time. Instead, much work has been devoted to quantifying the amount of precipitation from shallow cumulus

or understanding the processes responsible for warm-rain formation (e.g. *Beard and Ochs*, 1993; *Short and Nakamura*, 2000; *Rauber et al.*, 2007; *Snodgrass et al.*, 2009; *Blyth et al.*, 2013; *Siebert et al.*, 2013).

The influence of precipitation on the thermodynamic structure of the trades was first addressed by *Albrecht* (1993) using a simple bulk-equilibrium model. The study foreshadowed much of what we know from LES today. Namely, that precipitation limits the trade-wind layer depth by removing cloud droplets at cumulus tops that would otherwise evaporate into the inversion layer and deepen the cloud layer (*Albrecht*, 1993; *Stevens and Seifert*, 2008; *VanZanten et al.*, 2011; *Bretherton et al.*, 2013). And that the evaporation of precipitation in the lower cloud layer and sub-cloud layer weakens the humidity lapse rate and strengthens the temperature lapse rate (*VanZanten et al.*, 2011). Precipitation-driven downdrafts also influence the trade-wind layer by introducing additional gradients in the thermodynamic structure (*Betts and Albrecht*, 1987; *Zuidema et al.*, 2012).

The regulation of the cloud layer depth by precipitation is important for low-cloud feedbacks, because it limits the deepening and drying of the cloud layer in response to larger surface fluxes (*Blossey et al.*, 2013; *Bretherton et al.*, 2013). That precipitation from shallow convection limits the depth of the cloud layer is in contrast to deeper convection, where precipitation tends to increase updraft buoyancy by reducing the liquid water loading and by increasing the latent heating (e.g *Nuijens et al.*, 2017).

By redistributing some of the cooling and moistening by shallow convection from the cumulus tops to the lower trade-wind layer, precipitation can weaken the trade-inversion and limit surface evaporation because of near-surface moistening. Both processes potentially limit the moisture export to the deeper tropics. Indeed, results from a two-column radiative-convective equilibrium model show that warm rain from shallow cumulus and congestus clouds weakens the overturning circulation (*Nuijens et al.*, 2017).

Precipitation also influences the mesoscale organization of shallow convection through its associated cold pools. The satellite image in Fig. 1.2 shows the mesoscale organization of shallow cumulus clouds into arc-shaped clusters associated with secondary convection triggered at the cold-pool front. The arc-shaped clusters enclose a broad clear-sky area where convection is suppressed, along with remnants of the parent deeper convection. During the RICO field campaign, the highest rain rates were associated with such arc-shaped clusters (*Rauber et al.*, 2007; *Snodgrass et al.*, 2009). LES on relatively large domains of about $50\times50\,\mathrm{km}^2$ supports the emergence of shallow-convective organization into larger clusters and displays mesoscale structures similar to Fig. 1.2 (*Seifert and Heus*, 2013).

The thermodynamic and dynamic perturbations associated with cold pools influence the transition from shallow to deep convection (e.g. *Kuang and Bretherton*, 2006; *Khairoutdinov and Randall*, 2006; *Böing et al.*, 2012; *Jeevanjee and Romps*, 2013; *Schlemmer and*

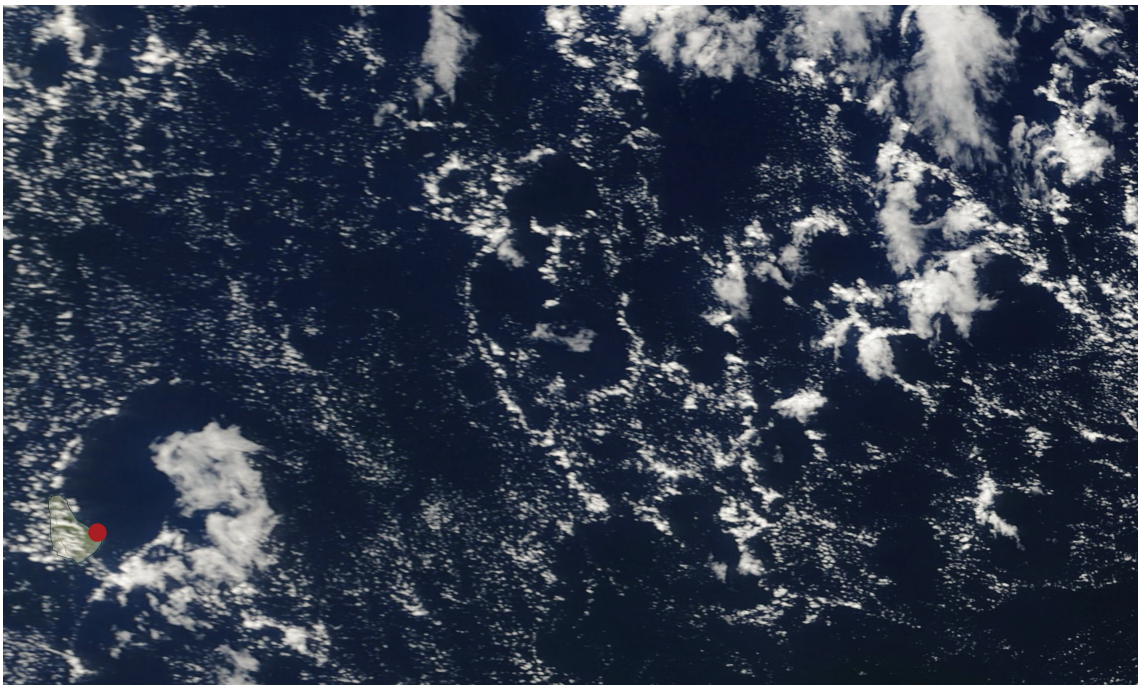

Figure 1.2.: MODIS *Terra* image recorded at 13.55 UTC on 12 February 2012 for the area from 12.5–15.5°N, 59.85–54.85°W. The mesoscale arc located over Barbados (in the lower left corner) has a radius of about 50 km. The red dot indicates the location of the Barbados Cloud Observatory (BCO).

Hohenegger, 2014; *Torri et al.*, 2015; *Feng et al.*, 2015). In particular, new convection triggered at colliding cold-pool boundaries experiences less entrainment drying, which is thought to promote the deepening of convection (*Böing et al.*, 2012; *Schlemmer and Hohenegger*, 2014; *Feng et al.*, 2015).

While cold pools influence the organization and deepening of shallow convection once the clouds are deep enough to produce substantial precipitation, recent LES by *Bretherton and Blossey* (2017) indicate that precipitation might not be necessary to initiate the organization, and neither are radiative feedbacks or interactive surface fluxes. The simulations by *Bretherton and Blossey* (2017) are representative for a slightly more suppressed regime than simulated in *Seifert and Heus* (2013), with shallower cumuli that do not precipitate strongly.

Independent of the processes initiating it, shallow-convective organization might have a pronounced influence on the spatial distribution of moisture, cloudiness and long-wave cooling in the lower troposphere. The LES in *Seifert and Heus* (2013) suggest that the trade-wind layer in the presence of organization has a larger moisture variance associated with the emergence of larger scale structures, but lower cloud cover. However, the relatively small vertical domain size of 4 km in *Seifert and Heus* (2013) did not allow the organized clusters to deepen much. In radiative-convective equilibrium studies, the orga-

nization of deep convection into a single moist patch with efficient precipitation leads to a much drier mean vertical structure (e.g. *Bretherton et al.*, 2005; *Muller and Held*, 2012). How the organization and deepening of shallow convection influences the thermodynamic structure in the trades remains unclear.

1.3. Large-scale cloud-controlling factors

As opposed to the control on the trade-wind layer structure and on cloudiness exerted by precipitation and shallow-convective organization—which are modulated by shallow convection itself—large-scale factors such as wind speed or sea-surface temperature (SST) also influence shallow convection. The shift from subsiding to rising mean vertical motion and the increase in SST separates cloud regimes along the trade-wind trajectory (Fig. 1.1a). Other large-scale factors like wind speed, horizontal advection, inversion strength or free-tropospheric humidity have also been identified as important cloud-controlling factors for marine boundary-layer clouds in observations (e.g. *Klein and Hartmann*, 1993; *Klein*, 1997; *Myers and Norris*, 2013; *Brueck et al.*, 2015; *Nuijens et al.*, 2015a), simple models (e.g *Betts and Ridgeway*, 1989; *Albrecht*, 1993), or LES (e.g *Sandu and Stevens*, 2011; *Nuijens and Stevens*, 2012; *Bretherton et al.*, 2013).

In the shallow cumulus regime, an increase in subsidence enhances the vertical advective drying, which limits the depth of the trade-wind layer (e.g *Betts and Ridgeway*, 1989; *Nuijens and Stevens*, 2012), but may enhance cloud cover by strengthening the inversion. An increase in wind speed enhances surface evaporation and correlates with enhanced low-level cloudiness and precipitation in observations (e.g. *Nuijens et al.*, 2009; *Brueck et al.*, 2015). Another important process controlling shallow convection is its interaction with radiation. Strong cloud-top radiative cooling is important for the propensity towards large stratiform cloud fractions under the trade-wind inversion in the LES intercomparison of the ATEX case (*Stevens et al.*, 2001). Interactive radiation also leads to a larger destabilization and a more rapid deepening of individual clouds and the inversion in transient stages of the LES (*Seifert et al.*, 2015).

Large-scale parameters in nature do not change on their own, but are linked with other large-scale parameters through circulations acting on various timescales. As such, positive correlations of wind speed and cloudiness also reflect the importance of the air mass history, because wind speed is correlated with wind direction, lower-tropospheric stability, and temperature advection (*Klein*, 1997; *Brueck et al.*, 2015). This also underlines how difficult it is to infer causal relationships between individual large-scale factors and the properties of shallow convection from observations.

Prominent examples of individual parameters changing in concert are the potential changes invoked by climate change and the seasonal cycle. For example, the shift from

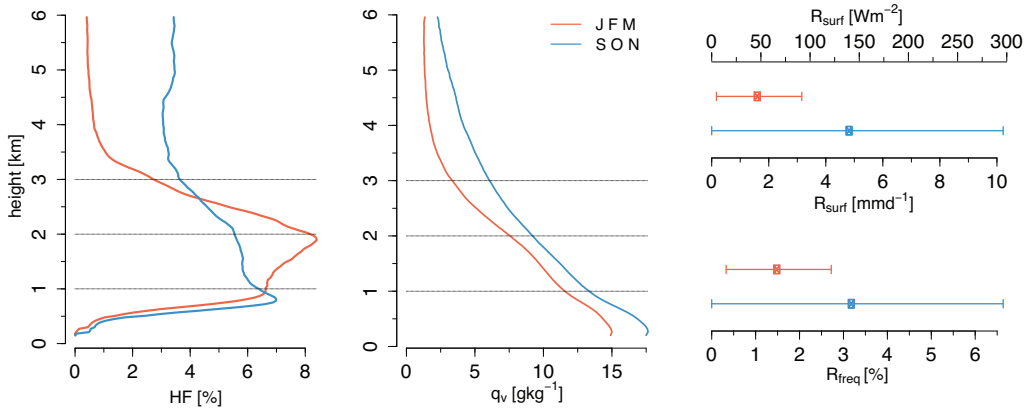

Figure 1.3.: Mean profiles of hydrometeor fraction HF and specific humidity q_v, and the mean$\pm 0.5\sigma$ of the daily surface precipitation rate R_{surf} and precipitation frequency R_{freq} for the period January–March (in red, representing the dry winter regime) and September–November (in blue, representing the wet summer regime). Data from the BCO is used for five years from January 2011 through Mid-September 2015. The hydrometeor fraction is similar to the cloud fraction and derived from a 36 GHz Doppler radar. The specific humidity is retrieved with a Raman lidar, and the surface precipitation measurements are made with a Vaisala WXT-520 weather sensor. Details on the data and the processing can be found in Chapter 4, in *Nuijens et al.* (2014; 2015a) or *Stevens et al.* (2016).

boreal winter to boreal summer at Barbados brings about an increase in SST, a shift from moderately subsiding to moderately rising motion, a reduction of wind speed, weaker horizontal advective cooling, and a moistening of the free troposphere (*Brueck et al.*, 2015). Fig. 1.3 shows how the seasonal changes affect the mean profiles of hydrometeor fraction and specific humidity, and the average frequency and intensity of surface precipitation at Barbados. The dry winter regime (red lines) has large hydrometeor fractions in the upper cloud layer between 1.5 and 2.5 km, a relatively pronounced humidity jump across the inversion, but only little precipitation. In the wet summer regime, frequent deep convection goes along with relatively large precipitation rates but low cloud fractions in the upper trade-wind layer around 2 km.

The last two sections of this introduction emphasize that both changes in the large-scale forcings and changes in the depth and organization of convection are important cloud-controlling factors in the trades. To understand the cloud and boundary-layer processes responsible for the observed seasonal changes in cloudiness and precipitation also requires a better understanding of how different large-scale factors influence the propensity of precipitating shallow convection to organize and deepen. The observed seasonal cycle at Barbados serves as a good starting point for such an investigation because clouds at Barbados are representative of clouds across the trade-wind region (*Medeiros and Nuijens*, 2016).

1.4. Research questions and strategy

The previous sections of this introduction highlight an insufficient understanding of how the interplay of precipitating shallow convection with its organization and the large-scale flow control the structure of the trades. This thesis investigates how precipitation and shallow-convective organization modulate the response of shallow convection to changes in the large-scale environment.

In ***Chapter 2*** and ***Chapter 3*** we use LES and perform a suite of numerical experiments to understand the response of precipitating shallow convection to perturbations associated with climate change and the seasonal cycle. More specifically, in ***Chapter 2*** we explore an idealized climate change scenario with uniform 4 K warming at constant relative humidity. We first address how precipitation and shallow-convective organization influence the trade-wind layer structure and cloudiness, and then focus on how the changes induced by precipitation and organization shape the warming response. In ***Chapter 3***, we start from the observed seasonal changes in cloudiness and precipitation at Barbados and ask what processes control the shift from more low-level cloudiness and less precipitation in winter, to less cloudiness and more precipitation in summer (see Fig. 1.3). A particular focus lies on the interaction of radiation with free-tropospheric humidity, on the influence of the surface forcing, and on the large-scale vertical velocity.

We perform the LES on large domains to allow the organization of precipitating shallow convection. We also apply interactive radiation and explore the role of computing the subsidence rate interactively to balance the heating tendencies of convection, radiation and precipitation. Thereby, we let go of many constraints that have limited the vertical development of shallow convection in previous LES studies. This allows us to move towards understanding shallow convection in a regime which is less strongly defined by the subsiding branch of the circulation, but by local cloud processes and local circulations. Our LES setup therefore renders more realistic the simulated cloud and trade-wind layer structures compared to LES setups with small domains and uniform radiation (*Siebesma et al.*, 2003; *VanZanten et al.*, 2011; *Bellon and Stevens*, 2012). The study yet relies on LES adequately describing cloud amount. This is evaluated in ***Appendix B***, which presents a review of the robustness and uncertainties of simulated cloud amount from LES.

Because of the inherent limitations of numerical simulations, in ***Chapter 4*** we shift the methodology to the use of observations collected at the BCO. We explore the statistics of spatial organization as identified by cold pools in a 9-year surface temperature timeseries. Furthermore, ground-based remote sensing observations of clouds and the humidity structure are used to relate changes in the vertical structure of the trades to the passage of cold-pool fronts.

Chapter 2

The role of precipitation and spatial organization in the response of trade-wind clouds to warming[1]

Abstract

Using highly resolved large-eddy simulations on two different domain sizes, we investigate the influence of precipitation and spatial organization on the thermodynamic structure of the trade-wind layer, under a uniform 4 K warming at constant relative humidity. In non-precipitating simulations the increased surface latent heat flux in the warmer climate produces a deeper and drier cloud layer with reduced cloud fractions between 1.5 and 4 km. Precipitation prevents the deepening and drying of the cloud layer in response to warming. Cloud fractions still decrease in the upper cloud layer, because stratiform outflow layers near cloud tops are less pronounced and because the larger liquid water contents are confined to narrower updrafts. Simulations on a sixteen-fold larger domain lead to the spatial organization of clouds into larger and deeper cloud clusters. The presence of deeper clouds results in a shallower, warmer and drier trade-wind layer, with strongly reduced cloud cover. The warming response in the precipitating large-domain simulation nevertheless remains similar to the small-domain precipitating simulation. On the large domain, deeper clouds can also develop without precipitation, because moisture-convection

[1] This chapter has been published with minor modifications as: Vogel, R., L. Nuijens, and B. Stevens (2016), The role of precipitation and spatial organization in the response of trade-wind clouds to warming, *J. Adv. Model. Earth Syst.*, *8*(2), 843–862, doi:10.1002/2015MS000568.

feedbacks strengthen in the absence of cold-pool dynamics. Overall, total cloud cover and albedo decrease only slightly with warming in all cases. This demonstrates the robustness of shallow cumuli—in particular of cloud fraction near the lifting condensation level—to changes in the large-scale environment.

2.1. Introduction

Shallow trade-wind cumuli in regimes with moderately subsiding large-scale vertical motion have been recognized as a critical source of uncertainty in projections of future climate (e.g. *Bony and Dufresne*, 2005; *Vial et al.*, 2013). Covering a large fraction of the world's oceans, these marine boundary layer clouds are decisive for climate change not only through their impact on the shortwave radiation budget, but also for their role in driving atmospheric circulations, both by modulating surface evaporation (e.g. *Tiedtke*, 1989; *Stevens*, 2007) and by influencing the distribution of longwave cooling within the atmosphere (*Muller and Held*, 2012; *Emanuel et al.*, 2014; *Fermepin and Bony*, 2014). Most comprehensive climate models indicate a reduction of cloud cover in response to warming and thus a positive low cloud feedback; because of insufficient physical understanding, however, confidence in these results remains low (*Boucher et al.*, 2013).

Because of uncertainties in the parameterization of boundary layer clouds in climate models, other tools are required to advance understanding of how low clouds change in response to climate perturbations. High resolution models like LES promote process-level understanding, because they explicitly resolve motions on the scale of the larger boundary layer eddies. Using LES, *Rieck et al.* (2012) introduced the idea that due to increasing surface latent heat fluxes, the cloud layer deepens and, by enhanced entrainment of dry free tropospheric air, becomes relatively drier. This drying reduces the cloud cover which, all else being equal, would constitute a positive cloud feedback in the shallow cumulus regime. The simple study design, using a uniform temperature increase at constant relative humidity, revealed a new mechanism influencing cloud feedbacks. But this approach also had limitations, most significantly perhaps its neglect of precipitation.

Observations show that trade-wind cumuli precipitate frequently (e.g. *Short and Nakamura*, 2000; *Nuijens et al.*, 2009; *Burdanowitz et al.*, 2015). Precipitation changes the microphysical structure of the shallow clouds and influences the energetics of the trade-wind boundary layer, including the heating and moistening tendencies and the growth rate of the boundary layer (here including both the sub-cloud and the trade-wind cloud layer). Because precipitation removes liquid water available for evaporation at cloud top, it limits cloud layer deepening (*Albrecht*, 1993; *Stevens and Seifert*, 2008; *VanZanten et al.*, 2011; *Bretherton et al.*, 2013)—an important mechanism in the response of shallow cumulus to idealized climate perturbations (*Blossey et al.*, 2013; *Bretherton et al.*, 2013). Precipita-

tion also affects cloud amount and cloud organization, through the emergence of cold pools (e.g. *Zuidema et al.*, 2012; *Seifert and Heus*, 2013). Here we ask if the response of cloudiness to warming differs as a result of allowing shallow convection to precipitate, a question motivated by the effect of precipitation on both the spatial structure of convection and the rate of convective deepening.

To investigate the response of clouds to warming in the presence of precipitation, we perform simulations on relatively large domains, because this has been shown to influence the degree to which convection organizes (e.g. *Muller and Held*, 2012; *Seifert and Heus*, 2013). Much deeper convection emerges in simulations supporting convective organization, which provides an opportunity to study the response of clouds to warming in a more convective regime. By contrasting the warming response of clouds in the large domain, in which deeper convection arises, with that in a smaller domain, it is also possible to ask to what extent the depth of convective mixing influences the cloud response to warming, as has been hypothesized in some recent studies (*Sherwood et al.*, 2014; *Zhao*, 2014).

We study the effect of an idealized climate change on precipitating shallow convection by applying a uniform warming to the initial temperature profile in a constant relative humidity framework, similar to *Rieck et al.* (2012). An idealized approach helps clarify the physical effects at play in the simplest possible setting. This has advantages and disadvantages. For instance, the idealizations may distort the response of clouds to climate change by leaving out important cloud-controlling factors such as wind shear, increases in free-tropospheric stability, changes in the CO_2 concentration, in longwave cooling, subsidence strength or inversion stability (e.g. *Bretherton et al.*, 2013). Thus, our results should not be considered as a quantification of cloud feedbacks, but rather as an attempt to understand a particular problem that is relevant for climate change.

The structure of the paper is as follows. The LES code, the model setup and the experiment design are discussed in Section 2.2. Section 2.3 investigates the impact of precipitation on the trade-wind boundary layer. How precipitation modulates the warming response is discussed in Section 2.4. In Section 2.5 we use large domain simulations to study the impact of deeper (and arguably more aggregated) convection on both the thermodynamic structure of the trade-wind layer and its response to warming. Concluding remarks are presented in Section 2.6.

2.2. Large-Eddy Simulation

We perform LES with the University of California Los Angeles (UCLA) LES code (*Stevens et al.*, 2005) in a setup representative of the conditions in the broader trades. In contrast to *Rieck et al.* (2012) who used the RICO case study described by *VanZanten et al.* (2011), we adopt the framework of *Bellon and Stevens* (2012). The framework has been used to study

non-precipitating stratocumulus and shallow cumulus convection in contrasting large-scale environments (*Bellon and Stevens*, 2012; *Nuijens and Stevens*, 2012; *Bellon and Geoffroy*, 2016). Our motivation for this change is twofold: (a) it allows us to test the generality of the *Rieck et al.* (2012) results, and (b) brings the simulation closer to equilibrium as the free tropospheric tendencies are strictly balanced. Achieving an equilibrium is particularly important with precipitation whose intermittent nature necessitates long averaging times (and/or very large domains).

2.2.1. LES Code

The UCLA LES solves the Ogura-Phillips anelastic equations with prognostic equations for the three wind components and two thermodynamic variables, the liquid water potential temperature (θ_l) and the total water mixing ratio (q_t), which includes vapor and cloud water. A third-order Rungge-Kutta time integration is used with variable time step (1 s or less to satisfy the Courant-Friedrichs-Lewy criterion). Momentum advection is based on 4th-order centered differences, while a higher-order upwind method with monotone centered slope limiters is applied to advect the scalars. The subgrid scale fluxes are modeled with the Smagorinsky-Lilly model.

Liquid water content is diagnosed according to a saturation adjustment scheme. Precipitating simulations are performed with the two-moment warm rain scheme of *Seifert and Beheng* (2001), assuming a constant cloud droplet number concentration $N_\mathrm{c} = 50$ cm^{-3} (representing clean maritime conditions at the lower end of observations (*Siebert et al.*, 2013)) and solving two additional prognostic equations for rain mass and number concentration. A more detailed description of the cloud microphysical model is provided by *Savic-Jovcic and Stevens* (2008).

2.2.2. Model Setup and Experiment Design

The framework we use prescribes large-scale forcings and initial profiles characteristic for the broader trades. Wind shear, which may be important for regulating mixing and projected cloud cover, is not prescribed in this study. Some shear develops in the lowest 1.5 km (see Fig. 2.4), but we do not attempt to address here how shear, or changes in shear, might modify the response of clouds to warming. The setup uses a Eulerian reference frame with homogeneous large-scale forcings (fixed sea surface temperature (SST) and subsidence). The forcings are prescribed as follows:

1. Subsidence: exponential profile with maximum value of $w_0 = 7.5 \times 10^{-3}$ $\mathrm{m\,s^{-1}}$
2. Radiative cooling: uniform cooling of $Q_\mathrm{R} = -2.5\,\mathrm{K\,d^{-1}}$
3. Wind speed: a barotropic geostrophic wind of $10\,\mathrm{m\,s^{-1}}$ aligned with the x-coordinate of the domain

Table 2.1.: Specifications used for the different perturbation experiments.
[a] A similar implementation as in *Seifert et al.* (2015) is used for interactive radiation, which is based on the broadband radiation code of *Fu and Liou* (1992) and uses Monte Carlo spectral Integration (*Pincus and Stevens*, 2009).

case name	SST [K]	θ_l profile	q_t profile	precipitation	domain [km^3]	radiation
noP-CTL	300	CTL	CTL	off	12.8×12.8×10	uniform
noPlarge-CTL				off	51.2×51.2×10	
P-CTL				on	12.8×12.8×10	
Plarge-CTL				on	51.2×51.2×10	
noP+4K	304	+4 K	adjusted	off	12.8×12.8×10	uniform
P+4K				on	12.8×12.8×10	
Plarge+4K				on	51.2×51.2×10	
additional sensitivity experiments:						
P-4K	296	−4 K	adjusted	on	12.8×12.8×10	uniform
Plarge-4K				on	51.2×51.2×10	
Δ seeds [3×] (102.4km)^2	300	CTL	CTL	on	12.8×12.8×10 102.4×102.4×10	uniform
IRAD Plarge	300	CTL	CTL	on	51.2×51.2×10	interactive[a]

Both the subsidence rate and the radiative cooling are relatively large compared to other case setups, but help compensate for the lack of additional drying and cooling from horizontal advection.

The initial temperature and humidity profiles (Fig. 2.1) have a well-mixed sub-cloud layer, topped by an inversion layer. The free tropospheric temperature lapse rate is chosen such that subsidence warming balances radiative cooling. Bulk aerodynamic formulas parameterize the surface thermodynamic and momentum fluxes, with constant SST and a slip/no-penetration condition. Integrations are performed with a horizontal grid spacing of 50 m and a vertical grid spacing uniformly stretched by a factor of 1.02 from 10 m at the surface to about 200 m at the domain top at 10 km.

Table 2.1 provides an overview of the experiments performed (the focus lies on the upper seven simulations; the additional sensitivity experiments will be referred to in Section 2.5 and Appendix A). We distinguish the control (CTL) and the warmed (+4K) climate state, the non-precipitating and precipitating cases on the small 12.8×12.8 km^2 domain (noP and P) and on the sixteen-fold larger 51.2×51.2 km^2 domain (Plarge and noPlarge). The difference between the two climate states is a uniform 4 K shift of the temperature profile in the +4K case compared to the CTL, along with an equivalent SST increase. The +4K humidity profile is adjusted such that the initial profile of the relative humidity is not changed. For both climate states, a precipitating and a non-precipitating simulation is performed on the small domain.

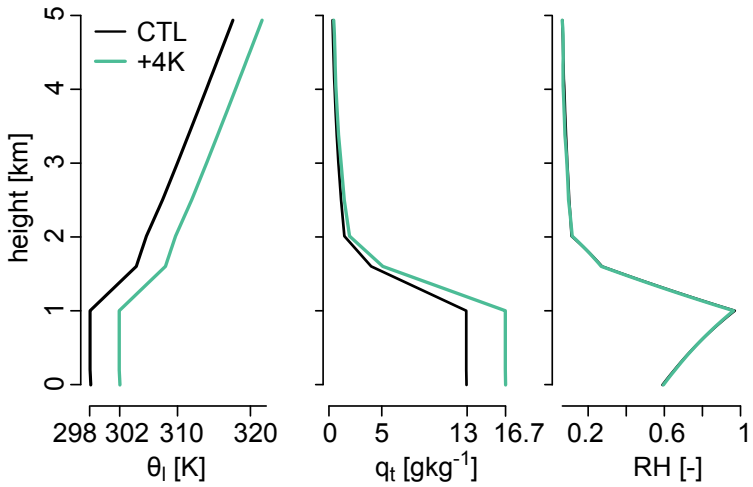

Figure 2.1.: Initial profiles of the liquid water potential temperature θ_l, total humidity q_t and relative humidity RH, for the CTL and +4K climate states.

To allow deeper clouds to form, we perform additional precipitating simulations of both the CTL and +4K climate state on the larger domain which allows for shallow convective organization. To test whether convection organizes in the absence of cold pools, the non-precipitating CTL simulation is also performed on the large domain. As indicated in the introduction, some of the large-domain simulations produce relatively deep clouds reaching beyond the freezing level and up to the domain top. To prevent these simulations from accumulating liquid at the top, a nudging towards the initial q_t-profiles is applied in the six highest model levels, beginning at 8.8 km. Ice processes, which become increasingly relevant for clouds above 8 km in the tropics, are not considered. Because our focus is on shallow convection, and we merely use the simulations that develop deeper convection to explore its effect on the structure of the shallower clouds, we do not believe that this admittedly artificial treatment unduly influences the interpretations we draw from the simulations.

Because precipitation and domain size strongly determine the time to reach quasi-stationarity, if reached at all, different averaging periods are used to present the statistics, namely day 7 to 10 for P-CTL and P+4K, day 2.5 to 4 for Plarge-CTL and Plarge+4K, and day 7 and 8 (in Section 2.3) or day 7 only (Section 2.4) for noP-CTL and noP+4K.

2.3. The Importance of Precipitation for Attaining an Equilibrium

In this section we document the influence of precipitation on the thermodynamic structure of the simulated trade-wind boundary layer and present a comparison of the baseline behavior of the precipitating and non-precipitating control simulations on the small domain.

In terms of the general evolution of the flow, a shallow layer of cumulus develops after a few hours of simulation time (Fig. 2.2). This layer progressively deepens, reaching a depth of about 2250 m after two simulation days with a total cloud cover of 12.5 % and mean cloud base near 600 m. The surface fluxes evolve more slowly, with surface sensible and latent heat fluxes of respectively $-1.8\,\mathrm{W\,m^{-2}}$ and $300\,\mathrm{W\,m^{-2}}$ after two days, while the latter decreases to a value around $250\,\mathrm{W\,m^{-2}}$ after eight days. The negative value of the sensible heat flux is caused by entraining warmer cloud layer air into the well-mixed sub-cloud layer in the absence of sufficient radiative or horizontal-advective cooling, which reduces the temperature gradient with respect to the underlying SST. Relatively deep cloud layers develop in our simulations with surface latent heat fluxes that are larger than measured during the BOMEX campaign (see e.g. *Holland and Rasmusson* (1973)), but not far from RICO observations when latent heat fluxes as strong as $250\,\mathrm{W\,m^{-2}}$ were measured (*Zuidema et al.*, 2012; *Nuijens et al.*, 2009). One reason for the large latent heat fluxes of both the P-CTL and noP-CTL simulations is the on average $1-2\,\mathrm{g\,kg^{-1}}$ drier initial humidity profile in the lower free troposphere compared to other trade-wind cumulus cases (*VanZanten et al.*, 2011; *Bellon and Stevens*, 2012). The reduced free-tropospheric humidity enhances the drying of the boundary layer through cloud-top entrainment and—rather than suppressing convection as one may expect—increases the vigor of convection through a larger surface buoyancy flux.

The timeseries (Fig. 2.2) show that the P-CTL and noP-CTL simulations have a similar boundary layer depth, surface fluxes and cloud properties until the cloud layer is deep enough for the shallow clouds to produce substantial precipitation on the order of $0.5\,\mathrm{mm\,d^{-1}}$ ($\sim 15\,\mathrm{W\,m^{-2}}$) after four days. As soon as substantial precipitation sets in, the cloud layer ceases to deepen further. The noP-CTL simulation does not reach stationarity and cloud cover continues to increase with time, especially towards the end of the simulation when pronounced stratiform outflows are formed. In P-CTL, however, the onset of precipitation stops the steady increase of cloud cover, which reaches a value of 13.5 % in equilibrium. The P-CTL timeseries show marked oscillations: the domain size of $12.8\times12.8\,\mathrm{km^2}$ only supports one or two larger precipitating clouds which leave an imprint on the time series (such variations are much less pronounced on the larger domain).

Precipitation removes liquid that would otherwise evaporate and deepen the cloud layer—a mechanism that is both understood theoretically (*Stevens*, 2007) and evident in models with different degrees of complexity (*Albrecht*, 1993; *Stevens and Seifert*, 2008; *VanZanten et al.*, 2011; *Bretherton et al.*, 2013). Reaching an equilibrium state, including a halt of boundary layer growth, requires that the heating and moistening tendencies are in balance throughout the layer. The following terms appear in the tendency equations, written in terms of the apparent heat sink Q_1 and moisture source Q_2 (following *Yanai et al.* (1973)):

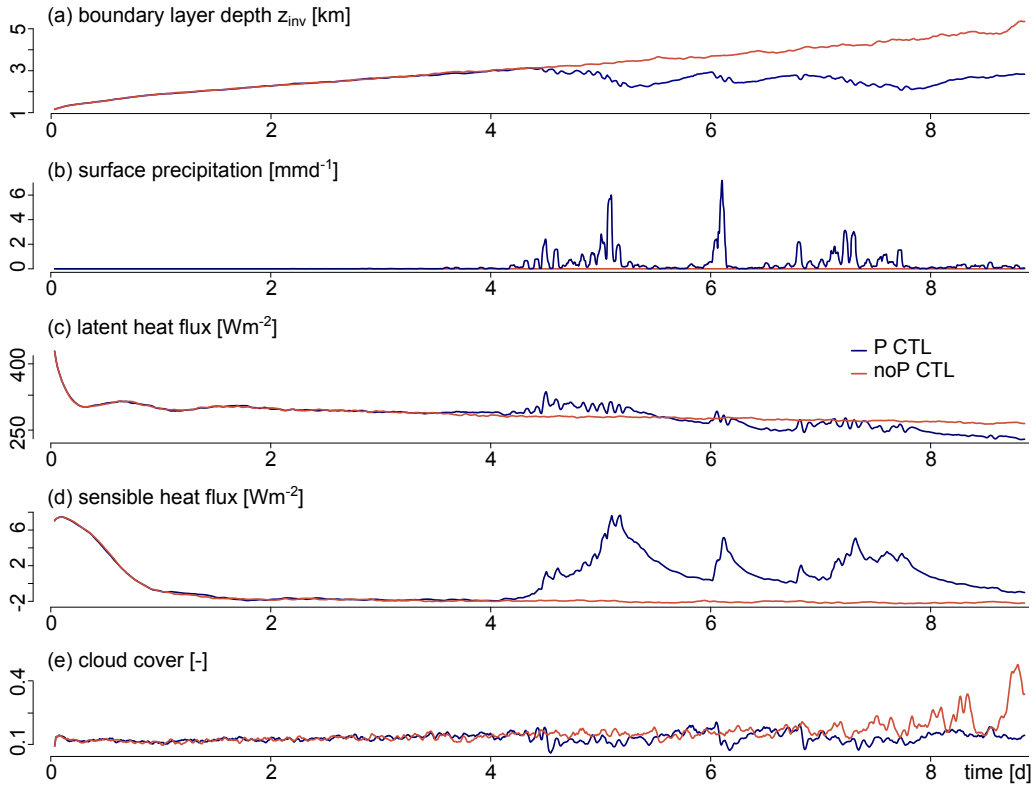

Figure 2.2.: Domain-averaged time series for P-CTL (darkblue) and noP-CTL (red).

$$Q_1 := -\left[\left.\frac{\partial\bar{\theta}_\mathrm{l}}{\partial t}\right|_\mathrm{tot} + \omega\left.\frac{\partial\bar{\theta}_\mathrm{l}}{\partial z}\right|_\mathrm{sub}\right] = -\left.\frac{\partial\bar{\theta}_\mathrm{l}}{\partial t}\right|_\mathrm{cnv} - \left.\frac{\partial\bar{\theta}_\mathrm{l}}{\partial t}\right|_\mathrm{prc} - Q_\mathrm{R} \tag{2.1}$$

$$Q_2 := \frac{L}{c_p}\left[\left.\frac{\partial\bar{q}_\mathrm{t}}{\partial t}\right|_\mathrm{tot} + \omega\left.\frac{\partial\bar{q}_\mathrm{t}}{\partial z}\right|_\mathrm{sub}\right] = \frac{L}{c_p}\left[\left.\frac{\partial\bar{q}_\mathrm{t}}{\partial t}\right|_\mathrm{cnv} + \left.\frac{\partial\bar{q}_\mathrm{t}}{\partial t}\right|_\mathrm{prc}\right] \tag{2.2}$$

where the terms on the left-hand side are the storage term or total tendency and large-scale subsidence. The terms on the right-hand side represent the contributions from convection (which is the turbulent flux divergence that represents the resolved and subgrid scale components of the simulated flow), precipitation and, in case of θ_l, the prescribed radiative cooling Q_R. Overbars stand for horizontal (slab) averages. To convert $\mathrm{g\,kg^{-1}}$ to $\mathrm{K\,d^{-1}}$, the moistening tendencies are multiplied by the enthalpy of vaporization L and divided by the isobaric specific heat capacity of dry air c_p. Given the choice of the thermodynamic variables as θ_l and q_t, the condensation and evaporation of cloud droplets does not affect the heat and moisture budget. For precipitation processes, however, θ_l (following its formulation in the LES) and q_t are not conserved and the formation and evaporation of precipitation represent a heating/drying and a cooling/moistening respec-

tively. Note that we inverted the signs of Q_1 and Q_2 compared to *Yanai et al.* (1973), as shallow convection mainly acts as a source of moisture rather than a sink. Because Q_R is constant, Q_1 is shown without the radiative contribution (that is, $Q_1 + Q_R$).

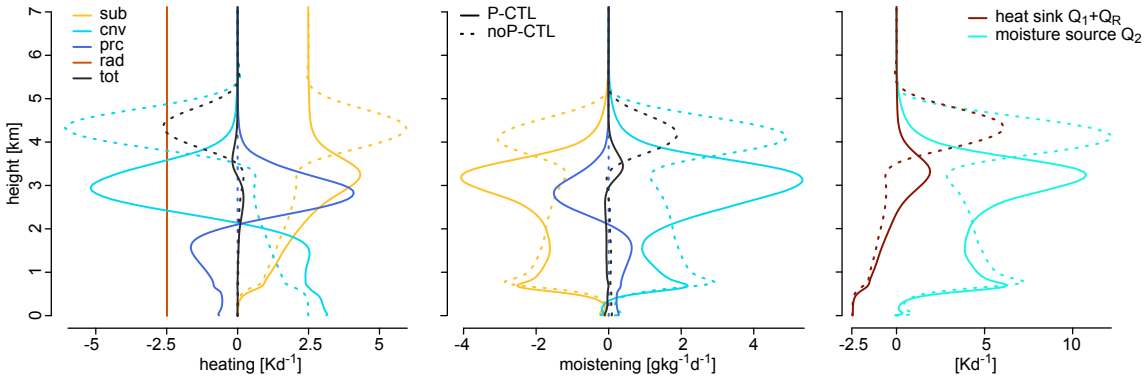

Figure 2.3.: (left and middle) vertical profiles of domain averaged contributions of the tendency equation terms for θ_l (heating) and q_t (moistening), and (right) the profiles of the heat sink ($Q_1 + Q_R$) and moisture source (Q_2). Shown are P-CTL (solid) and noP-CTL (dashed, averaged over day 7 and 8).

Fig. 2.3 illustrates how the boundary layer state is maintained by the different processes. In noP-CTL, the balance in the inversion layer, located here around 4.2 km, is given by the uniform radiative cooling, large-scale subsidence and convection. At the inversion, the warm and dry subsiding air meets with the moist and cold air lofted by convection. This leads to a maximum of both subsidence warming and drying, and convective cooling and moistening. In the specified large-scale environment, subsidence is not strong enough to counteract the convective tendencies, and a strong residual tendency remains that cools and moistens the inversion layer (the residual moistening tendency integrated over the whole boundary layer amounts to 47 Wm^{-2}, see Table 2.2). As convection keeps destabilizing the inversion layer and increasing the depth of the cloud layer, the boundary layer deepens (*Betts*, 1973; *Stevens*, 2007).

Precipitation has an opposing tendency to convection in the inversion layer. The heating and drying induced by precipitation formation limits boundary layer deepening and leads to a negligible residual integrated moistening tendency of 1 Wm^{-2} (Table 2.2). The right panel of Fig. 2.3 shows the apparent heat sink ($Q_1 + Q_R$) and moisture source (Q_2). The heat sink in the inversion layer is strongly reduced due to the heating tendency of precipitation. Also the Q_2 maxima in the inversion layer and near the cumulus bases around 700 m are somewhat smaller in P-CTL. The evaporation of precipitation provides a cooling and moistening over much of the cloud layer, which goes along with reduced convective moistening in the lower cloud layer compared to noP-CTL. The resulting temperature and humidity profiles (Fig. 2.4) show that the lapse rates change in the shallower precipitating cloud layer, with stronger temperature and weaker humidity lapse rates. As

Table 2.2.: Averages of surface latent heat flux (LHF), changes in LHF with warming (ΔLHF), the surface precipitation rate (P_{surf}), integrated subsidence drying (D), integrated residual moistening tendency (DT), surface sensible heat flux (SHF), boundary layer depth (z_{inv}, representing the location of maximum θ_l-gradients), cloud cover (CC), liquid water path (LWP), albedo (α), cloud base height (c_b) and maximum cloud fraction (CF_{max}, corresponding to the maximum at cloud base); for the noP and P simulations of both the CTL and +4K climate state. Values labeled with * denote averages taken over day 7 only, instead of day 7 and 8, to exclude biases introduced by the very deep cloud layer of the noP+4K simulation. Note that P_{surf} constitutes a negative contribution to the integrated moisture budget.

case	LHF [Wm^{-2}]	ΔLHF [$\%K^{-1}$]	P_{surf} [Wm^{-2}]	D [Wm^{-2}]	DT [Wm^{-2}]	SHF [Wm^{-2}]	z_{inv} [m]	CC [%]	LWP [gm^{-2}]	α [%]	c_b [m]	CF_{max} [%]
noP-CTL	273	6.9	-	-226	47	-2.1	4116	16.2*	27.5*	10.7*	617	4.3
noP+4K	347		-	-282	64	-6.5	4940	15.3*	33.2*	10.5*	675	4.2
P-CTL	251	5.8	15	-236	1	0.7	2633	13.5	36.4	8.0	516	3.9
P+4K	310		16	-302	-8	-2.3	2056	11.9	40.6	7.1	528	3.7

such, subsidence warming increases and subsidence drying decreases below about 2.5 km (see Fig. 2.3).

VanZanten et al. (2011) noted the same behavior of the temperature and humidity profiles in precipitating LES of the RICO case, and also found that much of the evaporation of precipitation is concentrated in the cloud layer and not merely confined to the sub-cloud layer. *Albrecht* (1993) reported a similar effect of precipitation on the temperature stratification of the cloud layer. The cloud layer in his model, however, became drier, likely because the evaporation of precipitation was confined to the sub-cloud layer. Different microphysics schemes of different LES codes tend to produce very different precipitation flux (and cloud fraction) profiles, particularly if averaged over a few hours only (*VanZanten et al.*, 2011; *Li et al.*, 2015). Investigating the influence of cloud droplet number concentration N_c on precipitating shallow convection, *Seifert et al.* (2015) find that all simulations reach a similar near-equilibrium rain rate. The main response to larger N_c is a delayed onset of rain, along with a slight deepening and drying of the cloud layer. So even if the cloud layer depth and the relative contribution of the different processes in the budgets depend slightly on N_c, the existing evidence suggests that N_c has little influence on the equilibrium response.

How do the changes of the thermodynamic structure in the presence of precipitation influence the clouds? The profiles of liquid water (Fig. 2.4) show that the larger relative humidity in the cloud and sub-cloud layer results in more condensate-laden clouds with lower cloud bases. Although the precipitating cloud layer is shallower and liquid water is removed by precipitation, the liquid water path corresponding to the profiles displayed is 36.4 g m^{-2} in the P-CTL compared to 30.1 g m^{-2} in noP-CTL. In both cases, cloud fraction maximizes at cloud base and decreases with height through the cloud layer until the base of the inversion layer, where it increases slightly (depending on the case). Compared to

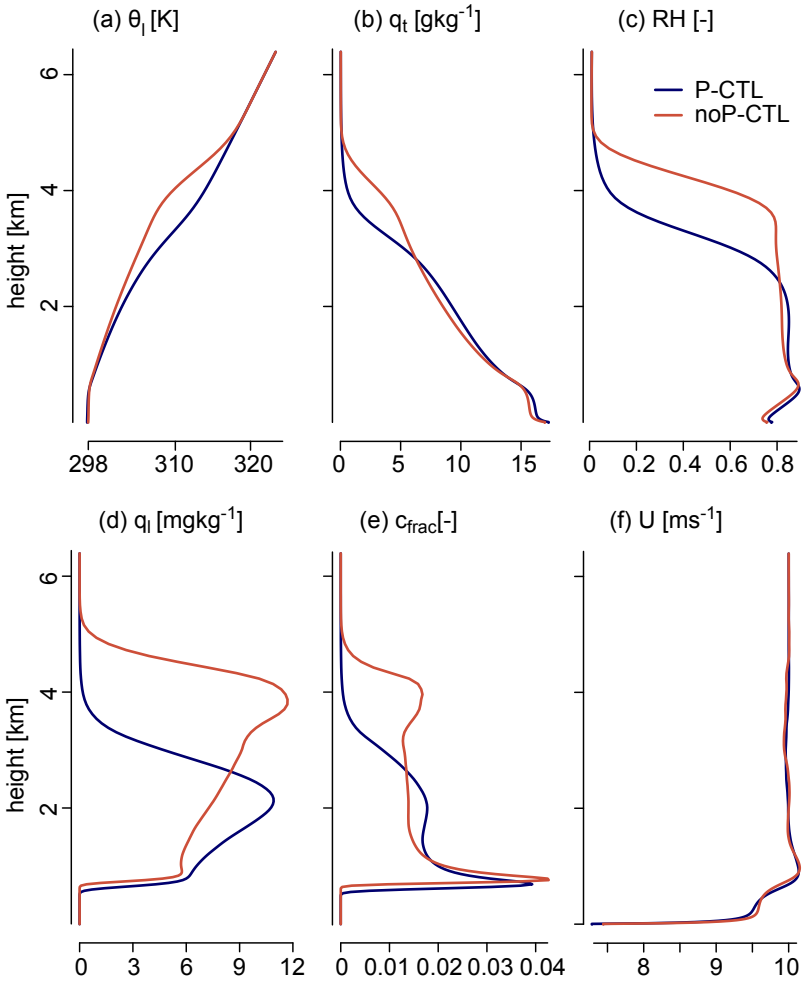

Figure 2.4.: Domain-averaged vertical profiles of (a) the liquid water potential temperature θ_l, (b) total humidity q_t, (c) relative humidity RH, (d) domain-mean liquid water q_l, (e) cloud fraction c_{frac}, and (f) zonal wind speed U. Shown are P-CTL (darkblue) and noP-CTL (red, averaged over day 7 and 8).

noP-CTL, P-CTL has larger cloud fractions above cloud base, but total cloud cover, as defined by the number of cloudy columns, reduces to 13.5 % compared to 17 %, due to the clouds being shallower. Stronger wind shear would probably enhance the differences between the simulations, because the contribution of the deeper clouds (in noP-CTL) to projected cloud cover may increase in the presence of shear.

2.4. How Precipitation Modulates the Warming Response

What do the results of the previous section imply for the response of the precipitating simulation to warming? Here we use the simulations to address the hypothesis that if precipitation controls the depth of the boundary layer, the deepening and drying response to warming found in the non-precipitating simulations of *Rieck et al.* (2012) is muted. To

do so, we first consider the warming response in our non-precipitating simulations.

2.4.1. Non-precipitating warming response

We find a similar response as *Rieck et al.* (2012) in the non-precipitating simulations, namely an increase in surface latent heat flux, a decrease in sensible heat flux, a deepening of the cloud layer and reductions in cloud cover (Table 2.2 and Fig. 2.5). The vertical profiles (Fig. 2.6) indicate a slight relative drying associated with the deeper cloud layer of the noP+4K case: the relative humidity in the cloud layer between 1.5 and 4 km is slightly reduced, leading to reduced cloud fraction and liquid water at those heights. Because the relative humidity also reduces in the sub-cloud layer, cloud base rises by about 10%. How much a reduced cloud fraction between 1.5 and 4 km contributes to a reduction in total cloud cover may depend on how strongly clouds are sheared with height. Unlike in the RICO setup used by *Rieck et al.* (2012), the uniform wind in the present framework is associated with less shear (Fig. 2.4 f), but an unambiguous response to shear is not obvious. Rather than enhancing projected cloud cover, shear may also limit the lifetime of convective elements and reduce cloud cover. Despite clouds in the noP+4K case being deeper, the reduced cloud fraction between 1.5 and 4 km and less of a stratiform cloud component at cloud top lead to a $\sim$1% overall reduction of cloud cover (see Table 2.2). Because comparable reductions in cloud cover with warming occur in *Rieck et al.* (2012), it suggests that wind shear does not play a first order role in the response of the simulations to warming. As the liquid water path is larger in noP+4K, the estimated albedo reduces only slightly, from 0.107 to 0.105. Here, the relation from *Zhang et al.* (2005) is used to approximate the albedo at a grid point by $\alpha = \tau/(6.8+\tau)$, with an optical depth estimate of $\tau = 0.19\ \mathrm{LWP}^{5/6}\ \mathrm{N}_c^{1/3}$. Overall, it is worth bearing in mind how small the changes are.

Along with the small changes in cloudiness, the differences in the apparent heat sink ($Q_1 + Q_\mathrm{R}$) between the noP-CTL and noP+4K case are, except for the upward shift of the maximum, very small (Fig. 2.7). This is because the initial temperature profile of the +4K case is shifted uniformly by 4 K and the lapse rate and thus subsidence warming are largely unaffected. Differences in the moisture source Q_2 are more pronounced throughout the cloud layer, because the initial absolute humidity profile of the +4K case is not uniformly shifted, but adjusted by the amount necessary to keep relative humidity constant. The differences in humidity therefore vary from $\Delta q_\mathrm{t} = 3.7\,\mathrm{g\,kg^{-1}}$ at the surface to $\Delta q_\mathrm{t} \approx 0\,\mathrm{g\,kg^{-1}}$ at domain top. The vertical humidity gradient is thus enhanced and subsidence drying increases, which is balanced by more convective moistening (see also the integrated tendencies in Table 2.2). However, the additional moistening is only enough to compensate the enhanced subsidence drying in the cloud layer, and not the additional drying related to the redistribution of moisture across a deeper layer. Consequently, relative humidity decreases in the cloud layer in the +4K case.

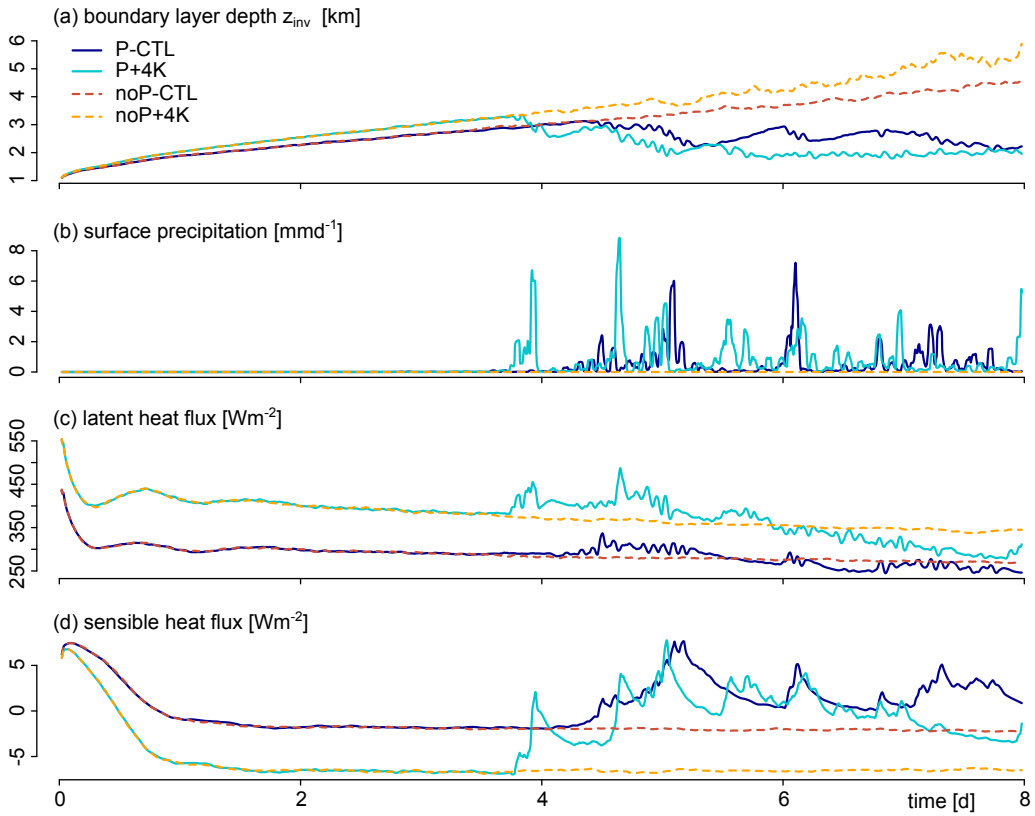

Figure 2.5.: Domain-averaged time series of P (solid) and noP (dashed) for both the CTL and +4K climate states.

2.4.2. Precipitating warming response

What about the warming response in the precipitating case? During the first 3.5 days before noticable precipitation is found at the surface, the P+4K surface fluxes show the same behavior as in the noP+4K case and enhance boundary layer deepening compared to P-CTL (Fig. 2.5). Because the clouds deepen more readily in P+4K, they precipitate sooner. In equilibrium, the P+4K boundary layer is shallower than P-CTL, and the differences in boundary layer depths is reduced compared to the noP cases (see Table 2.2). Also the differences in the surface fluxes between the two climate states are smaller than in the noP cases.

Although the mean cloud layer becomes even shallower in P+4K, the relative humidity in the cloud layer is very similar between P-CTL and P+4K (Fig. 2.6). Also the sub-cloud layer relative humidity and the average cloud-base height remain similar. Some deeper clouds develop that reach depths above 7 km. These deeper clouds increase relative humidity above 3 km and weaken the inversion, but have no strong imprint on the mean profiles of cloud fraction and liquid water.

Even though relative humidity is reduced only little in P+4K, cloud fractions reduce

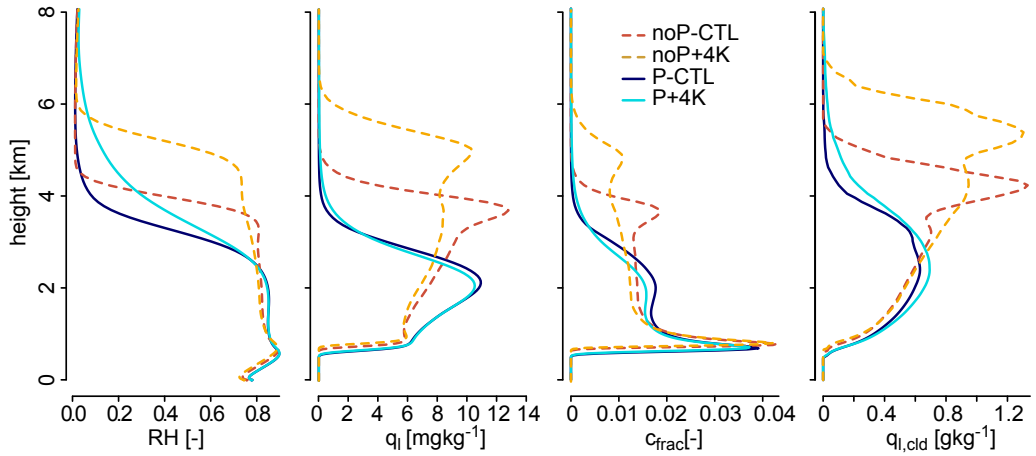

Figure 2.6.: Domain-averaged profiles of relative humidity RH, domain-mean liquid water q_l, cloud fraction c_{frac} and conditionally-averaged cloud water $q_{l,cld}$. Shown are P (solid) and noP (dashed) for both the CTL and +4K climate states. The profiles for the P simulations are averages over day 7-10, the noP profiles are averages over day 7.

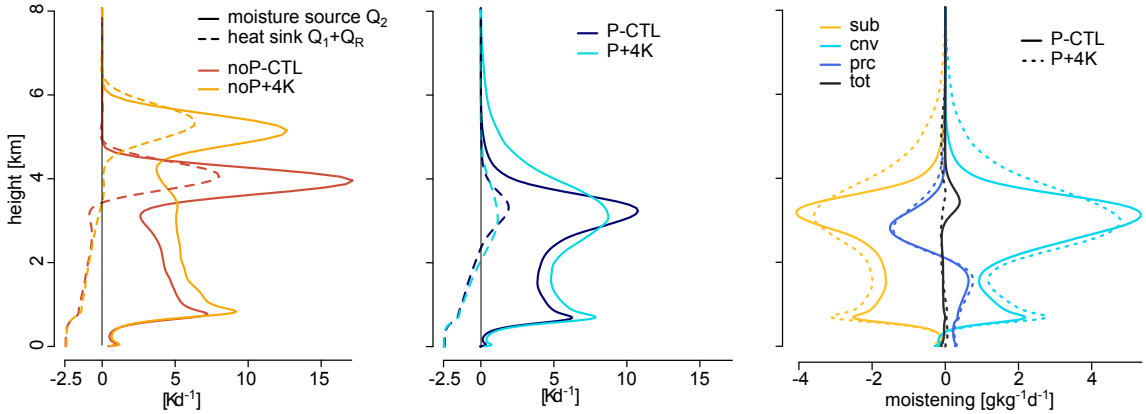

Figure 2.7.: Profiles of the heat sink (Q_1+Q_R, dashed) and moisture source (Q_2) for the CTL and +4K climate states of the noP cases (left, averages of day 7 are shown) and the P cases (middle). (right) Individual moistening tendencies of the P-CTL and P+4K simulations.

by ∼11.5 % relative to P-CTL between about 1 and 3.2 km. This reduction is caused by clouds being more concentrated in the warmer climate, carrying the same amount of liquid over smaller areas, what $q_{l,cld}$ is proof of (Fig. 2.6). Between 1.8 and 3.2 km, the reduction is also consistent with a somewhat weaker inversion, which reduces the accumulation of cloud below the inversion. Because the contribution of the deeper clouds to cloud fraction above 3.2 km is small, total cloud cover reduces by ∼1.5 % with warming (Table 2.2). Similar to the non-precipitating case, the albedo decreases from 0.080 to 0.071 in spite of a slight increase in liquid water path. Whereas changes in the vertical distribution of clouds may be more pronounced, the small magnitude of the overall reduction in cloud cover and albedo emphasizes that the real story may more be the robustness of the low clouds with warming, rather than their change.

The small sensitivity of cloud-base cloud fraction to warming is apparent in both the P and noP case (see CF_{max} in Table 2.2). The same was shown in the LES intercomparison of *Blossey et al.* (2013) (see their Figure 22), but stands in contrast to the behavior of parameterizations in climate models that mainly reduce cloud fraction close to the base of the shallow clouds (*Brient et al.*, 2015). Moreover, *Brient et al.* (2015) note that models with large cloud fractions near the lifting condensation level reduce cloudiness more effectively in response to warming, and therefore have a higher climate sensitivity. Observations also show that climate models may not capture the right modes of variability in cloudiness in the present-day climate, namely parameterizations tend to vary cloudiness near the base of the cumulus layer more readily with changes in the large-scale state than is observed (*Nuijens et al.*, 2015b).

The last panel of Fig. 2.7 shows that the enhanced convective moistening, and not an enhanced precipitation tendency, maintains the equilibrium in the P+4K case. Some more precipitation forms in P+4K from the deeper clouds above 3.2 km, which slightly enhances both the moistening in the cloud layer and surface precipitation (Table 2.2). The large domain simulations presented in the next section will show that precipitation tendencies change with warming in the presence of deeper convection.

2.5. Impact of Deeper Convection

To address the hypothesis that convective organization may change the response of shallow clouds to warming we perform simulations on a sixteen-fold larger (that is, a $51.2 \times 51.2\,km^2$) domain. In the first subsection, we show how the spatial organization into larger clusters influences the vertical structure of the trade-wind boundary layer using the CTL simulations. Subsection 2.5.2 then discusses how this modulates the warming response.

2.5.1. Influence of Deeper Convection on the Trade-Wind Layer Structure

Whilst the boundary layer deepening and surface fluxes of the Plarge-CTL case develop similarly as on the small domain for the first 2 days, they begin to differ when some deeper clouds form that produce substantial precipitation and trigger large cold pools (see Fig. 2.8). Spreading cold pools trigger subsequent, deeper convection at the cold-pool front through a combination of thermodynamic and dynamic perturbations (something commonly referred to as cold-pool dynamics (e.g. *Schlemmer and Hohenegger*, 2014)). This deeper convection reaches the top of the domain at 10 km already after 2.5 days. Fig. 2.9 shows snapshots of the cloud albedo of the different cases to illustrate the different horizontal structures of the cloud fields. The Plarge-CTL case (d) shows a strong separation into clear and cloudy patches. A spreading cold pool triggers uplift at the cold-pool front, where the subsequent clouds form along the arc-like structure of this front.

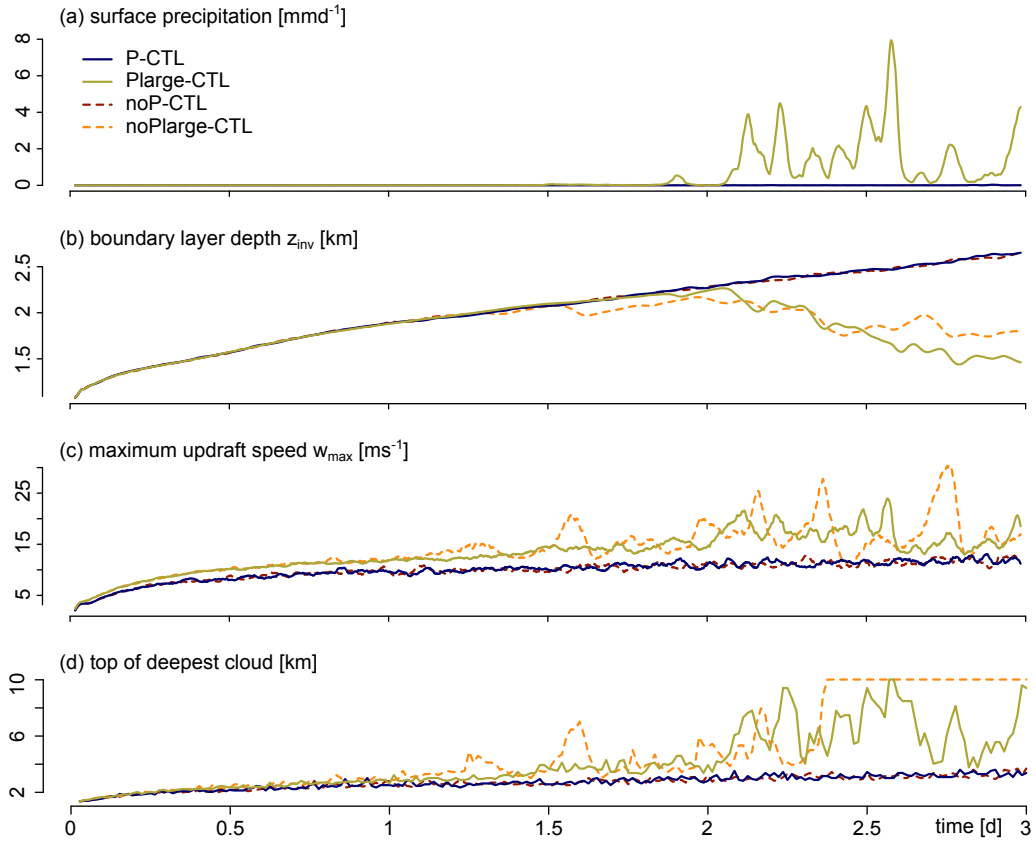

Figure 2.8.: Domain-averaged timeseries for the precipitating (solid) and non-precipitating (dashed) CTL cases on the small ($12.8\times12.8\text{km}^2$) and large ($51.2\times51.2\text{km}^2$) domain.

In contrast to the horizontal structures found in Plarge-CTL, both the noP-CTL (a) and P-CTL (b) simulations show little evidence of spatial organization. The larger clouds producing substantial precipitation on the small domain still generate cold pools, but the domain is too small for these cold pools to introduce an organization of the temperature and humidity field.

Because the development of deeper convection in Plarge-CTL may be somewhat artificial, we performed a simulation with a uniform 4 K cooling at constant relative humidity (see Table 2.1). The surface latent heat flux of this simulation is $190\,\text{W}\,\text{m}^{-2}$ and indeed, no clouds deeper than 6.5 km form (not shown). Nevertheless, the clouds reaching up to about 6 km in the Plarge−4K case represent larger and deeper clusters that influence the trade-wind layer in a similar way as the 10 km deep clouds in Plarge-CTL. The idea that the development of much deeper convection in Plarge-CTL may be artificial is also explored by relaxing some of the assumptions in the simplified setup. Not only the latent heat fluxes, but also the uniform radiative cooling of $-2.5\,\text{Kd}^{-1}$ in the free troposphere represents a strong forcing promoting the development of deeper clouds. In an additional simulation of Plarge-CTL with interactive radiation (IRAD Plarge, see Table 2.1 for fur-

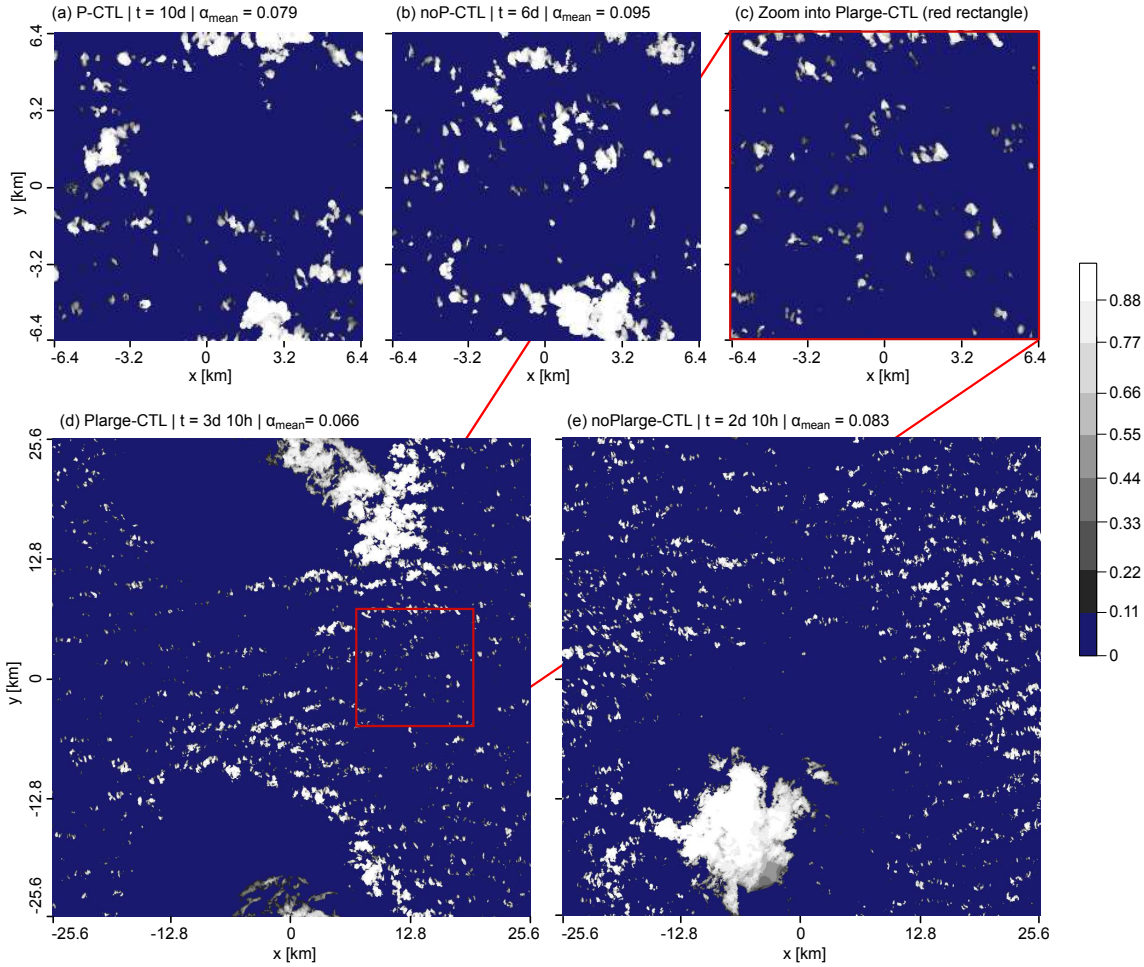

Figure 2.9.: Snapshots of cloud albedo: (a) and (b) show the small domain ($12.8\times12.8\text{km}^2$) P-CTL and noP-CTL, (d) and (e) the large ($51.2\times51.2\text{km}^2$) domain Plarge-CTL and noPlarge-CTL simulations. (c) displays a zoom into a $12.8\times12.8\text{km}^2$ region of Plarge-CTL. The recording time and the mean albedo of the respective field are indicated.

ther specifications), radiative cooling in the free troposphere reduces by 1-1.5 $\text{K}\,\text{d}^{-1}$, which stabilizes the free troposphere and suppresses deep convection (see the dotted black line in Fig. 2.10). The transition to deeper convection, and its surprising sensitivity to domain size, clearly merits more study (see e.g. *Kuang and Bretherton* (2006) and *Böing et al.* (2012) for investigations into the transition from shallow to deep cumulus convection). Here we simply take advantage of the simulations to study the impact of deeper convection on the equilibrium trade-wind layer structure and warming response, the main purpose of this work.

The profiles in Fig. 2.10 show a strong impact of the presence of deeper clouds on the thermodynamic structure of the trade-wind layer. Comparing the two CTL simulations

(solid lines), we find that the trade-wind clouds become much shallower in Plarge-CTL. Whereas the deep clouds increase relative humidity beyond 8 km, the shallower trade-wind layer becomes much drier. Both the temperature and humidity lapse rates are larger and the trade-wind layer thus more stable. The drier layer results in less condensate-laden clouds, with lower cloud fraction throughout the shallow cloud layer, albeit least pronounced near cloud base, consistent with the previous results. The liquid water path and total cloud cover decrease to 25 g m^{-2} and 9.1 % respectively (see Table 2.3) and the albedo reduces from 8 % to 4.9 %.

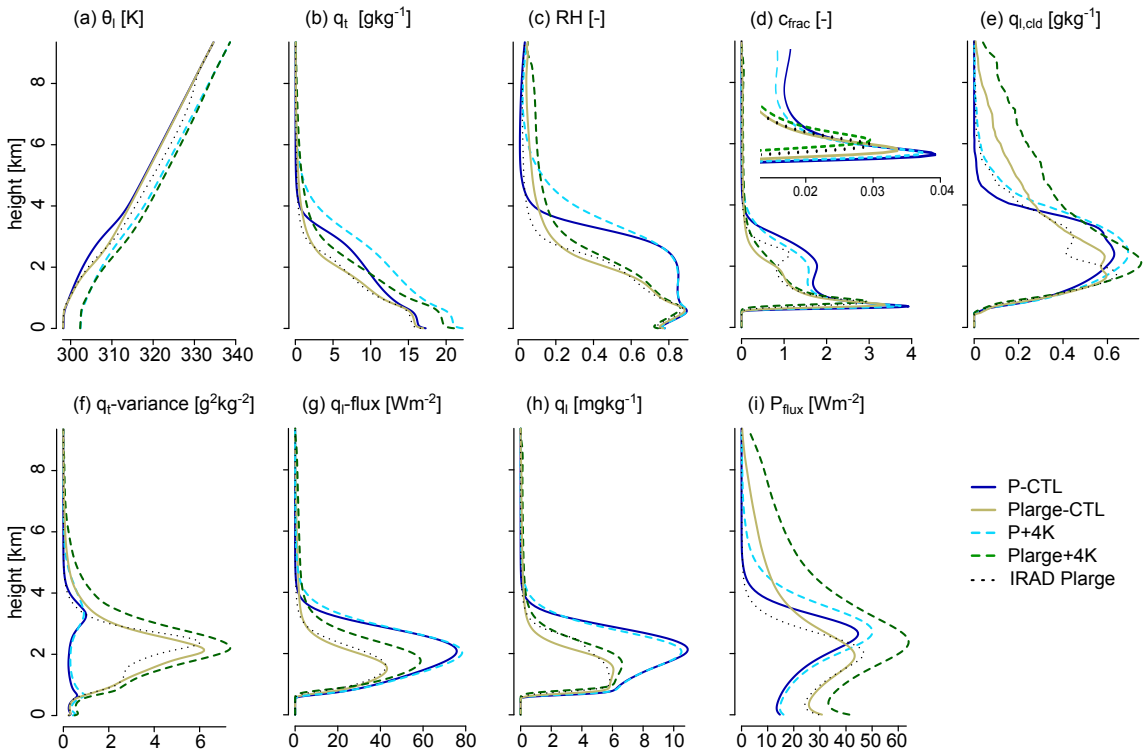

Figure 2.10.: Domain-averaged vertical profiles of the (a) liquid water potential temperature θ_l, (b) total humidity q_t, (c) relative humidity RH, (d) cloud fraction $\mathrm{c_{frac}}$ (with a zoom into the cloud base region), (e) conditionally-averaged cloud water $q_{\mathrm{l,\,cld}}$, (f) variance of total water q_t, (g) liquid water q_l-flux, (h) domain-mean liquid water q_l and (i) precipitation flux P_flux. Shown are again both P and Plarge for the CTL (solid) and the +4K (dashed) climate states, along with the interactive radiation simulation IRAD Plarge (dotted).

Surface precipitation doubles from P-CTL to Plarge-CTL despite a decrease in domain-average liquid water and similar precipitation rates close to the inversion in the two simulations (see Table 2.3 and Fig. 2.10 i). This increase in surface precipitation is associated with a decrease in the number of precipitating columns in the domain. As most of the precipitation comes from the small areas of deep convection, there is a greater distinction between the precipitating and non-precipitating areas. The larger variance of total water

Table 2.3.: Averages of surface latent heat flux (LHF), surface precipitation rate (P_{surf}), integrated subsidence drying (D), integrated residual moistening tendency (DT), surface sensible heat flux (SHF), boundary layer depth (z_{inv}), cloud cover (CC), liquid water path (LWP), albedo (α), maximum cloud fraction (CF_{max}), fraction of columns with precipitation (P_{frac}), and maximum vertical velocity (w_{max}); for small domain (P) and large domain (Plarge) precipitating simulations of both the CTL and +4K climate states.

case	LHF [Wm^{-2}]	P_{surf} [Wm^{-2}]	D [Wm^{-2}]	DT [Wm^{-2}]	SHF [Wm^{-2}]	z_{inv} [m]	CC [%]	LWP [gm^{-2}]	α [%]	CF_{max} [%]	P_{frac} [%]	w_{max} [ms^{-1}]
P-CTL	251	15	-236	1	0.7	2633	13.5	36.4	8.0	3.9	1.7	12.2
Plarge-CTL	262	29	-220	12	2.7	1620	9.1	25.0	4.9	3.4	1.0	14.8
P+4K	310	16	-302	-8	-2.3	2056	11.9	40.6	7.1	3.7	1.8	13.0
Plarge+4K	371	42	-281	49	-0.5	1747	7.8	41.1	4.6	3.0	1.3	19.4

is evidence of a larger contrast in humidity between the clear and cloudy columns. Precipitation from the deeper aggregated clouds tends to fall through moister environments, reducing evaporation in the on-average drier trade-wind layer. By stabilizing the shallow trade-wind layer and enhancing subsidence in the non-precipitating areas, the deep convection arising from the convective clusters effectively keeps the remainder of the clouds shallow. In energetic terms, the doubling of surface precipitation to $1\,\mathrm{mm\,d^{-1}}$ constitutes about a $15\,\mathrm{W\,m^{-2}}$ reduction of energy compared to P-CTL, which is roughly compensated by the $13\,\mathrm{W\,m^{-2}}$ increase of the latent heat flux. The precipitation characteristics of the Plarge-CTL case are similar to observations during RICO, when average precipitation amounts of $1\,\mathrm{mm\,d^{-1}}$ were observed, with larger rain rates associated with arc-shaped structures forming on what appeared to be cold-pool boundaries (*Rauber et al.*, 2007; *Snodgrass et al.*, 2009).

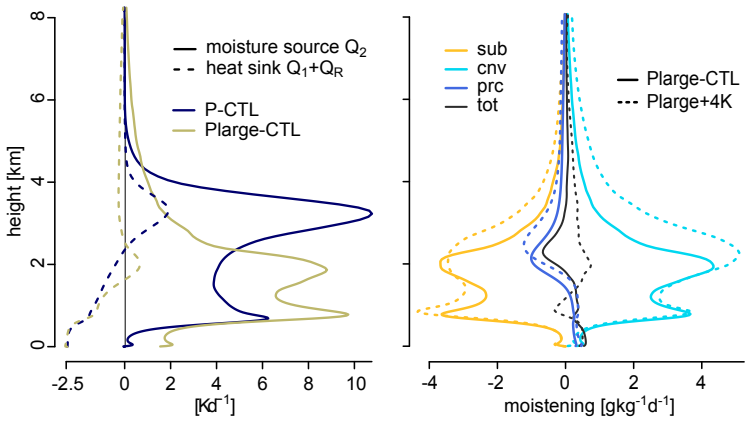

Figure 2.11.: (left) Profiles of the heat sink ($Q_1 + Q_R$, dashed) and moisture source (Q_2, solid) for P-CTL and Plarge-CTL, and (right) the individual moistening tendencies of the Plarge-CTL (solid) and Plarge+4K (dashed).

The left panel of Fig. 2.11 shows that besides the lowering of the maxima of cooling and moistening in the inversion layer, the moisture source at cloud base is stronger than

in the inversion layer for Plarge-CTL. Cloud base moistening is strongly enhanced in the Plarge-CTL case, likely because of the larger stratification across cloud base due to the drier domain-mean cloud layer, which corresponds to larger convective moistening that balances the enhanced subsidence drying. Further, due to the drier sub-cloud layer, Q_2 is also enhanced below cloud base.

Hence, by simulating on a sixteen-fold larger domain and allowing for mesoscale organization, a very different convection regime emerges, which manifests itself in the thermodynamic structure of the trade-wind layer and in cloudiness and precipitation characteristics.

The warming and drying of the trade-wind layer associated with the emergence of deep convection in the large domain simulation is not exclusive to the precipitating case: also in noPlarge-CTL, deep convection forms and the trade-wind layer warms and dries (see Fig. 2.8 d and Fig. A.1 e, f). Fig. 2.9 (e) displays a snapshot of noPlarge-CTL, which shows a certain separation of clear and cloudy regions on a scale comparable to the domain size. As the non-precipitating deep clouds do not generate cold pools, no mesoscale arcs are formed and the effect of deep clouds on their immediate surroundings is less evident than is the case for Plarge-CTL.

The simulations are a reminder that although cold-pool dynamics may often be an important impetus for deep convection, they are not necessary for its development (*Jeevanjee and Romps*, 2013; *Muller and Bony*, 2015), even in situations where we initially did not anticipate the development of deep clouds. There are no cold pools that can trigger deeper convection at colliding cold-pool boundaries, but in the absence of precipitation, more cloud liquid water evaporates and moistens the environment directly surrounding the updraft. Via entrainment, the moister ambient air promotes the deepening of convection through positive moisture-convection feedbacks (see the discussion in Appendix A). Although not directly related to the objectives of this study, one curious aspect of the simulations is why the larger domain allows deeper convection to form, which then completely reorganizes the flow and in particular the thermodynamic structure near the surface. On a larger domain, larger maximum updraft speeds are realized from the beginning of the simulation (see Fig. 2.8 c). *Bjerknes* (1938) provides a dynamical argument how stronger and deeper updrafts can be maintained on larger domains, by spreading their compensating subsidence over broader areas and therefore reducing the effective stability felt by the updraft. A larger domain may also sample rare events somewhat better, thereby increasing the likelihood of deeper clouds forming somewhere. Both of these mechanisms may play a role and are explored in more detail in Appendix A.

2.5.2. Warming Response

By permitting the emergence of convective aggregation, the increase of the domain size has a much stronger effect on the trade-wind boundary layer than the 4 K warming itself. Fig. 2.10 shows that the shape of the q_t and θ_l profiles of Plarge-CTL and Plarge+4K are similar, along with more similar relative humidity, liquid water, cloud fraction, q_t-variance and to some extent also precipitation flux profiles.

With warming, the amount of deep clouds is enhanced on the large domain, as seen from the increased relative humidity beyond 2 km. The deep clouds strongly enhance the precipitation flux and lead to a much stronger increase of surface precipitation with warming on the large domain (see Table 2.3). From an energetic point of view this can be understood by noting that the integrated subsidence drying in the dry shallow Plarge+4K trade-wind layer cannot increase enough to balance the strongly enhanced latent heat flux, which implies that larger precipitation drying is needed. Under warming, precipitation therefore has a stronger role in balancing the convective tendencies in the presence of a few deep clouds that effectively shallow and dry the trade-wind layer in regions away from deep convection. One deleterious effect of the deep convection is that longer time and larger spatial scales are introduced, and as a result the simulations are further away from stationarity. The Plarge+4K case has a particularly strong residual moistening tendency of about $49\,\mathrm{W\,m^{-2}}$.

Total cloud cover reduces from 9.1 % to 7.8 % with warming, comparable to the reduction on the small domain (Table 2.3). Both the weakening of the inversion, reducing the stratiform component near cloud tops (Fig. 2.10 d), and the slight reduction of cloud fraction near the cumulus bases contribute to this reduction. Similar to the small-domain precipitating case, the warmer climate state supports larger liquid water contents within clouds (Fig. 2.10 e). So although the domain-averaged liquid water increases slightly, the cloud fraction goes down. Previous LES studies show that entrainment feedbacks can prevent the liquid-water flux from increasing much with a climate perturbation (*Bretherton and Blossey*, 2014). Namely, the increased buoyancy with larger liquid water content leads to more entrainment across the inversion, and this additional drying and warming can reduce the liquid water content again. This is true for our non-precipitating simulations (not shown), and also the precipitating small domain simulations show only a small increase in the liquid-water flux with warming (Fig. 2.10 g). But on the large domain, an increase in liquid-water flux with warming is much more pronounced, because a few larger and deeper clouds carry most of the liquid across the inversion, making the entrainment feedback far less efficient.

Despite the strong influence of deeper convection on the trade-wind layer structure and dynamics, the overall cloud response to warming, and the processes causing them, remain similar as on the small domain—with the exceptions of the stronger role of precipitation in

balancing the enhanced convective moistening and the slight deepening of the trade-wind layer (Table 2.3). Because the liquid water path increases much more with warming on the large domain (related to the more strongly enhanced latent heat flux), the albedo reduction is smaller. As mentioned in the previous section, we also performed an experiment with a uniform 4 K cooling (at constant relative humidity), which indicates that similar mechanisms act between the CTL and the +4K climate state, and respectively the −4K and the CTL climate state (not shown). Moreover, also the mechanisms among the small and large domain simulations are similar, increasing the robustness of the results.

2.6. Conclusions

The response of shallow trade-wind convection to warming is studied with a special interest in how precipitation and organization of moist convection into deeper clusters modulate this response. Large-eddy simulations representative of present-day trade-wind conditions are compared to runs with a 4 K uniform warming at constant relative humidity. The effect of precipitation is assessed by either allowing or inhibiting the formation of precipitation, and by allowing mesoscale structures associated with precipitation to form through simulations on much larger domains.

As cloud fraction has its maximum near the cumulus bases, the near-base insensitivity to warming present in all cases considered partly masks the more pronounced changes that occur in the vertical distribution of cloud fraction. Different, albeit related mechanisms control the vertical distribution of cloudiness in the presence or absence of precipitation. In the non-precipitating case, the slight relative drying of the deeper boundary layer in the +4K climate state causes both a reduced cloud fraction between 1.5 and 4 km and a weaker stratiform component at cloud tops. Because of an opposing tendency to convection in the inversion layer and the evaporation of precipitation in the lower cloud layer, precipitation efficiently buffers the warmer cloud layer against deepening and relative drying. Cloud fractions between 1 and 3.2 km still decrease, owing to two mechanisms: (a) the clouds become more concentrated, that is they carry the same amount of liquid over a smaller area, and (b) the inversion weakens, reducing the stratiform cloud component in the inversion layer. Previous studies pointed out the importance of precipitation in limiting the boundary layer deepening with warming and thereby affecting the sensitivity of shallow cumulus clouds to climate perturbations (*Bretherton et al.*, 2013; *Blossey et al.*, 2013). Here, we link these ideas to processes that maintain the budgets of heat and moisture. We find that convective moistening in the warmer climate state, fueled by the larger latent heat flux, increases strongly to balance the enhanced subsidence drying caused by the increased humidity gradient between the surface and the free troposphere. The precipitation drying only replaces subsidence drying as the latter becomes less effective in the presence of a

few deeper cloud clusters and an overall shallower and drier trade-wind layer on the large domain.

Overall, the increase of domain size—and thus the spatial organization of shallow convection into larger and deeper clusters—has a much stronger effect on the trade-wind layer than the 4 K warming. Simulations with the same setup on a sixteen-fold larger domain ($51.2\times51.2\,\mathrm{km}^2$) support the spatial organization of clouds into clusters that get as deep as the domain top at 10 km. By stabilizing the boundary layer and enhancing subsidence in the non-precipitating areas, the presence of the deeper clouds results in a shallower, drier and warmer equilibrium trade-wind layer. Also the moisture source (Q_2) and heat sink ($\mathrm{Q}_1 + Q_\mathrm{R}$) are altered, with a strongly enhanced moisture source in the sub-cloud layer, at cloud base and above the trade-wind layer inversion. The emergence of deep convection on larger domains, although unintended and perhaps somewhat sensitive to the case setup, renders closer to observations the thermodynamic structure of the large domain precipitating control simulation, its precipitation characteristics and horizontal structure (e.g. *Rauber et al.*, 2007; *Zuidema et al.*, 2012; *Stevens et al.*, 2016). The development of larger and deeper clouds in larger domain simulations is not exclusive to precipitating simulations, but also occurs in the non-precipitating large domain case, with a similar influence on the thermodynamic structure of the trade-wind layer. In the absence of cold pools, moisture-convection feedbacks strengthen and the updrafts developing in moister regions preconditioned by previous convection continue to be strong, by entraining moister ambient air.

With warming, cloud cover and albedo decrease in all cases considered. This would, all else being equal, constitute a positive cloud feedback in the shallow cumulus regime. The albedo thereby decreases in spite of increasing liquid water paths, because reductions in total cloud cover tend to more than offset increases in liquid water. Nevertheless, the albedo reductions are small. If we take the global average cloud radiative effects of about $-20\,\mathrm{W\,m^{-2}}$ (*Boucher et al.*, 2013) as representative of trade-wind regimes (assumed to cover a third of the oceans), and suppose changes in cloud radiative effects scale with changes in albedo, then we see a 6−11 % reduction in cloud radiative effects in our precipitating simulations for a 4 K warming. The lower and upper bound of this reduction stem from the different albedo reductions in the large and small domain simulations respectively. The simple calculation thus gives us a change in cloud radiative effects of about 0.1 to 0.18 $\mathrm{W\,m^{-2}\,K^{-1}}$, that is, a robustly positive but likely much smaller change than one finds in global models (*Boucher et al.*, 2013). A particular insensitivity to warming is found for cloudiness near the base of the cumulus layer. This is in line with recent observations (*Nuijens et al.*, 2015b), but in contrast to some global models which reduce cloudiness near cumulus bases more readily with warming and therefore suggest a high climate sensitivity (*Brient et al.*, 2015). Our simplified setup exposes important mechanisms

shaping the warming response of precipitating shallow convection, and confirms previous studies suggesting a positive radiative feedback in the shallow cumulus regime. But our results indicate that the positive feedback is likely to be small, which is a demonstration of the insensitivity of precipitating shallow convection to changes in the environment. This insensitivity is shown to persist even in the presence of deep convection that substantially changes the structure of the trade-wind layer in larger domain simulations.

Chapter 3

Changes in precipitation, cloudiness and trade-wind layer structure from the winter to the summer trades

Abstract

Using large-eddy simulation we explore factors influencing the seasonal cycle of cloudiness and precipitation at Barbados. The increase in sea-surface temperature and decrease in large-scale subsidence in a summer-like simulation leads to deeper clouds, a quadrupling of precipitation and a 15% relative decrease in cloud cover compared to a more winter-like simulation, resembling the observed seasonal changes. Three separate processes which may contribute to the seasonal changes are addressed in more detail, being (1) moisture-radiation interactions, (2) surface forcing and (3) large-scale subsidence. First, interactive radiation is important to form and maintain thin stratiform layers near cumulus tops under a strong inversion. The stratiform layers develop from condensate-detrainment of deeper precipitating clusters, and strong radiative cooling in a confined layer helps stabilize the inversion. However, if strong radiative cooling is distributed over a broad layer, it contributes to the deepening of convection. This happens under a drier free troposphere, where stronger integrated radiative cooling—together with a larger latent heat flux—promotes the deepening of convection. The convective deepening leads to an increase in precipitation and a weakening of the inversion, which inhibits stratiform cloud layers. Second, the winter regime is also characterized by stronger wind and stronger cold-air advection. Both perturbations increase precipitation and cloudiness by building up relative humidity

during intermittent periods and in confined regions. Third, an increase in prescribed subsidence reduces precipitation, but does not enhance cloudiness near the inversion. Overall, the deepening of trade cumulus clouds and the increase in precipitation exert a dominant influence on diminishing the inversion structure and inhibiting the formation of stratiform layers, largely independent of the specific factors responsible for the deepening.

3.1. Introduction

Observations from the Barbados Cloud Observatory (BCO) indicate that the winter regime at Barbados has more low cloud cover than the summer regime (*Nuijens et al.*, 2014; 2015a; *Brueck et al.*, 2015). The larger low cloud cover in winter is caused by larger contributions to projected cloud cover from cloudiness near the trade-wind inversion around 2 km (see Fig. 1.3 in the introduction and *Nuijens et al.* (2014)), which is either due to the presence of stratiform layers near cumulus tops, sheared deeper trade cumulus or remnants of decaying clouds. In the winter regime, the development of stratiform layers is more common when clouds are deeper and precipitate more (*Nuijens et al.*, 2014; *Lamer et al.*, 2015). Contrastingly, deeper clouds and more precipitation can also be accompanied with less cloud cover. For instance, when the intertropical convergence zone (ITCZ) is located closer to Barbados during boreal summer, and convection deepens and precipitation increases, the region has less low cloud cover (*Nuijens et al.*, 2015a; *Brueck et al.*, 2015). Here we use large-eddy simulations (LES) to explore how factors related to the large-scale forcings and to convection itself influence the seasonal cycle of cloudiness and precipitation in the trades.

Changes in the large-scale forcings are an important control on the seasonal cycle of cloudiness and precipitation. From boreal winter to boreal summer, the free-tropospheric humidity increases, the subsidence regime shifts from moderately subsiding to moderately rising motion, the trade winds weaken, and sea surface temperatures (SSTs) increase at Barbados (*Brueck et al.*, 2015). The stronger trade inversion and the stronger wind speed in the winter regime might explain the observed increase in cloudiness in winter (*Klein*, 1997; *Brueck et al.*, 2015; *Nuijens et al.*, 2015a). But observed correlations between individual large-scale factors and low cloud cover are weak in the trade cumulus regime, particularly on timescales shorter than a month (*Brueck et al.*, 2015; *Nuijens et al.*, 2015a).

The depth of convection is another factor which might influence the seasonal cycle of cloudiness and precipitation. In Chapter 2 we showed that the spontaneous organization of shallow convection into deeper and larger precipitating clusters leads to a shallower, warmer, and drier domain-average trade-wind layer. Total cloud cover decreased by more than 30% relative to a simulation on a 16-fold smaller domain without organization, mainly because of reduced cloud fractions in the upper cloud layer under the weaker inversion.

Based on BCO observations, *Nuijens et al.* (2015a) hypothesised that the depth of trade cumuli might play a subtle role in controlling cloudiness near cumulus tops and thus low cloud cover in the trades, in the sense that cloud cover increases when trade cumuli deepen but still maintain a limited depth such that the trade inversion structure is preserved. To understand the factors controlling the seasonal cycle of cloudiness, it is thus also important to understand how specific large-scale factors influence the propensity of shallow convection to organize and deepen.

This study investigates the influence of large-scale forcing factors and of convective deepening on the seasonal cycle of cloudiness and precipitation in the trades. We address the following research questions: 1. How does interactive radiation help explain differences in cloudiness between the winter and summer regime? 2. How much does the deepening and organization of convection mediate the cloud response to changes in the large-scale forcings? We perform LES with a model domain of $51.2\times51.2\times10\,\mathrm{km}^3$ which was shown to be large enough to support shallow convective organization and the emergence of cumulus congestus (e.g. *Seifert and Heus*, 2013). The initial and boundary conditions of the simulations are inspired by some of the above-mentioned observations, which are made at Barbados in the Western North-Atlantic. The trade cumulus layer at Barbados is usually between 1.5 and 3 km deep and not necessarily capped by a temperature inversion. So we use the term inversion to refer to the pronounced humidity gradient (hydrolapse) at the top of the cumulus layer.

We address three important large-scale factors that might explain the seasonal changes in more detail. They are (1) moisture-radiation interactions, (2) surface forcing, and (3) large-scale subsidence. In the first set of simulations, we study the impact of radiation on the character of convection under a dry versus a moist initial free troposphere. In the second set of simulations, we study the effect of increasing wind speed and adding horizontal advective cooling, both of which alter the surface fluxes. In the third set of simulations, we study the impact of prescribed subsidence, a constraint we omit by also calculating subsidence interactively using the weak temperature gradient approximation (WTG, *Sobel and Bretherton* (2000)). As shallow convection deepens and precipitates more, we are moving from a purely radiative-subsidence equilibrium in the free troposphere towards a radiative-convective equilibrium. Thereby, subsidence should decrease in response to stronger heating from precipitation, such that the free-tropospheric heat balance is maintained. Previous work investigated the influence of changes in specific large-scale factors such as wind speed, large-scale subsidence or free-tropospheric humidity on the trade-wind layer structure with models of varying complexity (*Betts and Ridgeway*, 1989; *Albrecht*, 1993; *Nuijens and Stevens*, 2012; *Bretherton et al.*, 2013). But these studies did not represent the variability introduced by shallow-convective organization, or they neglected precipitation completely. Our simulation setup therefore opens new ways for a better un-

derstanding of the processes shaping the response of precipitating shallow convection to changes in the large-scale flow.

The next section describes the LES framework and the numerical experiments performed. Section 3 provides an overview of the simulations, followed by Section 4 which discusses the three sets of simulations performed in more detail. Conclusions are presented in Section 5.

3.2. Large-eddy simulation framework and experiments

3.2.1. LES framework

All the simulations are performed with the University of California Los Angeles (UCLA) LES (*Stevens et al.*, 2005), in a similar setup as in Chapter 2. The UCLA LES solves the Ogura–Phillips anelastic equations using finite differences and applies the Smagorinsky–Lilly model for the subgrid-scale fluxes. Prognostic equations are solved for the three wind components and the two thermodynamic variables total water mixing ratio q_t and liquid water potential temperature θ_l. Time-stepping is performed with a third-order Runge–Kutta integration. Liquid water is diagnosed with a saturation-adjustment scheme. Microphysical processes are based on the two-moment warm rain scheme of *Seifert and Beheng* (2001; 2006), as described in *Savic-Jovcic and Stevens* (2008). A constant cloud droplet number concentration $N_\mathrm{c} = 50\ \mathrm{cm}^{-3}$ is assumed. Ice microphysical processes are not considered.

The large-scale thermodynamic state is based on an idealized representation of the conditions in the broader trades, adapted from *Bellon and Stevens* (2012). The setup uses a Eulerian reference frame and prescribes homogeneous large-scale forcings. The forcings include an exponential subsidence profile

$$w(z) = -w_0 \left(1 - e^{-z/H_\mathrm{w}}\right), \tag{3.1}$$

where $w(z)$ is the subsidence rate at height z, w_0 is the prescribed base subsidence rate serving as asymptotic value at high altitude (default value $w_0 = 7.5\ \mathrm{mm\,s^{-1}}$), and $H_\mathrm{w} = 1$ km is the scale height. Like in the standard configuration of *Bellon and Stevens* (2012), the free-tropospheric temperature lapse-rate follows from the balance of the prescribed uniform radiative cooling tendency, $Q_\mathrm{R,uni} = -2.5\ \mathrm{K\,d^{-1}}$, and the subsidence rate $w(z)$ as

$$\frac{\mathrm{d}\theta_\mathrm{l}}{\mathrm{d}z} = \frac{Q_\mathrm{R,uni}}{w(z)}. \tag{3.2}$$

The surface sensible and latent heat fluxes (SHF and LHF) are modeled using the

following bulk formulas:

$$\mathrm{SHF} = C_D U(\theta_{\mathrm{l,s}} - \theta_{\mathrm{l,m}}) \tag{3.3}$$

$$\mathrm{LHF} = C_D U(q_{\mathrm{t,s}} - q_{\mathrm{t,m}}), \tag{3.4}$$

where m denotes values at the second model level (in the well-mixed sub-cloud layer), $\theta_{\mathrm{l,s}}$ is the fixed SST with a default value of 300 K and $q_{\mathrm{t,s}}$ the corresponding saturation specific humidity. C_D is the surface transfer coefficient derived from similarity theory and U the surface wind speed. A constant geostrophic zonal wind u_{g} is imposed, with a default value of $10\,\mathrm{m\,s^{-1}}$. No horizontal advective cooling and drying tendency is applied in the standard setup.

Except for two simulations applying the prescribed height-independent radiative cooling of $-2.5\,\mathrm{K\,d^{-1}}$, the radiative tendency is computed interactively. The interactive radiation tendency is based on the broadband radiation code of *Fu and Liou* (1992) and uses Monte Carlo Spectral Integration (*Pincus and Stevens*, 2009), similar to the implementation of *Seifert et al.* (2015). The radiative cooling tendency is computed for every column independently, based on the specific profiles of water vapor, temperature and liquid water. The profiles are blended to a typical tropical profile from the domain top at 10 km to the top of the atmosphere. A fixed solar zenith angle of 15° is used for the short-wave component. To avoid spin-up problems, the prescribed uniform radiative cooling of $-2.5\,\mathrm{K\,d^{-1}}$ is used during the first simulation hour.

A grid spacing of 50 m in the horizontal and 10 m in the vertical is used, with the vertical grid uniformly stretched by a factor of 1.02. All the simulations are performed on a $51.2\times51.2\times10\,\mathrm{km^3}$ domain (1024×1024×155 grid points) with doubly-periodic lateral boundary conditions.

3.2.2. Numerical experiments

Table 3.1 provides an overview of the different experiments performed. Two different initial free-tropospheric humidity profiles are used, a *CTL* and an on average 1–1.5 $\mathrm{g\,kg^{-1}}$ drier *DRY* profile. Both profiles have the same boundary layer humidity ($13\,\mathrm{g\,kg^{-1}}$ for $z < 1\,\mathrm{km}$, followed by a linear decrease to $4\,\mathrm{g\,kg^{-1}}$ at $z = 1.6\,\mathrm{km}$), but use a different scale height for the exponential free-tropospheric humidity profile

$$q_{\mathrm{t,ft}}(z) = q_0 e^{-z/H_{\mathrm{q}}}, \tag{3.5}$$

where $H_q = 5\,\mathrm{km}$ for the *CTL* cases and $H_q = 2\,\mathrm{km}$ for the *DRY* cases, and $q_0 =$

Table 3.1.: Specifications used in the different experiments. Free-tropospheric humidity profile, geostrophic wind component u_g, base subsidence rate ω_0, radiation treatment, SST, horizontal advective cooling rate, and averaging time of statistics. '*' refers to simulations that have been perturbed after 3 days from the baseline simulation with the same initial humidity profile.
[1]The *DRY.wtg.rlx* simulation uses a height-dependent relaxation of the domain-averaged humidity profile back to its initial profile. Refer to the text for details.

case name	q_t prof	u_g [$m\,s^{-1}$]	ω_0 [$mm\,s^{-1}$]	Q_R	SST [K]	adv. cool [$K\,d^{-1}$]	Δt [d]
CTL.2K.ω6	CTL	10	6	interactive	302	0	2.5-4.5
CTL	CTL	10	7.5	interactive	300	0	3.5-5.5
DRY	DRY	10	7.5	interactive	300	0	3-5
CTL.unirad	CTL	10	7.5	$-2.5\,K\,d^{-1}$	300	0	2.5-4.5
DRY.unirad	DRY	10	7.5	$-2.5\,K\,d^{-1}$	300	0	2.5-4
DRY.cool	DRY	10	7.5	interactive	300	−0.75	3.5-5.5*
DRY.u15	DRY	15	7.5	interactive	300	0	4-6*
DRY.ω8.5	DRY	10	8.5	interactive	300	0	4-6*
DRY.u15.ω8.5	DRY	15	8.5	interactive	300	0	4-6*
CTL.u15	CTL	15	7.5	interactive	300	0	4-6*
CTL.2K	CTL	10	7.5	interactive	302	0	5.5-7.5*
DRY.wtg	DRY	10	WTG	interactive	300	0	2-3
DRY.wtg.rlx	DRY	10	WTG[1]	interactive	300	0	2-3

$4\,g\,kg^{-1}$. The *CTL* and *DRY* simulations with the different initial humidity profiles, but everything else according to the standard setup described above, serve as a baseline for most of the other simulations. The simulations denoted with a '*' in the last column of Table 3.1 are restarted after 72 h of the baseline simulations with the same initial humidity profile. After 3 days, the major characteristics of the baseline simulations have evolved, and typical trade-wind structures become apparent (not shown).

The influence of wind speed is explored in the simulations *CTL.u15*, *DRY.u15*, and *DRY.u15.ω8.5* by increasing the zonal geostrophic wind u_g from $10\,m\,s^{-1}$ to $15\,m\,s^{-1}$. The influence of large-scale subsidence is studied by increasing the prescribed base subsidence rate w_0 to $8.5\,mm\,s^{-1}$, and by applying the WTG approximation as discussed in the next paragraph. The influence of horizontal advective cooling is studied in the *DRY.cool* case, which applies a horizontal advective cooling tendency of $0.75\,K\,d^{-1}$. The influence of increasing SST is investigated in the *CTL.2K* case with a 2 K SST increase. The *CTL.2K.ω6* simulation has a similar 2 K SST increase plus a $1.5\,mm\,s^{-1}$ reduction in subsidence applied. Unlike the other simulations with perturbations applied to the standard setup, *CTL.2K.ω6* is not restarted after 3 d of the *CTL* case, but started from initial conditions.

To understand how the large-scale subsidence influences precipitating shallow convection, we perform two simulations (denoted *DRY.wtg* and *DRY.wtg.rlx*) in which the large-scale subsidence rate is computed following the WTG balance (*Sobel and Bretherton*, 2000). We follow the implementation of *Raymond and Zeng* (2005) and compute subsidence as follows:

$$w_{\mathrm{wtg}}(z) = \frac{\lambda_t \left(1 - e^{-z/H_{\mathrm{w}}}\right) \left[\bar{\theta}_{\mathrm{l}}(z) - \theta_{\mathrm{l},0}(z)\right]}{\mathrm{d}\bar{\theta}_{\mathrm{l}}/\mathrm{d}z}, \tag{3.6}$$

where λ_t is the relaxation timescale set to $(2\,\mathrm{h})^{-1}$, the term in the round brackets represents the height-dependent relaxation rate with scale height $H_{\mathrm{w}} = 1$ km (as used to compute the prescribed subsidence rate in equation 3.1), and $\left[\bar{\theta}_{\mathrm{l}}(z) - \theta_{\mathrm{l},0}(z)\right]$ describes the difference of the domain-averaged temperature from its initial value. The WTG simulations are initialized using the domain-averaged temperature and humidity profiles of the *DRY.unirad* simulation averaged after 24 ± 2 h.

Because the WTG approximation breaks down in the trade-wind layer where horizontal temperature gradients can be larger, the subsidence rate needs to be interpolated from the top of the inversion layer down to the surface. From 5 km down to 3 km, we therefore linearly transition from pure WTG to pure prescribed subsidence according to equation 3.1, with a w_0 derived from the mean w_{wtg} between 3 and 5 km. As will be shown in Section 3.4.3, w_{wtg} is much smaller than the prescribed subsidence rate, which strongly reduces subsidence drying, and leads to a residual moistening tendency. We therefore perform an another simulation with the same WTG setup, but an additional relaxation of the free-tropospheric humidity profile back to its initial profile (*DRY.wtg.rlx*). The height-dependent relaxation is implemented similar to *Schlemmer et al.* (2011), with

$$\left.\frac{dq_{\mathrm{t}}}{dt}\right|_{\mathrm{relax}} = -\frac{\bar{q}_{\mathrm{t}} - q_{\mathrm{t},0}}{\tau} \cdot 0.5 \left[1 - erf\left(\frac{3500 - z}{750}\right)\right], \tag{3.7}$$

where $q_{\mathrm{t},0}$ is the initial humidity profile, $\tau = 6$ h is the timescale of relaxation, z is the height, and erf is the error function.

We perform all the simulations for several days and attempt to approach stationarity. However, due to the interactive radiation and the emergence of organized shallow convection, residual heating tendencies in the upper cloud layer and the free-troposphere, and residual moistening tendencies in the upper cloud layer persist even if the sub-cloud layer reached stationarity. We therefore chose the near-equilibrium averaging periods for the different simulations such that the tendencies in the sub-cloud layer and lower cloud layer are approximately in balance (see the last column of Table 3.1 for the averaging periods used). In the few simulations that develop deep convection reaching the domain top at 10 km (the *CTL.2K.ω6*, *DRY.u15.ω8.5*, *CTL.unirad*, and *DRY.unirad* simulation), the q_{t}-profiles are nudged towards their initial profiles in the six highest model levels to prevent the accumulation of liquid water at the domain top.

To study the moistening from precipitating shallow convection, we compute the moisture source Q_2 following *Yanai et al.* (1973). Because shallow convection acts as a net moisture source, we inverted the sign of Q_2 compared to the original definition, and compute Q_2 as follows:

$$Q_2 := \frac{L}{c_p}\left[\left.\frac{\partial \bar{q}_t}{\partial t}\right|_{\text{tot}} + \omega \left.\frac{\partial \bar{q}_t}{\partial z}\right|_{\text{sub}}\right] = \frac{L}{c_p}\left[\left.\frac{\partial \bar{q}_t}{\partial t}\right|_{\text{cnv}} + \left.\frac{\partial \bar{q}_t}{\partial t}\right|_{\text{prc}}\right]. \tag{3.8}$$

The terms on the left-hand side represent the storage term ('tot') and the contribution from large-scale subsidence ('sub'), and the terms on the right-hand side the contributions from the turbulent flux divergence ('cnv') and precipitation ('prc'). The tendencies are multiplied by the enthalpy of vaporization, L, and divided by the isobaric specific heat capacity of dry air, c_p.

3.3. Range of precipitation and cloud cover responses

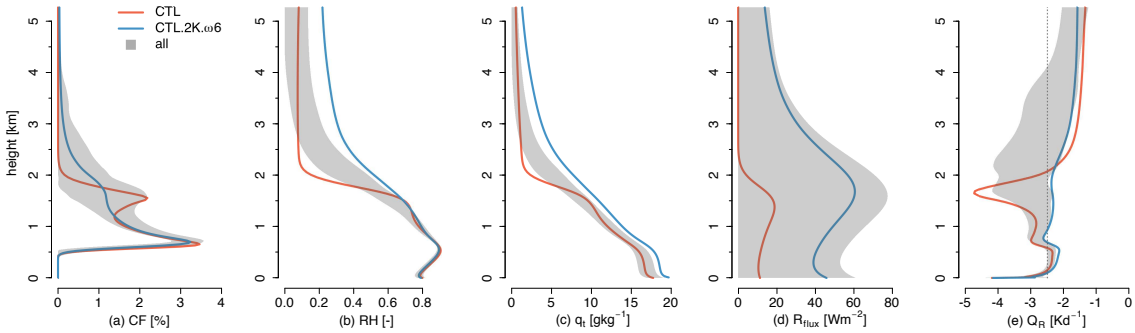

Figure 3.1.: Domain-averaged profiles of (a) cloud fraction, (b) relative humidity (RH), (c) total humidity, (d) precipitation flux, and (e) radiative cooling for the *CTL* case (red) and the *CTL.2K.ω6* case (blue). The shading represents the mean $\pm 1\sigma$ of all simulations performed (see Table 3.1).

Fig. 3.1 presents the two simulations that have the smallest (*CTL*) and largest (*CTL.2K.ω6*) near-equilibrium precipitation rate, which roughly resemble the winter and summer trades, such as seen in the observed profiles in Fig. 1.3. The difference between the cases is that *CTL.2K.ω6* uses 2 K larger SST and $1.5\,\mathrm{mm\,s^{-1}}$ weaker subsidence. So the *CTL.2K.ω6* may be more like a suppressed period in summer, because it still has prescribed subsidence, whereas Barbados experiences mean rising motion in summer (*Brueck et al.*, 2015; *Stevens et al.*, 2016). Other factors that might be different between the two seasons (wind speed, free-tropospheric humidity, horizontal advection) are kept the same. The vertical profiles in Fig. 3.1 show that the most salient features of the observed seasonal cycle at Barbados (see Fig. 1.3) are captured when changing the SST and subsidence rate: a

deeper moist trade-wind layer with a pronounced stratiform cloud layer at 1.5–2 km under a relatively strong inversion in the winter-like *CTL* case; a moister free troposphere, more precipitation, a stronger humidity lapse rate in the cloud layer, and a weaker inversion in the more summer-like *CTL.2K.ω6* case. The higher total projected cloud cover of 11.2% in *CTL* compared to 9.4% in *CTL.2K.ω6* is mostly due to the differences in cloudiness at the inversion. Cloudiness near cloud base is insensitive to the changes in the large-scale state (see also *Nuijens et al.* (2014; 2015b) and Chapter 2).

One major difference between observations and LES is that the LES underestimates total cloud cover by more than 50% compared to the Barbados Cloud Observatory, where a low cloud cover of more than 30% is observed (*Nuijens et al.*, 2014). This underestimation can be due to numerical diffusion (*Matheou et al.*, 2011), the use of an 'all-or-nothing' cloud scheme within each grid-cell, as well as the underestimation of variability in the cloud field on longer time scales due to homogeneous and constant large-scale forcings (see *Vial et al.* (2017) for a review of the robustness of simulated cloudiness in LES). Also the surface precipitation rate is underestimated compared to Barbados (Fig. 1.3), which is partly related to residual drying and warming tendencies present in many of the simulations due to the relatively strong prescribed subsidence.

The larger precipitation flux in the summer-like *CTL.2K.ω6* case can be attributed to a few deeper clouds reaching the domain top at 10 km. The convection in *CTL.2K.ω6* is deeper because of the increased SST, which reduces the stability and increases the surface fluxes, and because of the reduced warming and drying tendency from large-scale subsidence. Chapter 2 shows how the development of larger and deeper cloud clusters in simulations with a large domain size of $51.2\times51.2\times10\,\mathrm{km}^3$ exerts a strong influence on the trade-wind layer structure. In these simulations, deeper convection organized into a larger cluster with large humidity mixed over a deep layer and substantial precipitation, while the rest of the cloud field was suppressed, resulting in a shallower, drier, and warmer lower troposphere away from the deeper convection, capped by a weaker inversion and with reduced cloud cover compared to a simulation with a 16-fold smaller domain (see Chapter 2).

Similar to the deep convective simulations analysed in Chapter 2, 10 km deep convection develops in the *CTL.2K.ω6* simulation. The lower troposphere in the *CTL.2K.ω6* simulation is less stable and cloud fractions near the top of the shallow cloud layer are reduced compared to *CTL* (Fig. 3.1). In contrast, the *CTL* simulation with the lower SST and the stronger subsidence does not develop deep convection and rains about 4-fold less than *CTL.2K.ω6*, but maintains a strong inversion. The *CTL* simulation has a larger cloud cover, which is mainly due to larger cloud fraction under the more pronounced inversion. This might be expected from the simulations of the ATEX case (*Stevens et al.*, 2001), and from the well-known relationship between inversion strength and cloud cover in the

upstream trades where stratocumulus prevails (*Klein and Hartmann*, 1993). Fig. 3.1 e furthermore shows that the *CTL* simulation has a strong radiative cooling peak right at the inversion layer, reminiscent of stratocumulus decks.

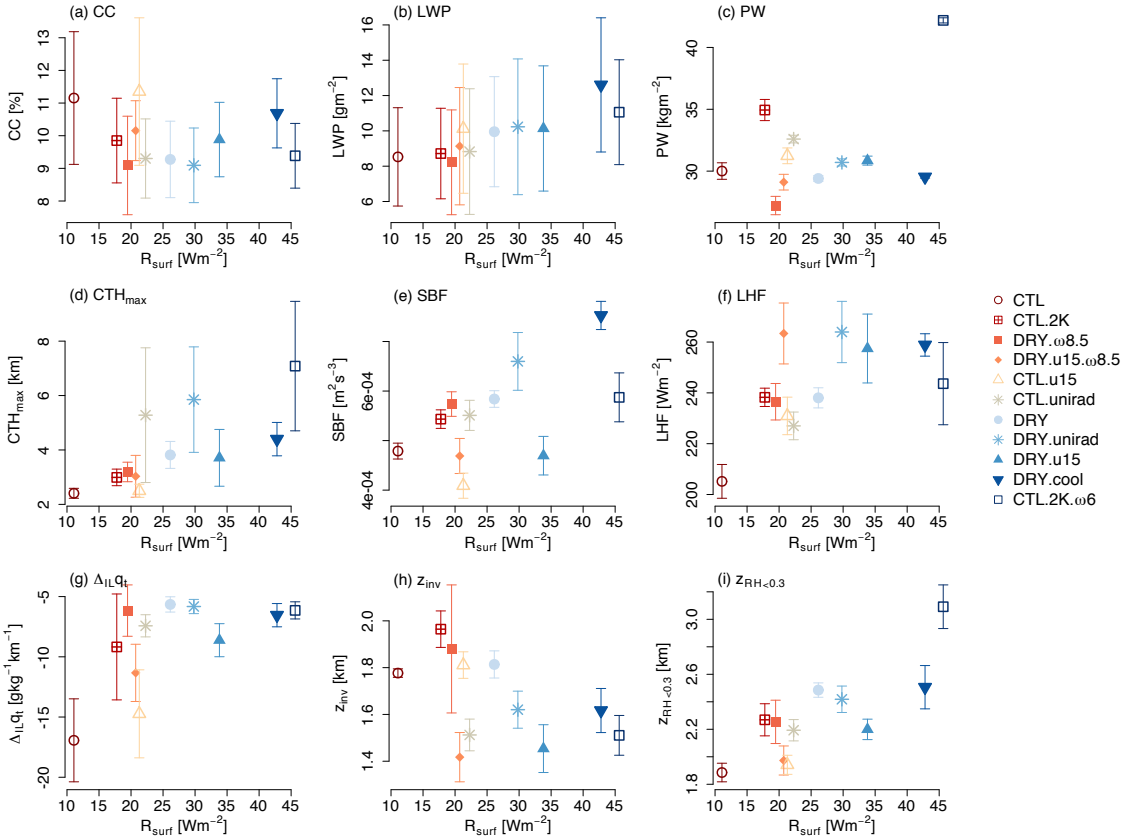

Figure 3.2.: Scatterplots of surface rain rate versus (a) cloud cover, (b) liquid water path, (c) precipitable water, (d) maximum cloud top height, (e) surface buoyancy flux, (f) LHF, (g) the jump in total humidity between ±200 m of the inversion depth, (h) the inversion depth, and (i) the height where the domain-averaged RH decreases below 30 %. The symbols represent the mean and the whiskers represent the temporal variability ($\pm 1\sigma$) in the near-equilibrium regime of the simulations (see Table 3.1 for the averaging periods of individual simulations).

The shading in Fig. 3.1 represents the range of simulated cloud, precipitation and humidity profiles across the different simulations performed (see Table 3.1), which have average surface precipitation rates that lie in between the winter and summer cases. The scatterplots in Fig. 3.2 shows how the domain-averaged and time-averaged cloud cover, liquid water path, precipitable water, maximum cloud top height, surface buoyancy flux, LHF, and the inversion strength and inversion depth of these simulations change as a function of precipitation, which is plotted on the x-axis. The simulations are colored from red to blue indicating increasing surface precipitation (this color coding will be used in other figures as well).

The scatterplots indicate that cloud cover tends to decrease with surface precipitation

(Fig. 3.2 a). Increases in precipitation are associated with deeper clouds (3.2 d), and a weaker inversion (3.2 g). Only 2 out of 11 simulations maintain a strong inversion with enhanced cloudiness at the inversion (*CTL* and *CTL.u15*). Panel 3.2 h shows that the inversion depth z_{inv}, computed from the maximum θ_l gradient at individual grid columns, tends to decrease with surface precipitation, and has a maximum value of about 2 km. Contrastingly, the depth of the moist layer, defined as the height where the domain-averaged relative humidity (RH) becomes less than 30% ($z_{RH<0.3}$), increases with surface precipitation and the depth of convection (3.2 i). Only for the simulations with a relatively strong inversion, like *CTL* and *CTL.u15*, do the two definitions lead to similar inversion depths. In the presence of deeper and organized cloud clusters, which cover moist regions with weaker temperature lapse rates, the inversion depth z_{inv} is not a representative measure of the depth of the cloud field anymore. We therefore use $z_{RH<0.3}$ to refer to the depth of the moist cloud layer. We further define the layer from the surface to the top of the trade cumulus layer as the trade-wind layer.

Whereas precipitation and the liquid water path are well-correlated (3.2 b, see e.g. *Kubar et al.* (2009) or *Jiang et al.* (2010)), precipitation does not increase with precipitable water (3.2 c), counter to our intuition and recent observations (see e.g. *Bretherton et al.*, 2004; *Holloway and Neelin*, 2009; *Nuijens et al.*, 2009). In fact, the simulations with a drier initial free troposphere (labeled '*DRY...*') tend to precipitate more than the simulations labeled as '*CTL...*', which have a somewhat moister (initial) free troposphere. This is related to the dependence of the surface fluxes and radiative cooling rates on the free-tropospheric humidity (see Section 3.4.1).

Precipitation is also well-correlated with the surface buoyancy flux (3.2 e), which appears as an important control on the deepening of clouds (3.2 d). The SHF plays a key role in increasing the surface buoyancy flux while precipitation increases, because the LHF levels off and does not increase much beyond 260 $\mathrm{Wm^{-2}}$ (3.2 f). Exceptions are the simulations with stronger wind speed (*CTL.u15*, *DRY.u15*, and *DRY.u15.ω8.5*), which develop a negative SHF, so that despite a large LHF, their buoyancy flux and maximum cloud tops are smaller. On the other hand, the three simulations with stronger wind, along with the simulation with cold-air advection (*DRY.cool*), tend to have large cloudiness despite relatively strong surface precipitation (3.2 a).

In the remainder of the paper we discuss these results in more detail, and explain the mechanisms behind the relationships we observe. The next sections present the three groups of simulations performed, including those that address moisture–radiation interactions (3.4.1), the influence of surface forcing (3.4.2), and large-scale subsidence (3.4.3).

3.4. Sensitivity to large-scale forcings, initial and boundary conditions

3.4.1. How drier atmospheres tend to precipitate more: the influence of radiation

Our winter-like *CTL* simulation ends up being much drier than the summer-like *CTL.2K.ω6* simulation, despite their identical initial humidity profile. This shows just how important deeper convection is in moistening the free troposphere. In this section, we study how convection responds to an external perturbation in free-tropospheric humidity. The initial profiles of both the '*CTL*' and the perturbed '*DRY*' cases are relatively dry, and their difference is modest: about $1.5\,\mathrm{g\,kg^{-1}}$ between 2–6 km (see the insets in Fig. 3.3 b, c for the initial humidity profiles belonging to the '*CTL*' and '*DRY*' simulations). Fig. 3.2 showed that the '*DRY*' simulations tend to have stronger LHF, deeper clouds and more precipitation than the '*CTL*' simulations. Why the drier atmospheres enhance precipitation can be explained by the influence of free-tropospheric humidity on both the surface fluxes and the radiative heating rates. To this end we compare the temporal evolution of the *CTL* and the *DRY* simulations when they are performed with prescribed uniform radiation, and with interactive radiation.

With uniform radiation, the trade-wind layer deepens slightly faster in the *DRY.unirad* case as compared to *CTL.unirad* (dashed lines in Fig. 3.4 b), which is due to greater evaporative cooling. The enhanced deepening leads to stronger entrainment drying across the inversion, and increases the LHF (Fig. 3.4 a). Whereas the *CTL.unirad* simulation starts to precipitate after about 24 h, the *DRY.unirad* case only starts to produce substantial precipitation after 48 h, when the inversion is about 400 m deeper than in *CTL.unirad*. With the onset of precipitation, the inversion depths cease to deepen and become shallower, so that in a quasi-stationary state, the *DRY.unirad* case is only slightly deeper than the *CTL.unirad* case (Fig. 3.3 b). Also the RH structures and the cloud fraction profiles are very similar between the uniform radiation simulations (Fig. 3.3 a, b). However, as a result of stronger surface fluxes, the *DRY.unirad* case has a larger precipitation flux than *CTL.unirad* (Table 3.3 and Fig. 3.3 d). In the *DRY.unirad* simulation, the drying from precipitation becomes more important to balance the enhanced surface LHF, because the drying from large-scale subsidence is in-efficient as the atmosphere is already very dry (see *Seifert et al.*, 2015). Table 3.3 shows that the integrated precipitation tendency, which equals the surface precipitation rate, is $7\,\mathrm{Wm^{-2}}$ larger than in *CTL.unirad*, whereas the integrated subsidence drying is only about $1.5\,\mathrm{Wm^{-2}}$ larger.

While the *DRY.unirad* and the *CTL.unirad* case using prescribed radiation look overall much alike, this is not true when running the same setup with interactive radiation. In Fig. 3.3 the difference in the cloud profile and the thermodynamic structure is much more

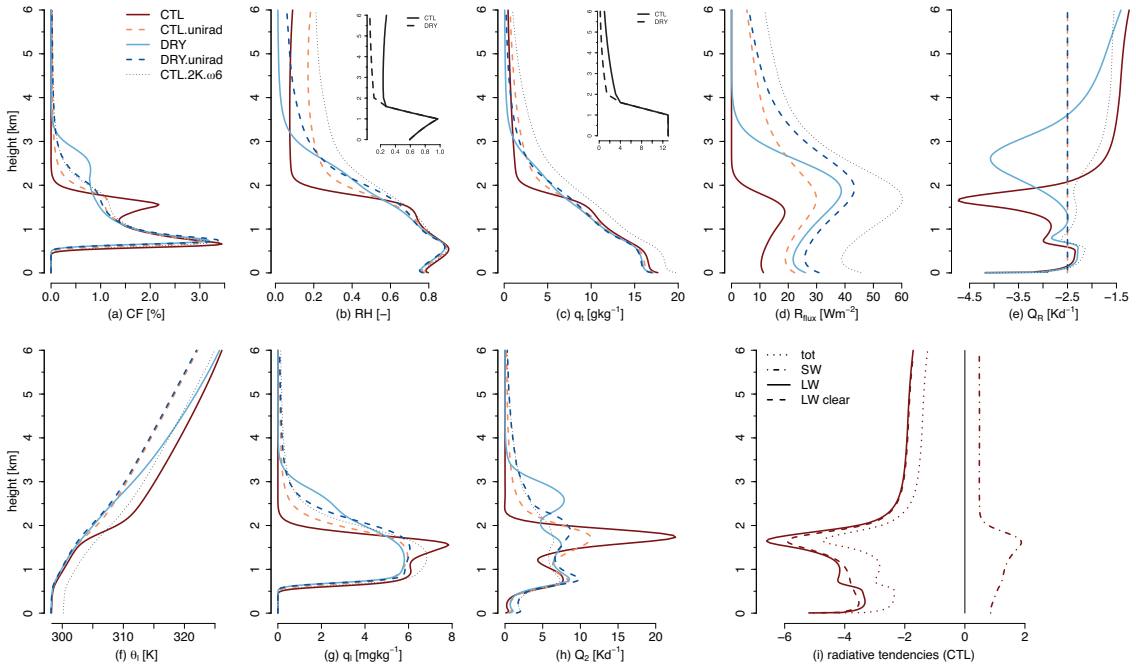

Figure 3.3.: Domain-averaged profiles of (a) cloud fraction, (b) RH, (c) total humidity, (d) precipitation flux, (e) radiative heating, (f) liquid water potential temperature, and (h) moisture source Q_2 for the *CTL*, *DRY*, *CTL.unirad*, and *DRY.unirad* simulation. Panel (i) shows different contributions to the total radiative heating tendency (dotted) of the *CTL* case, namely the tendency due to shortwave radiation (dashed-dotted), longwave radiation (solid), and clear-sky longwave radiation (dashed). The insets in panel b and c represent the initial humidity profiles for the *'DRY'* and *'CTL'* cases respectively. The thin dotted line represents the summer-like *CTL.2K.ω6* simulation, which is plotted as reference.

pronounced between the *CTL* (solid red, already used in Fig. 3.1) and *DRY* (light blue) cases using interactive radiation. This is because the radiative cooling of the layer now depends on the water vapor and the cloud structure. Whereas the cloud layer in the *DRY* case becomes deeper and has larger cloudiness up to 3 km compared to *DRY.unirad* (Fig. 3.3 a, b, c), the *CTL* case ends up having a somewhat shallower cloud layer than *CTL.unirad*, accompanied with a much stronger inversion and a large second peak in cloudiness which starts to resemble the stratiform outflow layers observed at Barbados during winter (see Fig. 1.3).

Both the *CTL* and the *DRY* case have less radiative cooling in the free troposphere, as compared to the dashed prescribed radiative cooling profile in Fig. 3.3 e. Because subsidence is prescribed and does not reduce in response to the lower radiative cooling rates, the free troposphere warms and stabilizes (Fig. 3.3 f), and deeper clouds do not develop. This explains why the RH above 3 km is lower and there is less surface precipitation compared to the respective prescribed radiation cases (Fig. 3.3 b, d). But within the cloud layer, and at the surface, radiative cooling is larger than in the prescribed radiation cases (Fig. 3.3 e).

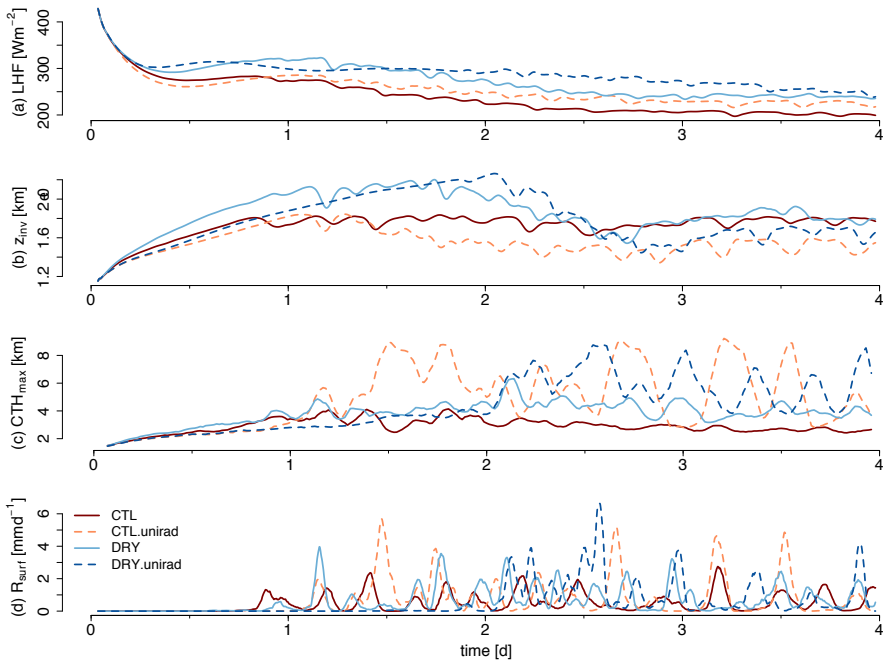

Figure 3.4.: Timeseries of (a) domain-averaged surface LHF, (b) inversion depth, (c) maximum cloud top height, and (d) surface precipitation rate for the *CTL*, *CTL.unirad*, *DRY*, and *DRY.unirad* simulations.

Fig. 3.3 i shows that the strong long-wave cooling is mainly a clear-sky response. Cloud radiative effects contribute to the cooling at cloud tops, and induce a slight warming in the sub-cloud layer. The overall enhanced radiative cooling in the cloud layer leads to a larger destabilization and a more rapid deepening of individual clouds and the inversion in the beginning of the simulations (see Fig. 3.4 c, similar to what was first shown in *Seifert et al.* (2015)). Because the drier free troposphere in the *DRY* simulation is more transparent to longwave radiation, the radiative cooling rate at the top of the moist cloud layer in the beginning of the simulation is strongly enhanced compared to the *CTL* case (Fig. 3.5 a). Together with the enhanced evaporative cooling, the enhanced radiative cooling leads to a much faster deepening of convection in *DRY* than in *CTL*, and a joint onset of precipitation after 1 d in the interactive radiation cases (Fig. 3.4 d). The deepening of shallow convection under a drier free-troposphere due to stronger surface evaporation and stronger radiative cooling was also shown with a simple bulk-equilibrium model (*Betts and Ridgeway*, 1989) .

The interaction of the water vapor and the cloud field with radiation also has a stabilizing effect, which helps form the more pronounced peaks in cloudiness near cloud tops (Fig. 3.3 a). This is particularly true for the *CTL* simulation, but also the *DRY* simulation tends to develop slightly larger cloudiness near cumulus tops compared to *DRY.unirad*. We further illustrate this with Fig. 3.5, which shows the temporal evolution of the domain-averaged radiative heating tendency (3.5 a), the cloud fraction profile (with

dashed contours for precipitation) (3.5 b), and the moisture source Q_2 profile (3.5 c). The timeseries on the left correspond to the interactive radiation *CTL* case, which has a pronounced second peak in cloudiness at the inversion, the timeseries in the middle show the prescribed radiation case *CTL.unirad*, and the timeseries on the right show the *DRY* case with interactive radiation. Fig. 3.5 b shows that, because of the limited domain size, the outflow layers in *CTL* are intermittent features, rather than a persistent feature that is constant in time. Fig. 3.5 b also shows that regions of stratiform cloudiness are associated with the presence of deeper clouds, rather than with the absence of deeper clouds, because the peak in cloudiness near cloud tops arises always after the occurrence of slightly deeper clouds. The vertical reference lines in Fig. 3.5 show that the pronounced outflow co-occurs with strong radiative cooling (Fig. 3.5 a) and with strong drying above the cloud layer (Q_2 switches from positive to negative in Fig. 3.5 c).

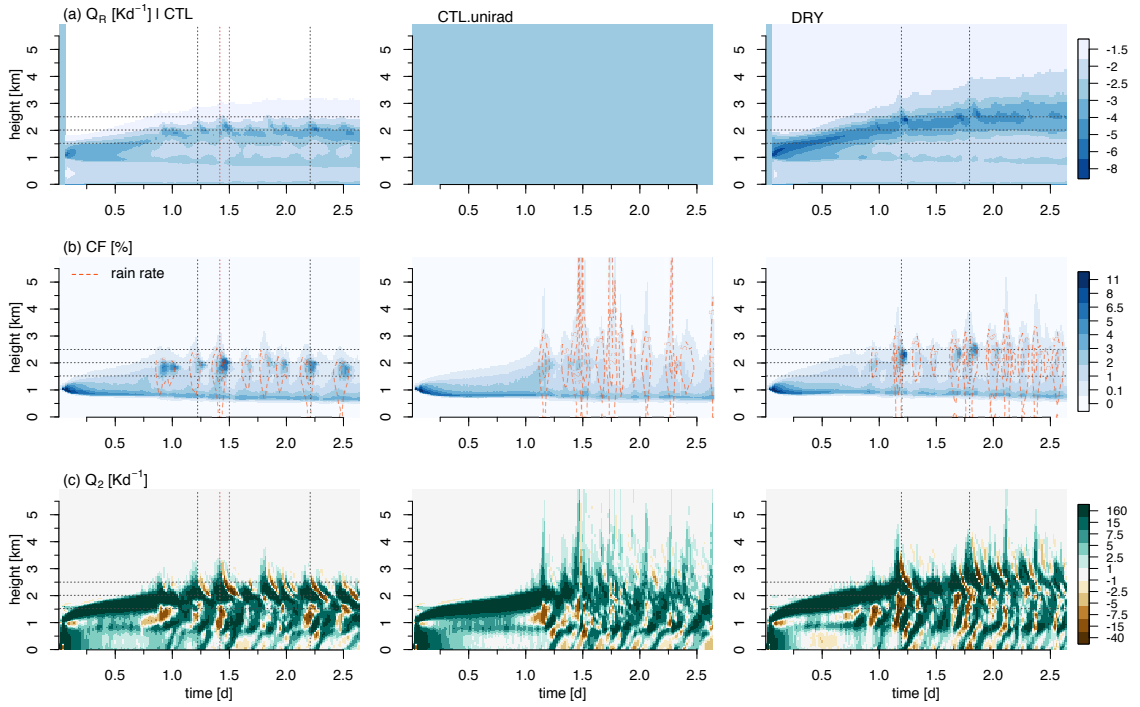

Figure 3.5.: Temporal evolution of domain-averaged profiles of the radiative heating tendency Q_R (top), cloud fraction (middle), and moisture source Q_2 (bottom), for the *CTL* (left), the *CTL.unirad* (middle), and the *DRY* simulation (right). Contour lines in the cloud fraction panels represent the precipitation rate in intervals of 5, 12.5, and 20 mg kg^{-1}. Horizontal and vertical reference lines are added to facilitate the comparison of features across the different variables. The two reference lines in darkred in the *CTL* panel correspond to the timesteps used for Fig. 3.6.

To better understand the development of the stratiform layers, Fig. 3.6 presents 2 D cross-sections and conditional profiles for two timesteps of the *CTL* simulation, at the growing stage of the deeper cloud cluster (t=1.42 d), and 2 h later, at the stage of mature outflow (t=1.5 d, as indicated by the darkred reference lines in the left column of Fig. 3.5).

Fig. 3.6 a shows that the congestus clouds with tops up to 4 km form as part of a larger cluster of individual updrafts. Already at this stage, condensate-detrainment from the deep cluster produced a considerable stratiform layer with an average thickness of about 400 m (Fig. 3.6 a, b). 2 h later, the congestus clouds disappeared and only the very thin outflow layers remain (Fig. 3.6 f, g). The moistening due to convection and precipitation accumulated during the two hours, and integrated from 1.5 km to 4 km (Fig. 3.6 c), shows that the drying above cloud tops evident in Fig. 3.5 c occurs right where the deepest clouds are located at t=1.42 d. Contrastingly, the area where the mature outflow is located at t=1.5 d experienced a net moistening in the two hours. Fig. 3.6 d displays vertical profiles of Q_2 conditioned on the two areas highlighted by the red contours in 3.6 c, which represent the location of the deep cluster at t=1.42 d ('area1'), and the area of the mature outflow at t=1.5 d ('area2'). For area1, the Q_2 profile shows the strong drying which extends over the entire cloud layer. Whereas about 20% of this drying is due to precipitation, the bulk of the drying is due to mixing or compensating subsidence induced by the deepest turrets. Compensating subsidence might be triggered by strong evaporative and radiative cooling across the strong inversion. The cross-section in Fig. 3.6 h demonstrates that the area of deeper convection and strong outflow has a much stronger integrated radiative cooling tendency between 1.5–4 km than the rest of the domain. The conditional profiles in Fig. 3.6 i show that this strong radiative cooling is concentrated in a narrow band near 2 km. The strong radiative cooling in the inversion layer stabilizes the layer above cloud tops, and maintains the outflow.

But what the results also appear to suggest is that the larger and deeper clusters themselves, through mixing and cooling-induced subsidence, help strengthen the inversion locally, which prevents subsequent updrafts from going deep. Hence, subsequent moisture transport into the cloud layer builds up moisture and forms larger cloud fractions under the strong inversion. The temperature and humidity profiles conditioned on area2 provide some evidence that the humidity and temperature inversion strengthens in the two hours considered (Fig. 3.6 e, j), coincident with the moistening and radiative cooling experienced (Fig. 3.6 d, i). The cold pool triggered by the cluster eventually stops the supply of moisture by subsequent updrafts, but the stratiform layers can persist for more than an hour due to the strong longwave cloud-radiative cooling across the inversion, which promotes saturation.

The important role of interactive radiation in the outflow formation is also manifest in the *CTL.unirad* case, where the presence of deeper clouds does not produce dry downdrafts and outflow layers (Fig. 3.5 b, c *middle*), likely because radiative cooling is prescribed and uniform. The results correspond to what is observed at Barbados, namely that the presence of stratiform outflow is enhanced when shallow convection tends to be deeper and more organized (*Nuijens et al.*, 2014; *Lamer et al.*, 2015). On the basis of individual cloud

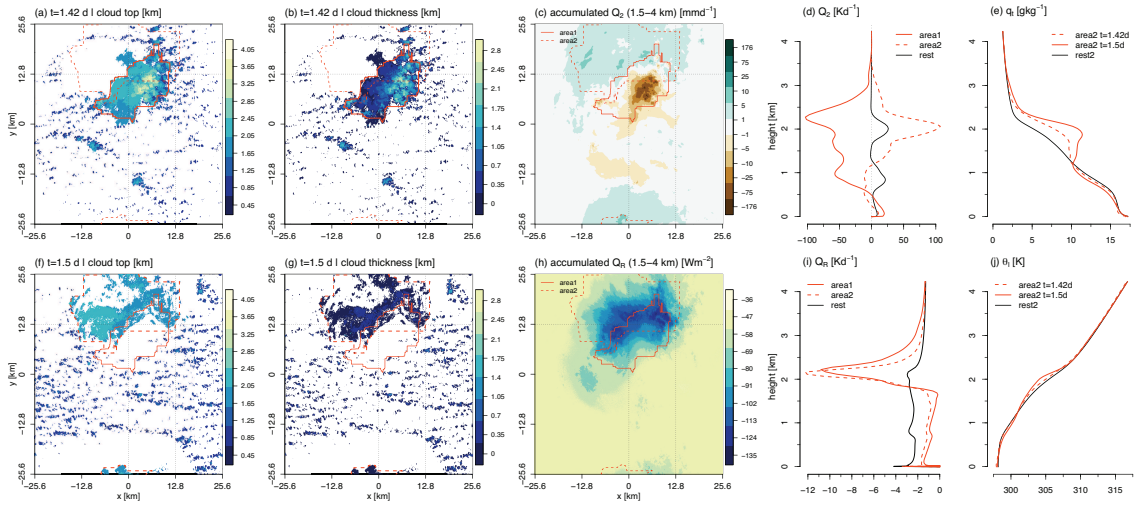

Figure 3.6.: Horizontal cross-sections and vertical profiles of various quantities for the *CTL* simulation. (a, f) cloud top height and (b, g) cloud thickness at time t=1.42 d (a, b) and at time t=1.5 d (f, g). (c) accumulated moisture source Q_2 and (h) accumulated radiative tendency Q_R between t=1.42 d and t=1.5 d, integrated from 1.5 km to 4 km. The contours show the location of the deep cluster at t=1.42 d ('area1', solid, connecting points where the cloud top height is larger than 2 km), and the location of the mature outflow at t=1.5 d ('area2', dashed, connecting points where the cloud base height is larger than 1.7 km). Vertical profiles of (d) accumulated moisture source Q_2 and (i) accumulated radiative tendency Q_R conditioned on area1, area2, and the average of the rest of the domain. And vertical profiles of (e) total humidity and (j) liquid water potential temperature conditioned on area2, showing both the profile at t=1.42 d (dashed) and at t=1.5 d (solid), and the temporal average for rest2.

events, cloudiness can thus be enhanced when shallow convection organizes and deepens. But such a positive relationship does not carry over to longer time scales. Once the cloud layer deepens beyond about 2.5 km, and the sustained presence of deeper convection diminishes the inversion structure, the stratiform layers do not develop anymore, as evident in the *DRY* simulation after about 2 d (Fig. 3.5 b *right*). It is not obvious why outflow layers cease to develop once the cloud field is deeper than 2.5 km, and their absence might be partly related to insufficient vertical resolution (the vertical grid is uniformly stretched by 1.02 with height, such that Δz increases from about 45 m at 1.75 km to 70 m at 3 km). Another possibility is that the stronger surface forcing in the *DRY* case promotes stronger updrafts that are more effective in disturbing the inversion. As a last remark, the evidence that the outflow layers always spread over cold-pools might have important radiative and dynamical implications to how cold-pool dynamics work, as for example the radiative cooling rate inside the cold-pool strongly reduces underneath the outflow layers (Fig. 3.6 i).

Table 3.2.: Averages of the surface buoyancy flux, the mean inversion depth z_{inv}, the cloud layer depth $z_{RH<0.3}$, maximum cloud top height, cloud cover, maximum cloud-base cloud fraction, the corresponding cloud core fraction (cloud core is defined as having nonzero liquid water and being positively buoyant compared to the slab-average), liquid water path, albedo (using the computation of *Zhang et al.* (2005)), and rain water path for all the simulations.

case name	SBF [10^{-4} m^2s^{-3}]	z_{inv} [m]	$z_{RH<0.3}$ [m]	CTH_{max} [m]	CC [%]	CF_{max} [%]	CoF_{max} [%]	PW [kgm^{-2}]	LWP [gm^{-2}]	α [%]	RWP [gm^{-2}]
CTL.2K.ω6	5.87	1511	3092	7082	9.4	3.2	2.0	42.2	11.06	5.22	28.2
CTL	4.80	1777	1885	3032	11.2	3.4	2.1	30.0	8.53	5.81	4.7
DRY	5.84	1814	2485	3818	9.3	3.2	1.9	29.4	9.95	5.18	12.3
CTL.unirad	5.51	1512	2193	5279	9.3	3.2	2.0	32.6	8.83	5.0	12.6
DRY.unirad	6.60	1620	2418	5850	9.1	3.4	2.2	30.7	10.23	4.90	17.4
DRY.cool	7.53	1617	2506	4398	10.7	3.7	2.1	29.5	12.6	6.06	42.8
DRY.u15	4.70	1454	2199	3711	9.9	3.0	1.9	30.8	10.14	5.58	13.3
DRY.ω8.5	5.74	1880	2254	3191	9.1	3.2	1.9	27.2	8.22	4.93	8.3
DRY.u15.ω8.5	4.70	1417	1973	3032	10.2	3.1	1.9	29.1	9.13	5.65	7.5
CTL.u15	4.10	1811	1942	2499	11.4	3.0	1.8	31.2	10.1	6.29	7.9
CTL.2K	5.43	1964	2269	2991	9.9	3.4	2.1	34.9	8.7	5.33	7.6
DRY.wtg	6.69	1721	3120	8056	9.8	3.3	2.0	35.1	15.9	6.01	55.1
DRY.wtg.rlx	6.94	1931	2864	7325	8.6	3.2	2.0	31.0	12.7	5.04	33.8

Table 3.3.: (Continued from Table 3.2) Averages of the integrated moistening tendencies LHF, subsidence drying, precipitation drying, and residual moistening tendency $d/dt\ q_t$. The heat budget is integrated up to 6 km, the variables shown are radiative tendency, SHF, subsidence warming, and residual warming tendency $d/dt\ \theta_l$. Note that 29 $W\,m^{-2} \approx 1\ mm\,d^{-1}$.

case name	LHF [Wm^{-2}]	sub q_t [Wm^{-2}]	R [Wm^{-2}]	$d/dt\ q_t$ [Wm^{-2}]	Q_R [Wm^{-2}]	SHF [Wm^{-2}]	sub θ_l [Wm^{-2}]	$d/dt\ \theta_l$ [Wm^{-2}]
CTL.2K.ω6	245.3	-205.0	-45.7 ± 42.0	-5.4	-129.3	3.2	120.0	38.3
CTL	205.1	-227.5	-11.1 ± 13.0	-33.5	-139.5	1.3	170.3	44.0
DRY	238.1	-224.9	-25.9 ± 29.1	-12.8	-167.1	2.5	168.5	32.2
CTL.unirad	227.1	-219.2	-22.2 ± 38.9	-14.3	-161.6	2.3	145.7	8.8
DRY.unirad	261.7	-220.7	-29.4 ± 46.2	11.6	-161.6	3.2	143.9	17.7
DRY.cool	258.9	-220.4	-42.8 ± 36.3	-4.4	-165.4	6.7	165.0	4.5
DRY.u15	257.8	-238.7	-33.6 ± 49.1	-14.5	-175.4	-3.0	168.9	26.6
DRY.ω8.5	236.5	-252.9	-19.5 ± 26.3	-35.8	-174.0	2.2	199.0	48.4
DRY.u15.ω8.5	263.6	-268.3	-20.6 ± 33.6	-25.3	-177.0	-3.5	195.3	36.7
CTL.u15	231	-239.0	-21.1 ± 26.8	-29.1	-145.2	-3.1	170.0	43.9
CTL.2K	238.3	-259.2	-17.9 ± 18.9	-38.8	-151.8	1.1	163.9	32.4
DRY.wtg	242.8	-77.0	-86.4 ± 91.1	79.2	-131.3	6.9	46.8	7.1
DRY.wtg.rlx	264.8	-172.2	-51.8 ± 57.4	-39.8	-153.4	5.2	96.8	3.2

3.4.2. Enhanced precipitation and cloudiness in response to stronger surface forcing

Across most of the simulations in Table 3.1, cloud cover tends to decrease when precipitation increases and clouds deepen (Fig. 3.2 a). The exception are the simulations where the surface fluxes are more strongly forced, either via cold-air advection (*DRY.cool*) or via a wind speed increase (*DRY.u15* and *CTL.u15*). Here we discuss how the stronger surface forcing in these simulations influences cloudiness and precipitation.

The $-0.75\,\mathrm{K\,d^{-1}}$ horizontal advective cooling in *DRY.cool* enhances both the LHF by about $20\,\mathrm{Wm^{-2}}$ (a relative increase of 9 %) and the SHF by $4\,\mathrm{Wm^{-2}}$ (a relative increase of 168 %), which leads to a 30 % increase of the surface buoyancy flux compared to *DRY* (see Table 3.3). This stronger surface forcing in *DRY.cool* promotes the deepening of shallow convection, enhances the mass flux, and increases the surface precipitation rate by 65% to $43\,\mathrm{Wm^{-2}}$ (dark blue lines in Fig. 3.7). Even though the domain-averaged RH below 2 km has not changed much, cloud fractions between cloud base up to 2 km in *DRY.cool* have increased considerably compared to DRY (in light-orange). The enhanced cloud fractions stem from larger and deeper clusters developing due to the strong surface fluxes (not shown). These larger cloud clusters help build up RH locally, which is also manifest in the larger moisture variance (Fig. 3.7 f). The enhanced cloudiness in the lower cloud layer, along with the additional deeper cloud above 3 km, results in a relative increase of projected cloud cover by 15 % (Table 3.2).

Rather than promoting the surface fluxes by cooling and destabilizing the layer, we can force stronger fluxes mechanically by a sudden perturbation in the surface wind speed, such as done in *Nuijens and Stevens* (2012). The timeseries in Fig. 3.8 shows that a $5\,\mathrm{m\,s^{-1}}$ increase of the geostrophic zonal wind in *DRY.u15* instantaneously increases the LHF by about 60 % compared to *DRY*, a much larger increase than in the *DRY.cool* case. The initially enhanced surface buoyancy flux in *DRY.u15* after the wind speed increase leads to the development of 6 km deep congestus clouds and large precipitation rates in the first 12 h after the perturbation (Fig. 3.8 d, e). But rather than maintaining a large LHF due to enhanced deepening and drying, the LHF in *DRY.u15* gradually lowers due to sub-cloud layer moistening, eventually being only 8% larger than in the *DRY* case. Combined with a SHF that becomes negative due to sub-cloud layer warming (as found in *Nuijens and Stevens* (2012)), the surface buoyancy flux becomes low enough to eventually collapse congestus to shallow convection at day 3.75. After a subsequent 12 h period of shallow non-precipitating convection, congestus eventually re-appears, along with a boost in the sensible and thus also surface buoyancy flux due to evaporating precipitation (Fig. 3.8 b, c, e).

A separate inspection of the shallow non-precipitating and the deeper congestus regime in *DRY.u15*, distinguished by compositing on periods with the lowest (dashed) and high-

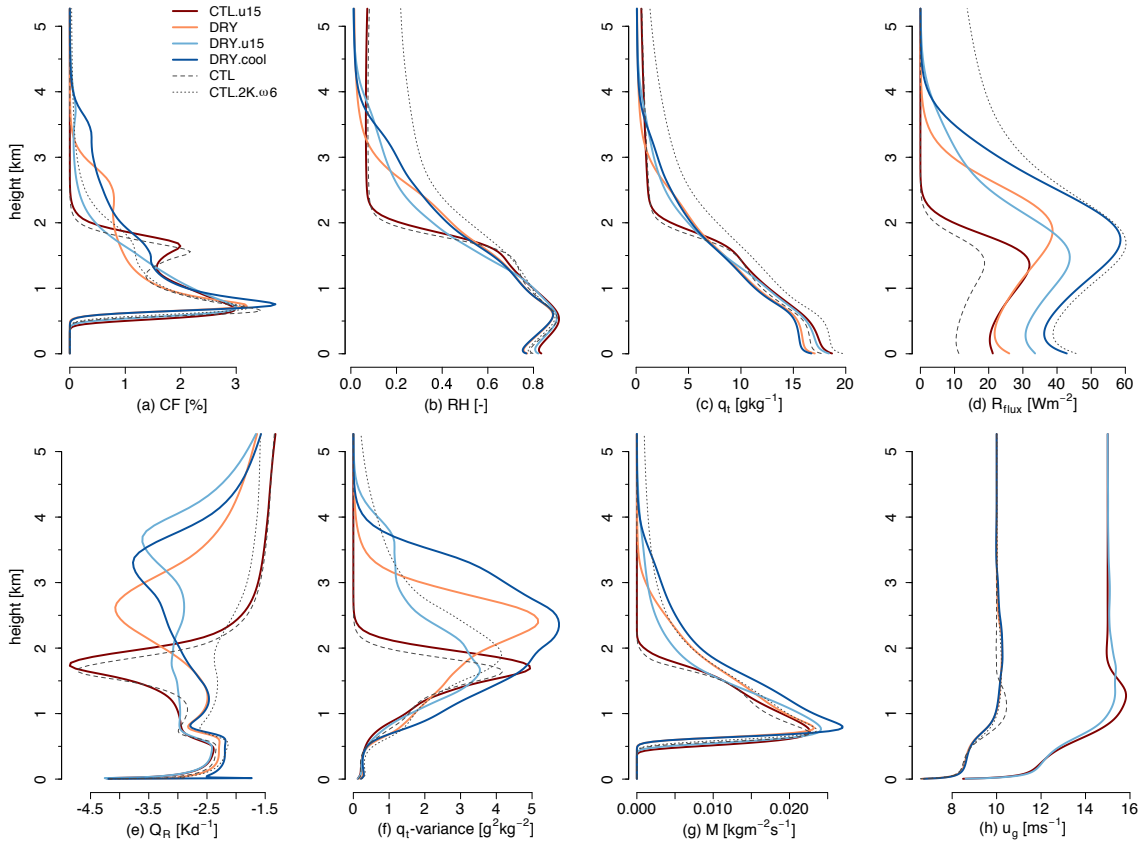

Figure 3.7.: Domain-averaged profiles of (a) cloud fraction, (b) RH, (c) total humidity, (d) precipitation flux, (e) radiative heating, (f) variance of total humidity, (g) convective massflux, and (h) geostrophic zonal wind for the *CTL.u15*, *DRY*, *DRY.u15*, and *DRY.cool* simulation. The thin dashed and dotted lines represent the winter-like *CTL* and the summer-like *CTL.2K.ω6* simulation, respectively.

est (solid) quartile of surface precipitation (Fig. 3.9), reveals that during periods with more precipitation, deeper convection detrains its moisture in the free troposphere, while the cloud layer below 1.75 km experiences a drying due to precipitation, mixing and compensating subsidence from the deeper convection. The gradual drying of the cloud layer eventually leads to the collapse of congestus, because it becomes increasingly difficult for updrafts to maintain sufficient buoyancy in the drier cloud layer. During periods with non-precipitating shallow convection (dashed blue lines in Fig. 3.9), the layer near and above cloud base experiences strong moistening (3.9 b), and cloud fractions above cloud base increase (3.9 a). The difference between the shallow and the congestus regime is also evident in the horizontal structure of the cloud field, which is organized into cloud streets during periods of non-precipitating shallow convection, compared to arc-like structures reminiscent of cold pools during the deeper congestus phases (not shown).

In *DRY.u15*, the domain and time-average cloud fraction profile in near-equilibrium shows a more linear decrease with height, compared to the exponential decrease which most

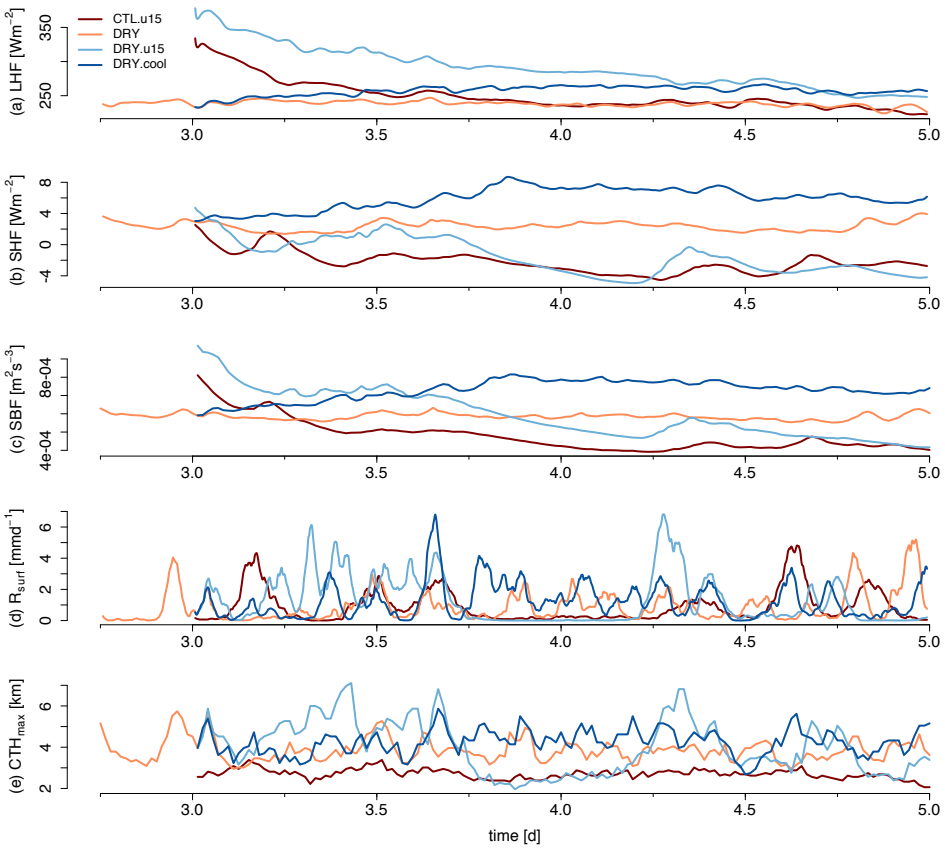

Figure 3.8.: Domain-averaged timeseries of (a) LHF, (b) SHF, (c) surface buoyancy flux, (d) surface precipitation rate, and (e) maximum cloud top height for the *CTL.u15*, the *DRY*, the *DRY.u15*, and the *DRY.cool* simulations.

other simulations show (Fig. 3.7 a). Besides the higher RH at those levels, the presence of larger wind shear across cloud base might play a role at promoting cloudiness (Fig. 3.7 h), by horizontally spreading out cloud layers as they form near the lifting condensation level. The enhanced cloud fraction between about 1–1.8 km increases projected cloud cover compared to other simulations with comparable precipitation rates (see Fig. 3.2 a).

The same 5 m s^{-1} wind speed increase in the moister *CTL.u15* simulation leads to similar changes in the surface fluxes (Fig. 3.8 a–c), ending up with just a 13 % increase of the LHF, the development of a negative SHF, and a 15% lower surface buoyancy flux compared to *CTL* (Table 3.2, 3.3). The increase in the LHF is still enough to double the average precipitation rate (Table 3.3). Similar to the *DRY.u15* case, the RH in the lowest 1.5 km is enhanced and the domain-averaged cloud fraction profile above cloud base more linear, presumably along with the greater wind shear. But unlike in the *DRY.u15* case, clouds deeper than 3 km hardly develop in *CTL.u15* (Fig. 3.7 a). Similar to what we described in Section 3.4.1, the LHF is smaller in the case of a moister free troposphere, and the smaller integrated radiative cooling rates leads to shallower convection overall,

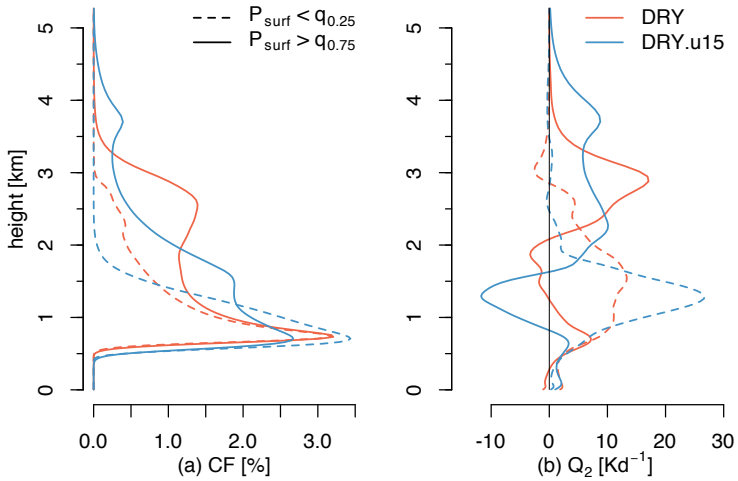

Figure 3.9.: Domain-averaged profiles of cloud fraction (a) and moisture source Q_2 (b) composited on the lowest ($<q_{0.25}$, dashed) and highest ($>q_{0.75}$, solid) quartile of the surface precipitation rate. Shown are the *DRY* case in red and the *DRY.u15* case in blue. The mean surface precipitation rate for the lowest and highest quartile respectively are: 3.9 W m^{-2} vs. 62.8 W m^{-2} for *DRY*, 0.3 W m^{-2} vs. 102.4 W m^{-2} for *DRY.u15*.

which remains capped by a relatively strong inversion.

3.4.3. Larger subsidence can limit precipitation, but not necessarily the depth of the moist layer

As discussed in Section 3.4.1, simulations with a drier initial free troposphere tend to precipitate more, but in those simulations we considered only a perturbation in absolute humidity in the free troposphere. In nature, drier layers are likely created by changes in vertical or horizontal advection. How does an increase in subsidence, which dries layers in the presence of a vertical humidity gradient, influence cloudiness and the precipitation rate?

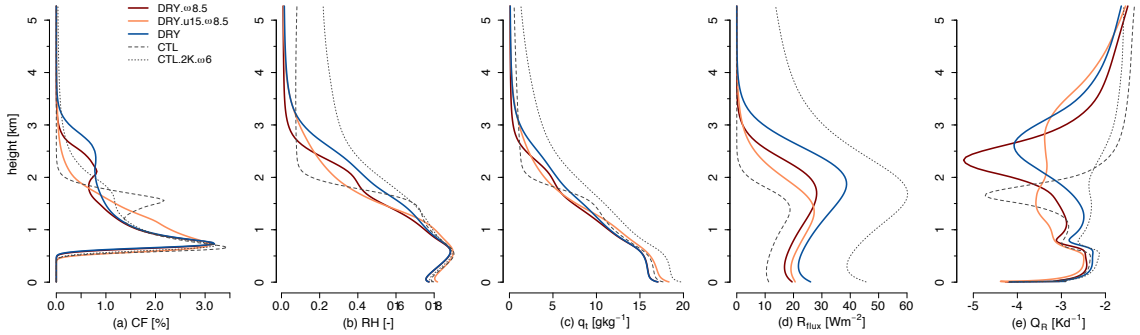

Figure 3.10.: Domain-averaged profiles of (a) cloud fraction, (b) RH, (c) total humidity, (d) precipitation flux, and (e) radiative heating for the *DRY.ω8.5*, the *DRY.u15.ω8.5*, and the *DRY* simulation. The thin dashed and dotted lines again represent the winter-like *CTL* and the summer-like *CTL.2K.ω6* simulation.

Fig. 3.10 shows that increasing the base subsidence rate ω_0 from 7.5 to 8.5 mm s^{-1} in the *DRY.ω8.5* simulation (solid red line) leads to a decrease in precipitation and a shallowing of the cloud layer of about 250 m compared to *DRY* (solid blue line). The integrated heat and moisture budget terms in Table 3.3 show an increase in subsidence drying by 12% and an increase in subsidence warming by 18%. Because the prescribed subsidence rate decreases exponentially towards the surface, and absolute humidity gradients in the sub-cloud layer are small, the additional drying is concentrated in the cloud layer (Fig. 3.10 b). A shallower trade-wind layer requires less surface moisture input to maintain a given moisture profile. Hence, although the layer is drier, the LHF does not increase. The *DRY.ω8.5* case has both the lowest liquid water path and the lowest integrated moisture content of all the simulations discussed (Fig. 3.2 b, c), but because convection is deeper than in the *CTL* case, its surface precipitation rate is still larger than in the winter-like *CTL* case.

Subsidence is effective at creating structure in the lower atmosphere by increasing existing gradients in humidity and temperature, in contrast to convection, which tends to smooth gradients when deepening (see also Fig. 3.1). The RH profile of the *DRY.ω8.5* simulation shows more pronounced gradients in the cloud layer, at about 1.5 km and 2.5 km, than the *DRY* simulation. Along with the stronger gradient especially near 2.5 km, and due to larger cloudiness at this level, the radiative cooling peak the top of the cloud layer is enhanced by about 1 K d^{-1} compared to *DRY*. Although there is a slightly larger tendency to form layers with enhanced cloudiness near cumulus tops at about 2.2 km, the total cloud cover of *DRY.ω8.5* is even lower than in *DRY* (9.1% compared to 9.3%), with both being on the low side of cloud covers (Fig. 3.2 a). When the zonal wind speed is uniformly increased by 5 m s^{-1} in addition to strengthening the subsidence rate (*DRY.u15.ω8.5*)—as one might expect from a strengthening of the large-scale overturning circulation—cloud cover increases by 12% relative to *DRY.ω8.5* due to the effect of the different surface forcing explained in the previous section. But the increased subsidence in *DRY.u15.ω8.5* keeps its effect on reducing precipitation and slightly shallowing the moist layer compared to *DRY.u15* (see Table 3.2 and 3.3).

As shallow convection deepens to congestus and precipitation contributes more to the heating of the free troposphere, subsidence should decrease. Further, the simulations which use interactive radiation but have a prescribed subsidence profile develop a free-tropospheric heating surplus (see e.g. Fig. 3.3 f), unless an additional horizontal cooling tendency is prescribed (in the *DRY.cool* case). If subsidence is computed interactively to fulfill WTG balance in the *DRY.WTG* simulation, the realized subsidence rate is much smaller than what is prescribed in *DRY* (Fig. 3.11 e). The heating and drying tendencies from subsidence are therefore smaller (yellow lines in Fig. 3.11 a-d), and the precipitation tendency contributes most to the heating and drying of the free troposphere. The

cloud layer in the *DRY.wtg* case has a higher RH than in the *DRY* case, and cloud fractions between 1 and 2 km increase. Together with the additional deeper cloud in the free troposphere, this contributes to a modest 5% relative increase of projected cloud cover (Table 3.2). Despite the reduced subsidence and the moister cloud layer, the inversion depth reduces by about 100 m compared to *DRY* (see Table 3.2).

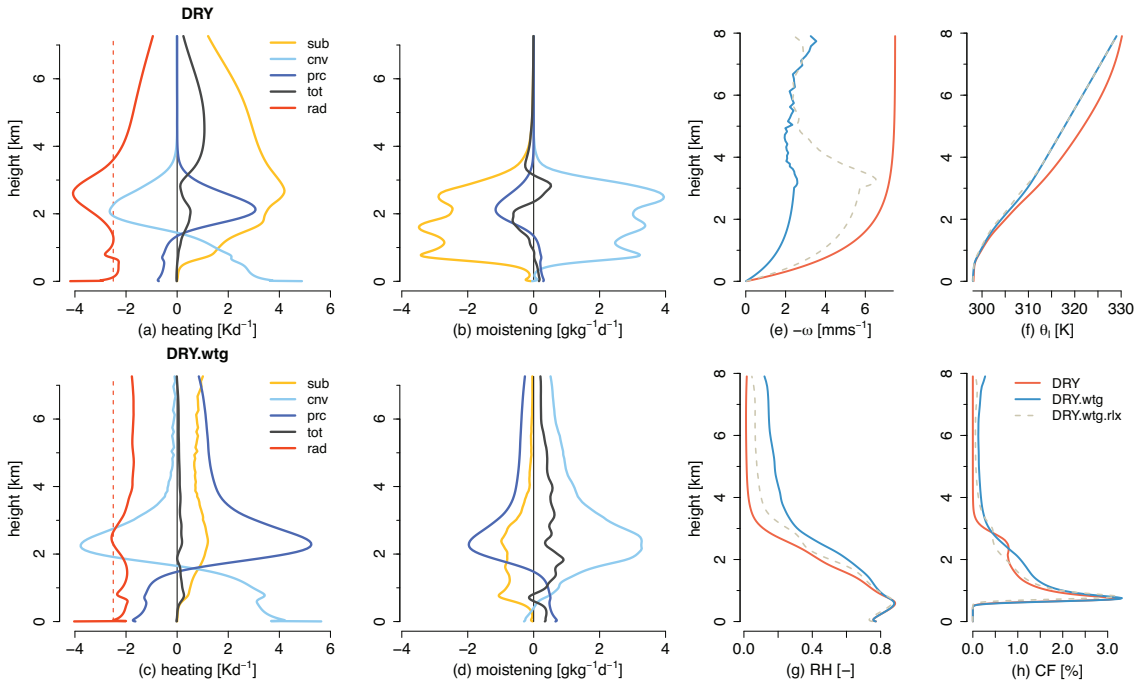

Figure 3.11.: Domain-averaged vertical profiles of the heating and moistening tendencies for the *DRY* (a, b) and *DRY.wtg* simulation (c, d); and profiles of (e) large-scale subsidence rate, (f) liquid water potential temperature, (g) RH, and (h) cloud fraction for the *DRY*, the *DRY.wtg* and the *DRY.wtg.rlx* case.

While the heat budget is nicely balanced in the *DRY.wtg* simulation, the strong convective moistening—in the absence of strong subsidence drying—leads to a pronounced residual moistening tendency (see solid black lines in Fig. 3.11 c, d). Fig. 3.11 c also shows that the radiative cooling tendency below about 4 km reduces because of the moister free troposphere. When a height-dependent relaxation of the domain-averaged humidity profile to its initial profile is applied (*DRY.wtg.rlx*), the integrated residual moistening tendency reduces (Table 3.3). But the humidity relaxation gives rise to new issues regarding the interpolation of the subsidence profile in the lowest 3 km (dashed gray lines in Fig. 3.11 e, g). Overall, the WTG simulations show that a domain size of $51.2\times51.2\times10\,\mathrm{km}^3$ is likely too small to robustly represent the interactions of shallow convection with deep convection.

3.5. Conclusions

In the introduction we sketched how recent observations made at Barbados have highlighted changes in the cloud fraction profile and the precipitation rate that occur between the different seasons. Namely, the winter regime has larger low-level cloudiness than the summer regime because of enhanced cloudiness near the inversion, but the summer regime has overall more precipitation and deeper convection. Here we focus on three factors influencing the seasonal cycle of cloudiness and precipitation at Barbados: (1) free-tropospheric humidity and its interaction with radiation, (2) surface forcing, and (3) large-scale subsidence. For the moisture-radiation interactions, we focus on differences in prescribed and interactive radiation under the presence of different initial free-tropospheric water vapor contents. For the surface forcing, we study the effect of adding horizontal advective cooling and increasing wind speed. And for the large-scale subsidence, we study the influence of stronger prescribed subsidence and explore the impact of interactively computing subsidence to fulfill the weak temperature gradient balance.

Our large-eddy simulations (LES) highlight two mechanisms that help increase cloud cover during winter. First, cloud cover increases when stratiform outflow layers form at the top of the cloud layer. Such locally detrained layers of outflow are observed regularly at Barbados, and their more frequent occurrence in winter contributes to the enhanced low-level cloudiness of this season (*Nuijens et al.*, 2014). The thin stratiform layers are triggered by condensate-detrainment from larger and deeper cloud clusters and spread over the cold-pool initiated by the cluster. The formation of outflow is associated with strong drying above the cloud layer, which is concentrated in the region of the deepest turrets, and which arises due to precipitation and compensating subsidence. Our simulations suggest that the deeper clusters themselves help strengthen the inversion, which caps subsequent moisture transport into the cloud layer and promotes the outflow. Outflow layers do not develop when radiation is prescribed and uniform. The interaction of radiation with cloud and moisture gradients is crucial because dry downdrafts are promoted when overshooting updrafts experience strong radiative cooling. And strong cloud-radiative cooling across the inversion promotes saturation and helps maintain the outflow layers once the supply of moisture from the sub-cloud layer stops. That convection itself might be largely responsible for locally strengthening the inversion would help explain why variations in measures of the inversion strength, such as lower tropospheric stability (*Klein and Hartmann*, 1993), do not well explain variations in cloudiness near cloud tops (*Nuijens et al.*, 2015a).

For the second mechanism, cloud cover increases when cloud fractions increase throughout the lower cloud layer. This occurs in simulations with stronger wind or additional advective cooling, in which intermittent periods and confined regions of larger relative humidity increase cloud fractions between about 1 and 2 km. Furthermore, stronger wind shear in the lowest 1000 m slightly increases cloud cover in the higher wind speed cases.

Observations also suggest that stronger wind and air masses advecting colder and drier air promote cloudiness at those levels (*Klein*, 1997; *Brueck et al.*, 2015; *Nuijens et al.*, 2015a).

The different simulations overall underestimate cloud cover compared to observations, and simulated cloud fraction profiles show a more exponential decrease of cloud fraction above cloud base than in nature (*Nuijens et al.*, 2014). One reason for these differences is numerical diffusion (*Matheou et al.*, 2011), which limits the lifetime of small cloud patches. Another reason is a certain lack of variability in cloud top heights compared to nature due to missing stratification associated with differential advection, even though mesoscale circulations related to deeper and organized cloud clusters develop on the relatively large $51.2\times51.2\times10\,\mathrm{km}^3$ domain used. Similar to Barbados, where cloud fractions near cloud base are relatively invariant over longer timescales (*Nuijens et al.*, 2014; 2015a;b), the near-base cloud fractions vary only little across the different simulations (3–3.7%). Also the near-base cloud core fractions show little variability (1.8–2.2%).

As soon as the cloud layer deepens beyond about 2.5 km, the inversion structure diminishes. A weaker inversion reduces longwave cooling at the top of the cloud layer, which discourages the development of stratiform outflow layers near 2 km and decreases cloud cover. Even if stratiform layers may form when the cloud layer gets deeper than 2.5 km, for example when large-scale subsidence is increased, the stratiform layers tend to have lower cloud fractions than if they had formed at lower altitudes, because moisture gradients are smaller at higher altitudes. This is similar to findings based on observations from the Barbados Cloud Observatory (*Lamer et al.*, 2015). But insufficient vertical resolution due to the stretched vertical grid might also explain why the development of outflow layers is discouraged once the cloud layer deepens beyond 2.5 km in the LES. The hypothesis that strong inversions are difficult to be maintained in the presence of precipitation and deeper and organized clusters is worth being tested with measurements.

Similar to observations (e.g *Kubar et al.*, 2009), the depth of convection is a good predictor of precipitation in our simulations. The strongest deepening and the largest precipitation rates develop under weaker subsidence and larger sea surface temperatures, and resemble the shift from the winter to the summer trades. But moderate deepening of the cloud layer and increases in precipitation also take place under much stronger winds, under cold-air advection, and under drier free tropospheres. These three perturbations strengthen the surface fluxes and are typically associated with the winter regime, demonstrating that even small changes in large-scale forcings during winter can introduce considerable variability in cloudiness and precipitation (*Brueck et al.*, 2015; *Nuijens et al.*, 2015a). That a drier free-troposphere promotes the deepening of shallow convection by enhancing surface evaporation and increasing the net radiative cooling of the trade-wind layer was also found by *Betts and Ridgeway* (1989) based on a one-dimensional thermodynamic model.

The average surface precipitation rate across the different simulations does not increase much beyond $1.5\,\mathrm{mm\,d^{-1}}$ as shallow convection deepens to congestus. The simulations tend to underestimate precipitation compared to observations at Barbados, which is in part related to the residual drying and warming tendencies present in many of the simulations due to the relatively strong prescribed subsidence. Simulated precipitation flux profiles are also sensitive to the microphysics scheme used (*Stevens and Seifert*, 2008; *VanZanten et al.*, 2011; *Li et al.*, 2015). Still, we may postulate a few mechanisms that could hint at why increases in precipitation might be limited. First, precipitation removes liquid water near cumulus tops, which limits the amount of entrainment drying and the depth of the cloud layer (e.g *Albrecht*, 1993; *Stevens and Seifert*, 2008; *Bretherton et al.*, 2013). Second, precipitation often evaporates below cloud base (e.g *VanZanten et al.*, 2011). Both mechanisms can limit the surface moisture flux and thus the amount of liquid available for precipitation. Third, with a deepening of the moist layer, the amount of radiative cooling experienced by the sub-cloud and lower cloud layer decreases. This would negatively influence the surface heat and moisture fluxes, reducing the tendency to deepen and precipitate. The only simulation supporting a large surface precipitation rate of about $3\,\mathrm{mm\,d^{-1}}$ is when large-scale subsidence is computed interactively to fulfill the weak temperature gradient (WTG) approximation. In this WTG simulation, the realized subsidence rate is much smaller than what is prescribed in the other simulations, because convection deepens rapidly and precipitation and its heating tendency become large.

The WTG simulations are a step towards exploring precipitating shallow convection in a regime where the vertical development is no longer strongly constrained by the setup. But they have their own limitations, because they would require an even larger domain size and a more realistic representation of large-scale advection to achieve balanced tendencies. Nevertheless, together with the other simulations presented here, they demonstrate that the organization and deepening of shallow convection and its interaction with radiation are an important control on precipitation, cloudiness and the trade-wind layer structure. However, convection only organizes and deepens on domains of about $50\times50\,\mathrm{km^2}$ or larger (*Seifert and Heus*, 2013), showing that cloud responses to climate change simulated with LES on much smaller domains (e.g *Rieck et al.*, 2012; *Blossey et al.*, 2013; *Tan et al.*, 2016) might miss important properties of convection. The upcoming field campaign 'EUREC^{4}A' (*Bony et al.*, 2017) will provide specific measurements to test whether the physical mechanisms at play in the rather idealized simulations presented here are adequate descriptions of the interactions of shallow convection and the large-scale flow.

Chapter 4

Statistics of spatial organization as identified by cold pools

4.1. Introduction

Cold pools associated with evaporating precipitation influence the organization and deepening of shallow convection. In the large-eddy simulations (LES) presented in the previous chapters of this thesis, the dynamic and thermodynamic perturbations associated with cold pools organized the shallow convection into larger and deeper cloud clusters with substantial precipitation, surrounded by dry regions with non-precipitating shallow convection. While the organized clusters mix moisture over a deep layer, compensating subsidence dries the lower cloud layer in the vicinity. In the mean, the simulated organization therefore smooths the vertical humidity profile and diminishes the inversion strength. Although cloud clusters locally enhance cloud cover, the presence of deeper and organized convection decreases domain-averaged and time-averaged cloudiness in the LES, as was also found by *Seifert and Heus* (2013). The organization of shallow convection on the mesoscale might therefore strongly affect the albedo in the trade-wind region, a region known to account for much of the uncertainty in climate sensitivity estimates (e.g *Bony and Dufresne*, 2005; *Vial et al.*, 2013). Lacking insight from observations makes relationships between cloudiness and shallow convective organization an important outstanding question (*Zuidema and Torri*, 2017).

There are different ways to detect periods of deeper and presumably organized convection in the trades using observations. The most straightforward indicator is the cloud-top

height. Other indicators are precipitation, which scales with the depth of shallow cumuli (e.g. *Kubar et al.*, 2009; *Nuijens et al.*, 2009), or the horizontal clustering of clouds, which can be analyzed with satellite data (as done by *Lonitz et al.* (2014) for trade-wind clouds and by *Tobin et al.* (2012) for deep convection). But deeper and organized trade-wind convection can also be identified by its surface manifestation—the occurrence of cold pools. When relying on measurements taken at a single site, the occurrence of cold pools is probably the most reliable way to identify periods of deeper and organized convection because the deeper precipitating clouds do not need to overpass the site directly for a period to be identified as organized.

Convective cold pools are triggered by the evaporation of precipitation into unsaturated downdrafts, spreading out at the surface as a density current. The passage of a cold-pool front manifests itself in an abrupt drop in surface temperature, and is often accompanied by a humidity drop and a wind speed increase associated with the gust front. In the wake of a cold-pool front, the mixed layer recovers back to its pre-front properties. Most studies addressing oceanic cold pools in the past focused on deep convection (e.g *Barnes and Garstang*, 1982; *Young et al.*, 1995; *de Szoeke et al.*, 2017). A number of those studies focused on the thermodynamic structure of the sub-cloud mixed layer, and how different processes such as clear-air entrainment from above and surface fluxes govern the cold-pool recovery process (*Barnes and Garstang*, 1982; *de Szoeke et al.*, 2017).

In the trades, detailed case studies for two weeks of the RICO campaign have advanced our understanding of cold pools from shallow convection (*Zuidema et al.*, 2012). They showed that the deepest clouds and strongest radar signals occurred in the moistest tercile of water vapor paths, and that precipitation-driven downdrafts can introduce additional gradients in the thermodynamic structure. However, the short time period and the sparse sampling of the vertical structure with radiosondes did not allow to draw conclusions about the statistics of shallow-convective organization in the trades.

Here we use ground-based in-situ and remote-sensing data at Barbados to explore the statistics of shallow-convective organization as identified by cold pools. We address the following research questions: How frequently do we observe cold pools at Barbados? And with what changes in the surface meteorology and in the vertical cloud and humidity structure are they associated? We use data from two surface stations located about 400 m apart on eastward promontories of Barbados. Whereas the Ragged Point station is characterized by its nearly 10-year long timeseries of surface weather data, the 6-year timeseries from the Barbados Cloud Observatory (BCO) at Deebles Point also includes coincident remote sensing of cloudiness, precipitation and the vertical humidity structure.

The numerical simulations performed in the previous chapters of this thesis motivate the use of observations to test the hypotheses regarding the strong influence of organized and deeper shallow convection on the thermodynamic and cloud structure in the trades. This

is a challenging task because it involves processes acting on many spatial and temporal scales that are hard to separate. Hence, in this chapter we focus on the instantaneous effect of the organized convection by relating changes in cloud properties and the vertical humidity structure to the onset of cold pools. This strategy limits the potential impact of other factors that might influence cloudiness and the trade-wind layer structure.

The next section presents the data sources and explains the cold-pool detection algorithm. In Section 4.3, we discuss two example days with intense cold-pool activity. Besides presenting general statistics of the structure and variability of detected cold pools, Section 4.4 shows how surface properties, cloudiness and the vertical humidity structure change with respect to the cold-pool onset.

4.2. Data and Methods

4.2.1. Data sources

Most of data used in this study is collected at the BCO (*Stevens et al.*, 2016). The BCO is operated by the Max Planck Institute for Meteorology together with the Caribbean Institute for Meteorology and Hydrology since April 2010 at Deebles Point. Deebles Point is located atop a cliff 17 m a.s.l. at the eastern most tip of Barbados (13.15°N, 59.4°W) and samples nearly undisturbed Atlantic trade-wind conditions. The longer cold-pool timeseries used in Section 4.4.1 is derived from weather data collected at Ragged Point, approximately 400 m to the northwest of Deebles Point. The individual instruments and the variables derived are described in more detail in the following subsections. Fig. 4.1 displays the time periods for which data from the different instruments are used.

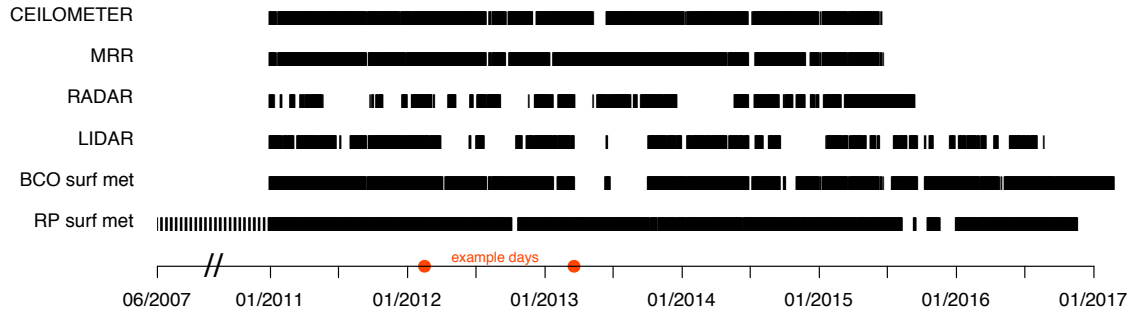

Figure 4.1.: Time periods used for the different instruments. The red dots show the example days discussed in Section 4.3.

4.2.1.1. Surface meteorology data

The University of Miami operates a measurement station mounted on a 17 m tower (atop a 30 m cliff) at Ragged Point (RP). The tower was erected in 1989 to collect aerosol

measurements (see e.g. *Prospero and Lamb* (2003)). The station measures temperature, relative humidity, barometric pressure, wind speed, wind direction, and rain occurrence at 1-min resolution with a weather sensor from the company 'R.M. Young', with the control system and software package developed by the University of Miami. We use RP data from mid-June 2007 until November 2016.

At the BCO, a Vaisala WXT520 sensor mounted on a 5 m mast measures temperature, relative humidity, pressure, rain, wind speed and wind direction. The original 10-s resolution is averaged to 1-minute resolution. Measurements with a data quality less than 100 % (variable 'SDQ') are discarded. We use BCO surface data from January 2011 to February 2017.

For both sites, we discard temperature measurements exceeding 35°C and pressure measurements lower than 980 hPa. Specific humidities are computed from temperature and relative humidity. A mean offset exists between the timeseries at the BCO and RP, with temperature at the BCO being 1.6°C warmer, specific humidity 2.0 $\mathrm{g\,kg^{-1}}$ larger, pressure 1.7 hPa higher and wind speed 2.2 $\mathrm{m\,s^{-1}}$ lower. The offset mainly results from the height difference of about 25 m. The examples in Fig. 4.3 and Fig. 4.4 demonstrate how closely the temperature, humidity and wind speed timeseries match.

4.2.1.2. KATRIN cloud radar

The hydrometeor fraction is derived from the 36 GHz Doppler radar 'KATRIN'. The KATRIN radar has a temporal resolution of 10 s and a vertical resolution of 30 m. We use data for the period of January 2011 to Mid-September 2015, during which the radar operated in vertically-pointing mode.

We mask returns with equivalent radar reflectivity $\mathrm{Z_e}$ below −45 dBZ (a 5 dBZ lower threshold than used in *Nuijens et al.* (2014)). We derive the maximum cloud top height $\mathrm{CTH_{max}}$ as the uppermost range gate with cloudy echo below 5 km. The cut-off height of 5 km assures to capture deeper convective clouds while excluding cirrus clouds.

4.2.1.3. Ceilometer

The first-detected cloud-base height (cbh1) is derived from a Jenoptik 15-K laser ceilometer operating at 1064 nm. The ceilometer has a temporal resolution of 30 s and a vertical resolution of 15 m. Ceilometer data is used up to a height of 5 km for the period of January 2011 to June 2015.

We use cbh1 to derive cloud cover estimates. As in *Nuijens et al.* (2014; 2015a;b), we distinguish contributions to cloud cover from clouds with bases near the lifting-condensation level (cbh1 $<$ 1 km, referred to as $\mathrm{CC_{LCL}}$) and from clouds with bases further aloft (cbh1 $>$ 1 km, $\mathrm{CC_{ALOFT}}$). During periods of strong rain, the ceilometer cannot detect a cbh1. To not confuse these periods with clear-sky, we exclude data when the MRR detects rain

but no cbh1 is detected.

4.2.1.4. Raman lidar

The vertical humidity structure is retrieved with a multichannel Raman lidar. The water vapor mixing ratio is derived from the backscattered energy at the shifted Raman frequency at 355 nm. The profiles have a 30 min temporal resolution and a 60 m vertical resolution.

The profiles are only available during nighttime for the period of January 2011 to August 2016. The lidar hatch closes when the MRR (see Section 4.2.1.5) detects rain rates larger than $0.05\,\mathrm{mm\,h^{-1}}$ at any level below 3 km. Values where the estimated error is larger than 10 % are excluded.

4.2.1.5. MRR

The Micro-rain radar (MRR) is a vertically-pointing frequency-modulated continuous-wave radar operating at 24 GHz (X band). The MRR has a 1-min temporal resolution and a range gate of 30 m up to a height of 3 km.

The rain flag is set to 1 when the MRR detects rain rates $> 0.05\,\mathrm{mm\,h^{-1}}$ in at least five range gates.

4.2.2. Cold-pool detection algorithm

We identify cold pools in 1-minute surface temperature data as follows. We first apply a smoothing to the temperature timeseries with an 11-minute centered linear filter. We then classify temperature drops $T_{\mathrm{fil}}(t) - T_{\mathrm{fil}}(t-1) < -0.05\,\mathrm{K}$ in the filtered timeseries as a cold pool. The associated temperature minimum is identified as the minimum of consecutive temperature timesteps. Temperature drops exceeding the $-0.05\,\mathrm{K}$ threshold that occur within 20 min are combined if the temperature does not rise by more than 0.5 K above the previous minimum in between. If another, less abrupt (i.e. not exceeding the $-0.05\,\mathrm{K}$ threshold) temperature drop follows within 20 min, the later minimum is used. The last temperature minimum marks the end of the cold-pool front and is referred to as t_{min}.

The cold pool onset t_{max} is defined as the last instance within 20 min before the initial abrupt temperature drop when $T_{\mathrm{fil}}(t_{\mathrm{max}}) - T_{\mathrm{fil}}(t_{\mathrm{max}} - 1) > 0\,\mathrm{K}$ (or, if the temperature is falling continuously, t_{max} is chosen as the time of the maximum temperature, which then is 20 min before the abrupt temperature drop). We diagnose the temperature drop ΔT as the difference between the maximum temperature $T_{\mathrm{fil}}(t_{\mathrm{max}})$ and the minimum temperature $T_{\mathrm{fil}}(t_{\mathrm{min}})$. The end of a cold pool is either marked by the onset of the next cold pool, or by the time when the filtered temperature first exceeds its minimum by $\Delta T/e$. We only analyse cold pools with $\Delta T < -0.5\,\mathrm{K}$ and less than 2 missing values (NAs) in the filtered temperature timeseries during the entire cold-pool duration.

Our cold-pool detection algorithm is similar to the one used by *de Szoeke et al.* (2017), but with the important modification that we ensure to identify cold pools only for situations with abrupt temperature drops. Identifying cold pools when the temperature is lower than during the previous 20 min (as in *de Szoeke et al.* (2017)) would also select times of steadily but slowly decreasing temperature as potential cold pools, which is rather an advective feature than a cold pool triggered by convection.

Figures 4.3 and 4.4 discussed in the next section show examples of how the algorithm works. The figures demonstrate that the timing and intensity of cold pools detected at the BCO and RP are similar, but not identical, because of the different location and likely also the different instrumentation used.

4.3. Example cases

This section presents timeseries for two example cases characterized by intense cold-pool activity in the dry winter season, the 15 February 2012 and the 19 March 2013. We select these days because there was little to no cold-pool activity the preceding days. This ensures that the cold pools move into an atmosphere that likely is undisturbed by previous deeper convection.

4.3.1. 15 February 2012

The 15 February is characterized by a major cloud system evident in the satellite images in Fig. 4.2b-c. Fig. 4.3 shows that the system reached the BCO at 6.30 UTC (2.30 LT) and intense convection and precipitation lasted for about 24 h. The first weak cold pool was recorded at 6.30 UTC and coincided with the first deeper precipitating cloud moving over the site. The next two cold pool fronts followed immediately after, and reduced the surface temperature from about 25.7°C to 23.1°C. Subsequent cold-pool fronts were recorded in 1.5–2 h intervals, until the temperature recovered fully at around 17 UTC. The red circles in the satellite image in Fig. 4.2 c indicate two mesoscale arcs, which were likely triggered by the cold-pool fronts moving over the site at 17 UTC and shortly after 18 UTC. The radar reflectivity suggests that the convective cores between 17 UTC and 22 UTC were further away from each other and produced shorter-lasting rain pulses, such that the temperature recovered more quickly after the cold-pool passages.

Surface rain was registered during all detected cold-pool fronts (Fig. 4.3c). The MRR detects rain also well into the cold-pool wake, as long as deeper clouds are present with large hydrometeors at some levels in the lowermost 3 km. The surface specific humidity tends to drop in the front and quickly recover thereafter (Fig. 4.3d). Strong gust fronts accompany the cold-pool fronts, with wind speed increases up to $5\,\mathrm{m\,s^{-1}}$ (e.g. at 10.30 UTC).

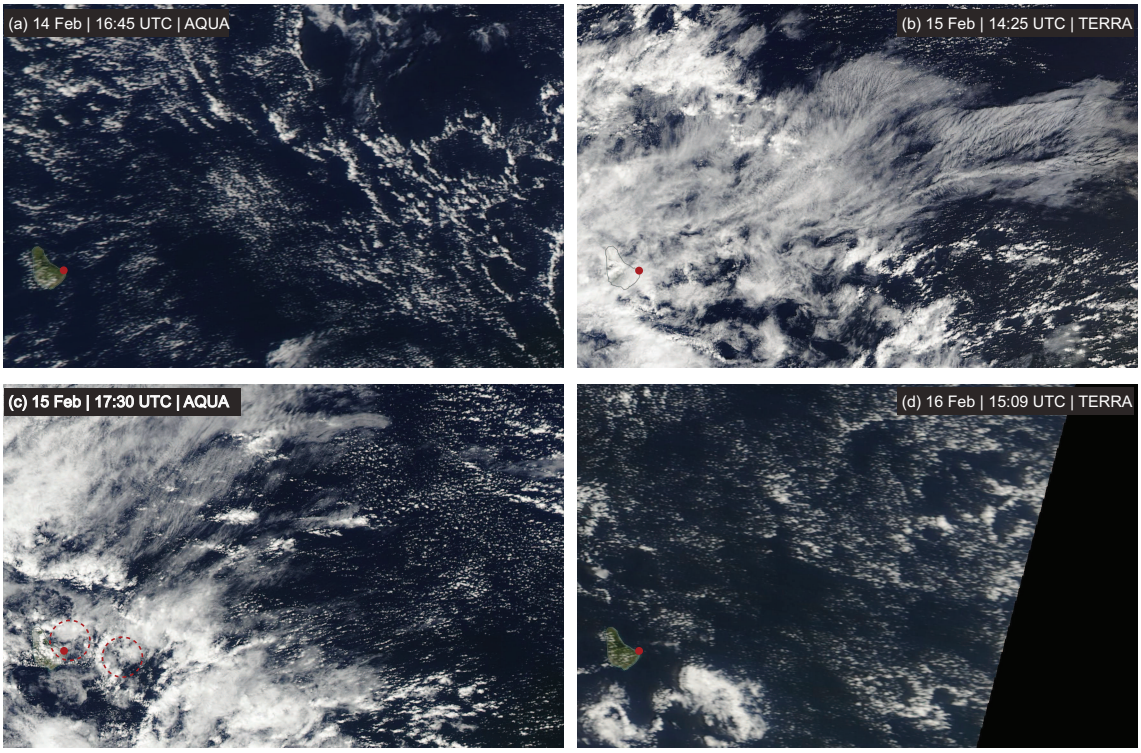

Figure 4.2.: Visible satellite images from MODIS for the area 12.5–15°N, 56–59.85°W between 14 and 16 February 2012 with Barbados located in the lower left corner. The respective recording time and satellite is indicated on the panels. The two cold-pool fronts indicated in panel (c) have radii of about 15 km.

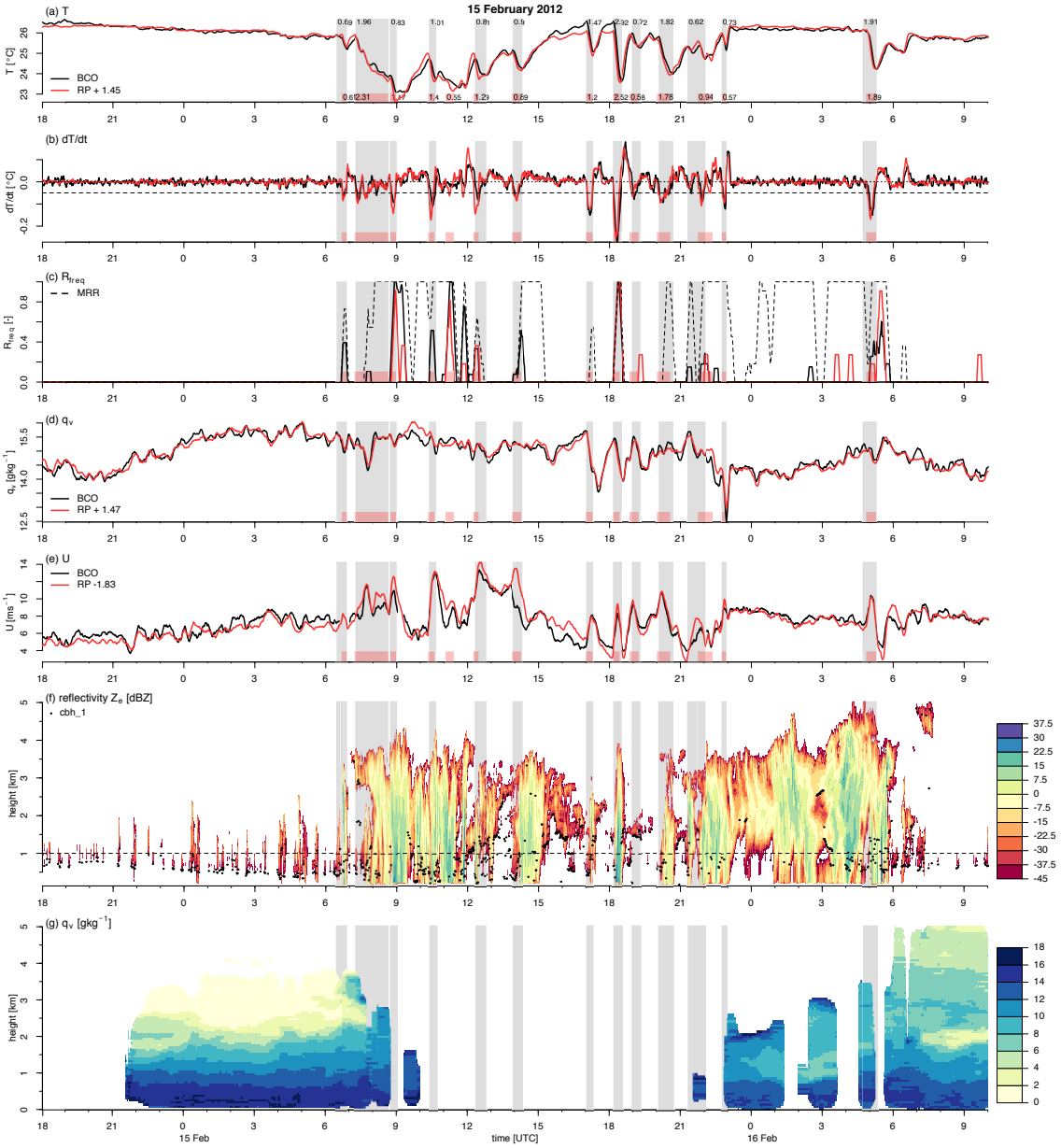

Figure 4.3.: Example of detected cold pools on 15 February 2012 (from 18 UTC on 14 February until 10 UTC on 16 February) for (a) air temperature, (b) temperature change , (c) rain frequency, (d) specific humidity, (e) wind speed from the surface weather stations at BCO (black) and RP (red). Profiles of (f) equivalent radar reflectivity from the KATRIN radar and (g) specific humidity from the Raman lidar at the BCO. Also shown are the rain frequency from the MRR in (c) and the cbh1 from the ceilometer in (f). Cold pool fronts are shaded in grey (BCO) and red (RP), and the respective $-\Delta T$ is indicated in panel (a). The timeseries in panels (a)-(e) are smoothed with a 11-min centered linear filter. The RP temperature, specific humidity and wind speed data is shifted compared to the BCO data by the amount specified in the respective legend. The relatively constant offset between RP and BCO arises from the 25 m height difference, as discussed in Section 4.2.1.1.

Before the passage of the first cold-pool front, the specific humidity increased from about $14\,\mathrm{g\,kg^{-1}}$ at 21 UTC on 14 February to about $16\,\mathrm{g\,kg^{-1}}$ at 4 UTC on 15 February. The specific humidity increase went along with a steady increase in wind speed and a steady reduction in temperature. During this time, clouds deepened beyond 2 km (Fig. 4.3f), along with a deepening of the moist layer as indicated by the lidar (Fig. 4.3g). The vertical humidity structure strongly differs before and after the passage of the cloud system and the intense cold-pool activity. The specific humidity decreased steadily with height in the early morning on 15 February, with the inversion layer located at about 2 km height. The strong humidity stratification was broken up after the passage of the system, with moisture mixed over a deeper layer and dry intrusions in-between.

The very steady temperature in the early morning of 16 February marks another interesting feature. Both the radar and the MRR indicate high reflectivities, but the surface remains unaffected by the deeper convection.

The 4 km deep precipitating cloud system which likely triggered the strong cold-pool front reaching the site at 7.15 UTC on 15 February moved over the site about 30 min after the cold-pool onset. It appears that for this cloud system, the cold pools might not have affected the dynamics of the system much, but were rather dragged along with it. This is similar to observations of drizzling marine stratocumulus in *Wilbanks et al.* (2015), which suggest that cold pools are often not the primary process initiating the mesoscale organization, but rather a tracer of stratocumulus precipitation.

Fig. 4.3a-e demonstrate how remarkably well the temporal fluctuations in the surface properties match between the BCO and RP. Also the timing and intensity of cold pools in the two datasets matches very well.

4.3.2. 19 March 2013

The 19 March 2013 is a slightly different, and perhaps more classic case of trade-wind cumulus cold pools. Fig. 4.4 shows an individual strong cold pool which passed the site at 1 UTC, associated with a large cloud system moving over the site from 0.30–3.30 UTC. The temperature fully recovered within 3 h after the cold-pool onset, which was about one hour after the last surface precipitation. Despite sustained precipitation, the humidity recovered quickly after a strong drop in the front. The wind speed indicates two gust fronts, which were particularly pronounced at RP (Fig. 4.4).

A second system passes the site with an active core around 12–13.30 UTC, which brings along less precipitation and only weak cold pools. Another suite of cold pools are recorded at 18 UTC, 19.15 UTC and 21.30 UTC. The weak cold pool passing the site at 18 UTC likely coincides with the cold pool responsible for the mesoscale arc highlighted in the satellite image (Fig. 4.5c). This cold-pool arc had a radius of about 50 km and had already partly recovered when reaching the BCO. No coincident cloud was identified by

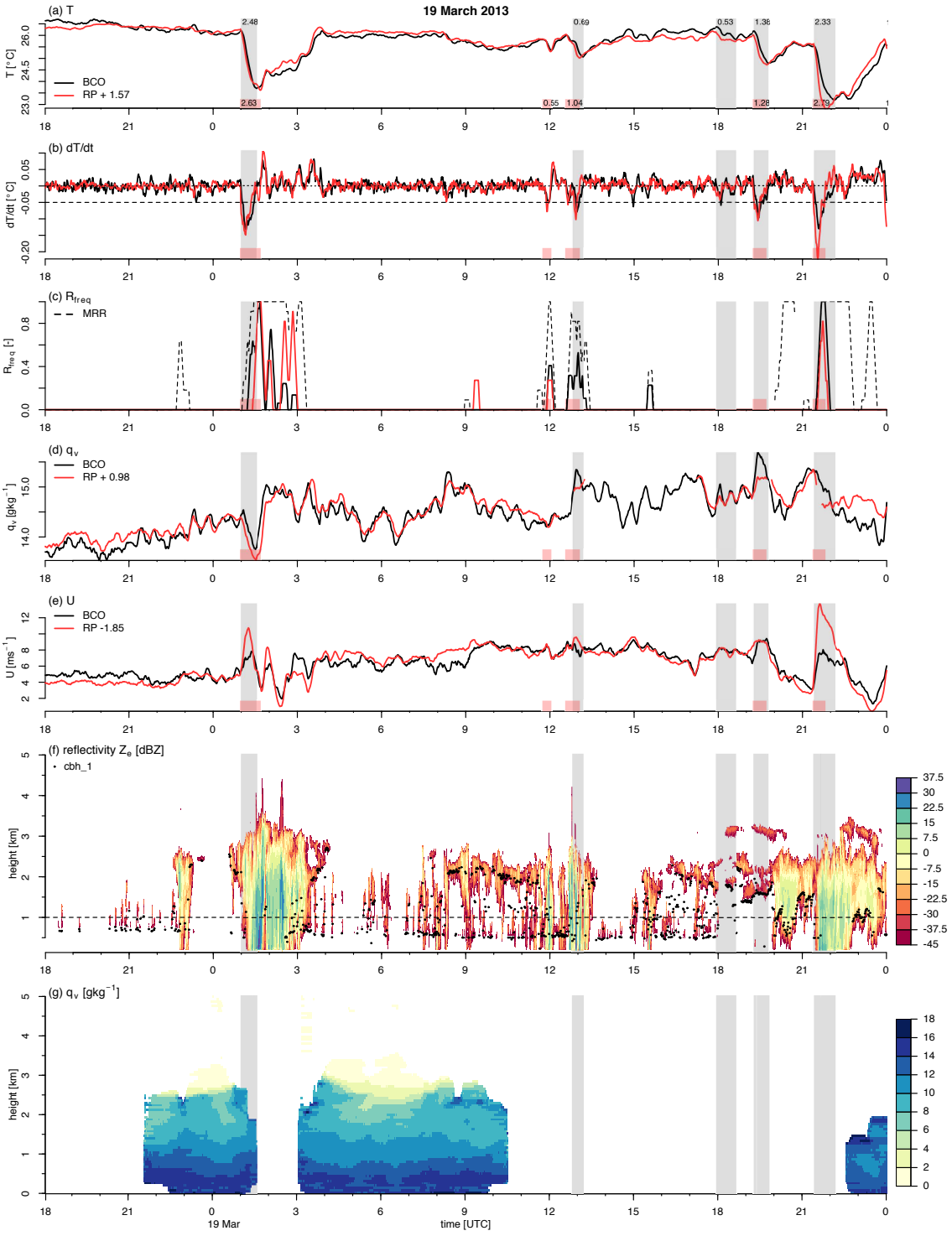

Figure 4.4.: Same as Fig. 4.3, but for 19 March 2013 (starting at 18 UTC on 18 March).

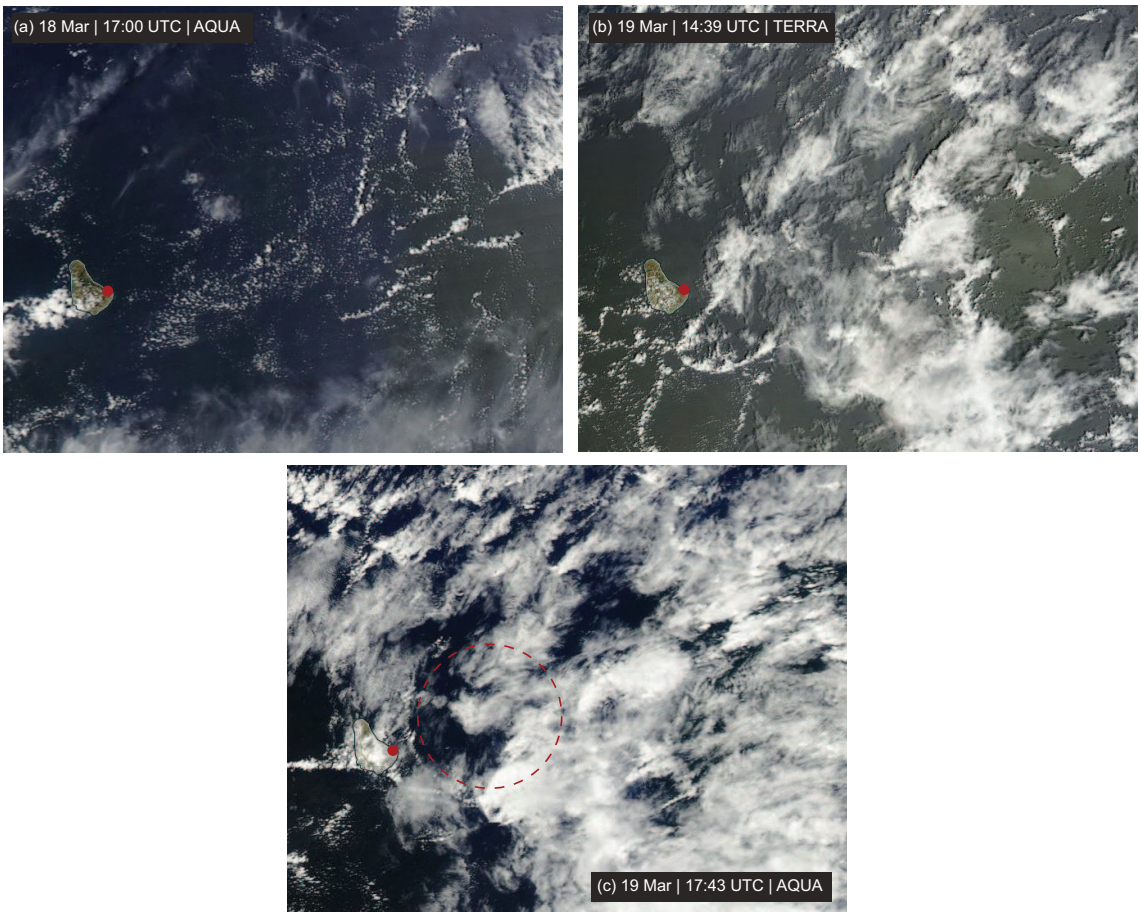

Figure 4.5.: Same as Fig. 4.2, but for 18 and 19 March 2013 and the area 12.3–17.7°N, 57–60°W. The cold-pool arc indicated in panel (c) has a radius of about 50 km.

the BCO radar (Fig. 4.4 f).

The humidity structure shows a relatively deep moist layer of about 2.5 km depth (Fig. 4.4g). Clouds coincided with an increase in specific humidity indicative of vertical moisture transport by the convective cores (e.g. at 23 UTC on 18 March and between 1 UTC and 4 UTC on 19 March). Otherwise, the vertical humidity structure did not differ much before and after the cold-pool passage.

4.4. Cold-pool statistics

4.4.1. General statistics

The example cases in the previous section gave an impression of the structure, strength, and variability of cold pools and the associated convection. In this section, we present statistics of various cold-pool diagnostics for the 9.5 years of RP data. In total, 8023 cold pools were detected which meet the criteria of $\Delta T < -0.5\,\mathrm{K}$ and less than two missing values in the filtered temperature timeseries.

Table 4.1.: Quantiles of different diagnostics for all the cold pools detected at RP with $\Delta T > 0.5\,\mathrm{K}$ and less than two NAs in the filtered temperature timeseries. Shown are ΔT [K], Δq_{min} [$\mathrm{g\,kg^{-1}}$], $\Delta\theta_{\mathrm{e,min}}$ [K] and ΔU_{max} [$\mathrm{m\,s^{-1}}$], the latter three referring to the minimum or maximum difference of the quantity in the cold-pool front compared to the value at t_{max}. $\mathrm{R_{freq}}$ [-] is the average in-front rain frequency, dur [min] is the total duration of the cold pool, front dur and wake dur refer to the respective duration of the cold pool front and wake [min]. The last row shows the % of time spent in a cold-pool front, and the last column '#' shows the number of samples for the specific diagnostic.

	q0 %	q1 %	q5 %	q10 %	q25 %	q50 %	q75 %	q90 %	q95 %	q99 %	q100 %	#
ΔT	-0.50	-0.51	-0.55	-0.59	-0.74	-1.07	-1.64	-2.39	-2.93	-4.02	-7.42	8023
Δq_{min}	0.40	0.09	0.05	0.02	-0.09	-0.78	-0.38	-1.22	-1.56	-2.28	-5.12	7930
$\Delta\theta_{\mathrm{e,min}}$	0.52	0.20	0.06	-0.23	-1.03	-2.06	-3.45	-5.20	-6.46	-9.68	-16.32	7930
ΔU_{max}	-0.78	-0.17	-0.0	0.20	0.78	1.64	2.91	4.39	5.38	7.49	13.07	5617
$\mathrm{R_{freq}}$	0	0	0	0	0	0.22	0.55	1	1	1	1	8023
dur	12	15	18	20	25	34	50	72	92	171	754	8023
front dur	6	11	12	13	15	20	29	42	50	73	167	8023
wake dur	0	4	5	6	8	11	20	35	51	124	662	8023
% of day in front	0	0	0	0	0	0.03	0.07	0.12	0.15	0.20	0.34	3128

Table 4.1 shows that 50 % of all cold pools have a ΔT smaller than $-1.07\,\mathrm{K}$ across the front, a maximum in-front humidity reduction exceeding $0.38\,\mathrm{g\,kg^{-1}}$, a θ_{e} reduction exceeding 2.06 K, a maximum in-front wind speed increase larger $1.64\,\mathrm{m\,s^{-1}}$, and an in-front rain frequency of more than 22 %. The strongest 1 % of ΔT are smaller than $-4\,\mathrm{K}$, and the strongest humidity reductions and wind speed increases are larger than $2.28\,\mathrm{g\,kg^{-1}}$ and $7.5\,\mathrm{m\,s^{-1}}$, respectively. As will be shown in Section 4.4.2, stronger temperature depressions tend to go along with larger humidity and θ_{e} decreases, larger wind speed increases and larger rain frequencies in the front. The numbers presented here are broadly consistent

with the ones in *Zuidema et al.* (2012) (see their Figure 3).

The median duration of the cold-pool front is 20 min, followed by a cold-pool wake lasting for 11 min. The recovery of a cold pool, and therefore the wake duration (if the cold pool is not impinged on by a subsequent cold pool), is difficult to define. Here we define a cold pool as recovered once the low-pass filtered temperature rises by $\Delta T/e$ above $T_{\min}$ (as in *de Szoeke et al.* (2017)), which leads to 94 % of cold pools recovering. Multiplying the median cold pool duration of 34 min with the median wind speed of 8.1 m s^{-1} yields a median size of cold pools of 16.5 km. The example cold pools from the LES displayed in the Figures 2.9 and 3.6 have radii of ∼13 km. Visual inspection of other snapshots of LES cloud fields indicates that simulated cold-pool radii are on the order of 5–15 km, which compares reasonably well with the observations.

To put the examples of the previous section in context with the long-term statistics, the cold-pool front which moved across the BCO at 1 UTC on the 19 March 2013 pertains to the strongest 10 % in terms of ΔT. The wind speed increase $\Delta U_{\max}$ of 5.8 m s^{-1} pertains to the 5 % largest, the $\Delta q_{\min}$ of -0.84 g kg^{-1} to the 25 % strongest, and the front duration of 43 min to the 10 % longest-lasting fronts.

We find that on 70 % of the days analyzed at least one cold-pool front is detected. 10 % of the days spend up to 3 h in a cold-pool front. For comparison, on the example days discussed, 5 h (15 February 2012) and 2.5 h (19 March 2013) were subject to cold-pool fronts, respectively.

The 9.5-year dataset at RP also allows to study the seasonality of the cold-pool characteristics. Fig. 4.6 displays boxplots of ΔT, $\Delta q_{\min}$, R_{freq} and the '% of day in front' for every month separately, and for 3-month periods representing boreal winter (February, March, and April) and boreal summer (August, September, and October). There is a hint of slightly stronger temperature depressions in the summer regime, most evident for the 75 % quantile. Seasonal changes in the in-front humidity reduction are slightly more pronounced, with the distribution shifting to stronger humidity reductions in the summer regime. Cold-pool fronts also tend to be associated with a higher rain frequency in summer, which reflects the fact that precipitation is both more frequent and stronger in the wet summer regime (see Figure 1.3 in the introduction). Furthermore, days without any cold-pool front are slightly less frequent in the summer regime than in the winter regime.

Despite a tendency towards stronger cold-pool activity in the summer regime, the seasonal changes of the cold-pool characteristics are overall modest. Other diagnostics like $\Delta U_{\max}$ show no seasonal cycle at all (not shown). Likewise, no pronounced diurnal cycle of cold-pool activity was found (not shown).

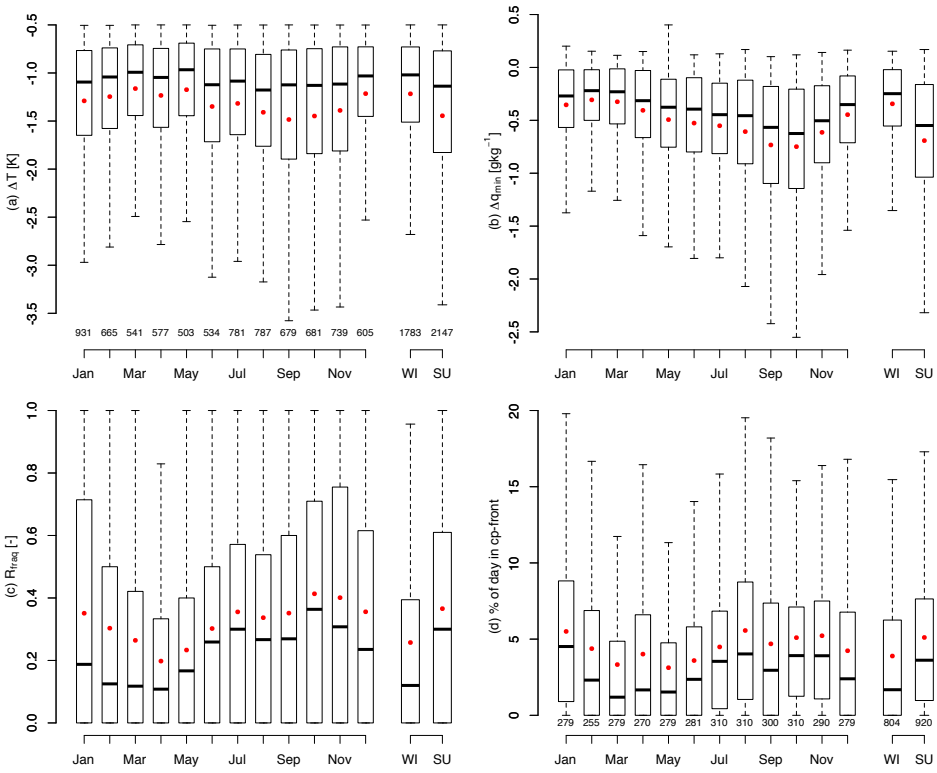

Figure 4.6.: Boxplots of monthly and seasonal distribution of (a) ΔT, (b) $\Delta q_{\min}$, (c) R_{freq}, and (d) '% of day in front' for cold pools detected at RP. The winter regime (WI) is represented by the period February-April, and the summer regime (SU) by August-October. The boxes represent the 25th, 50th and the 75th percentile, and the whiskers extend to ±1.58 IQR/sqrt(n), where n is the number of samples (which is indicated in panel a (valid for panels a-c), and in panel d). The red dots mark the monthly mean.

4.4.2. Temporal structure

In this subsection, we analyse the temporal structure of the cold pools. To facilitate the comparison of different cold pools, we use a normalized time coordinate in the cold-pool front with values mapped onto 20 points (the median duration of the front), similar to previous studies (*Young et al.*, 1995; *de Szoeke et al.*, 2017; *Zuidema and Torri*, 2017). We limit our analysis to cold pools that move into an atmosphere unmodified by previous cold pools and precipitation by applying an additional criterion of no precipitation and no previous cold-pool wake in the hour prior to the cold-pool onset.

For the composite-mean cold pool in Fig. 4.7, the temperature decreases rapidly in the front and recovers by $\Delta T/e$ within 11 min after the front. The temperature remains about 0.5 K below the pre-front value in the hour after the frontal passage. The surface humidity initially increases in the front and only then decreases to a minimum at $t_{\min}$. The humidity recovers more quickly to its pre-front value than the temperature. A reason for this might be continued evaporation of precipitation, which would cool and moisten the

air in the cold-pool wake. The initial increase in humidity at the edge of the front might be explained by surface fluxes (*Langhans and Romps*, 2015; *Torri and Kuang*, 2016) or by an accumulation of moisture from evaporation of precipitation of the parent convection, which was pushed to the edge of the front (*Tompkins*, 2001). We find similar rings of enhanced humidity at the edge of the cold-pool front in the LES (see Fig. A.2 in the appendix).

Governed by the temperature changes, the relative humidity in Fig. 4.7c increases in the front and slowly decreases thereafter. The in-front wind speed increase has a maximum in the middle of the front. After the frontal passage, the wind speed decreases below the pre-front level. The wind turns clockwise by about 4° in the front and stays constant in this altered direction in the cold-pool wake. The rain frequency increases in the front, peaks at $t_{\min}$, and rapidly decreases after the front.

To investigate whether the temporal structure of the cold pools differs between RP and BCO, we compare the temporal structure for RP (solid grey line) and BCO (dotted grey line) during the period of joint operation from January 2011 to November 2016 (Fig. 4.7). The different sample size does not influence the temporal structure at RP compared to the full sample. While the structure at the BCO is largely consistent with RP, a few interesting differences arise, which are likely related to the different sampling height (the BCO is ~ 22 m a.s.l. and RP about ~ 47 m a.s.l.). Fig. 4.7b shows a more pronounced specific humidity increase before $t_{\max}$ at the BCO, and also a stronger increase at the beginning of the front. The in-front wind speed increase is somewhat weaker at the BCO, and the increase in rain frequency is shifted to earlier times in the front. The stronger in-front wind speed increases at RP are also evident in Fig. 4.4 on 19 March 2013.

The temporal structure conditioned on the lowest quartile (red) and the highest quartile of ΔTs (blue) shows that stronger cold pools are associated with higher rain frequencies and have stronger in-front humidity reductions, wind speed increases and wind direction changes. However, there is a lot of variability between individual cold pools. The variability is illustrated in Fig. 4.8, which shows the temporal structure of individual cold pools, ranked according to their ΔT. Both the mean structure and the variability among cold pools is similar to observations of tropical cold pools described in *de Szoeke et al.* (2017) (see their Figures 5 and 7).

The next sections discuss how cloud properties and the vertical humidity structure change relative to the passage of cold-pool fronts, and focus on data collected at the BCO.

4.4.2.1. Cloudiness

In this section, we relate the ceilometer-derived cloud cover and the radar-derived maximum cloud-top height ($\mathrm{CTH_{max}}$) to the onset of the cold pools. Again, we only consider cold pools which move into an atmosphere unmodified by previous cold pools and precip-

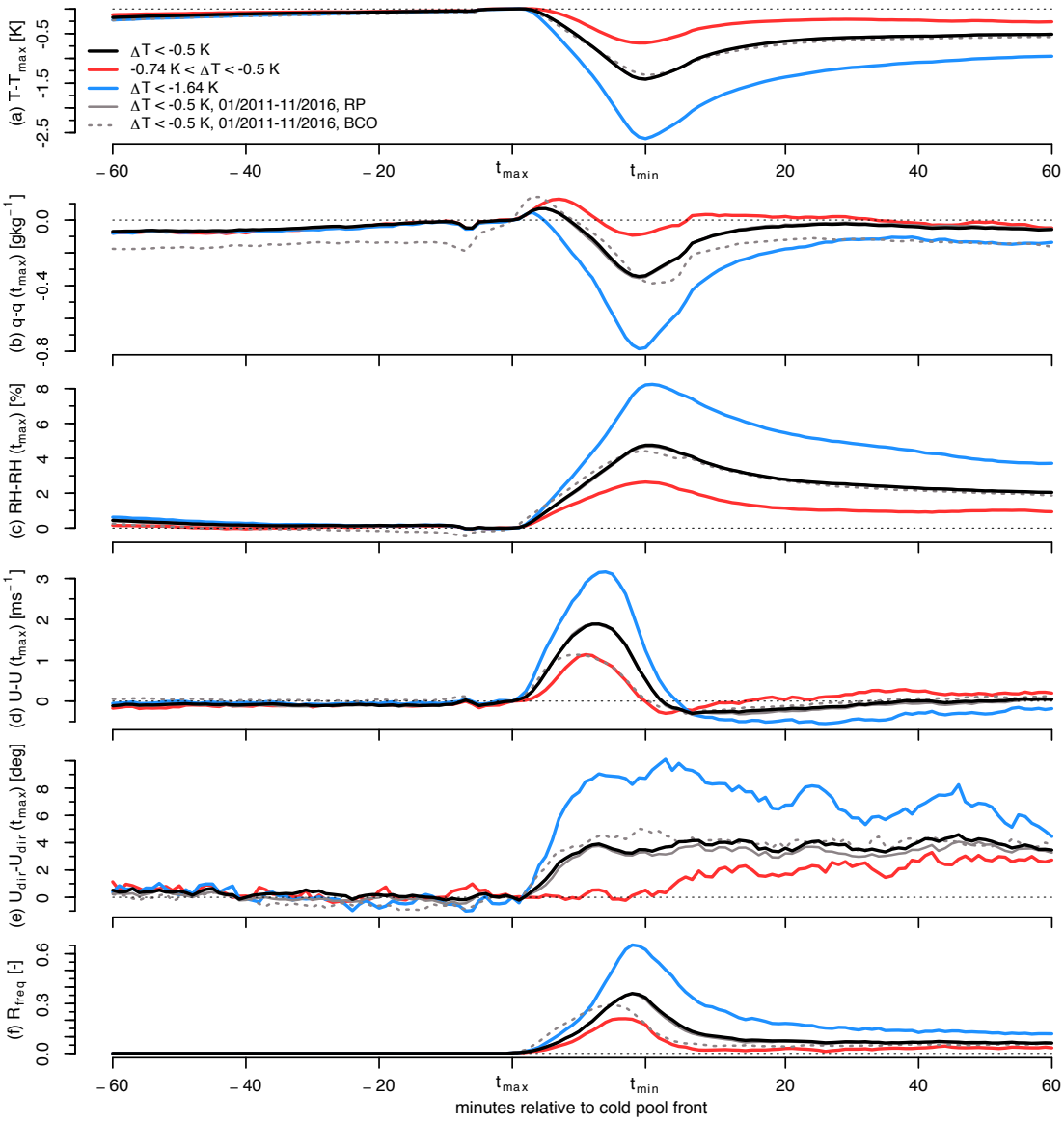

Figure 4.7.: Mean temporal structure of anomalies relative to the cold-pool front ($t_{\max}$) for the surface properties (a) temperature, (b) specific humidity, (c) relative humidity, (d) wind speed, (e) wind direction, and (f) rain frequency. The black line shows the mean structure of all the cold pools at RP with $\Delta T < -0.5\,\mathrm{K}$ and no rain and no wake of a previous cold pool in the hour prior. The red (blue) line shows the mean for cold pools with ΔT lower than the 25 % quartile (larger than the 75 % quartile) at RP. The darkgrey lines show the mean structure at RP (solid) and BCO (dashed) for the period of joint operation (i.e. January 2011 to November 2016).

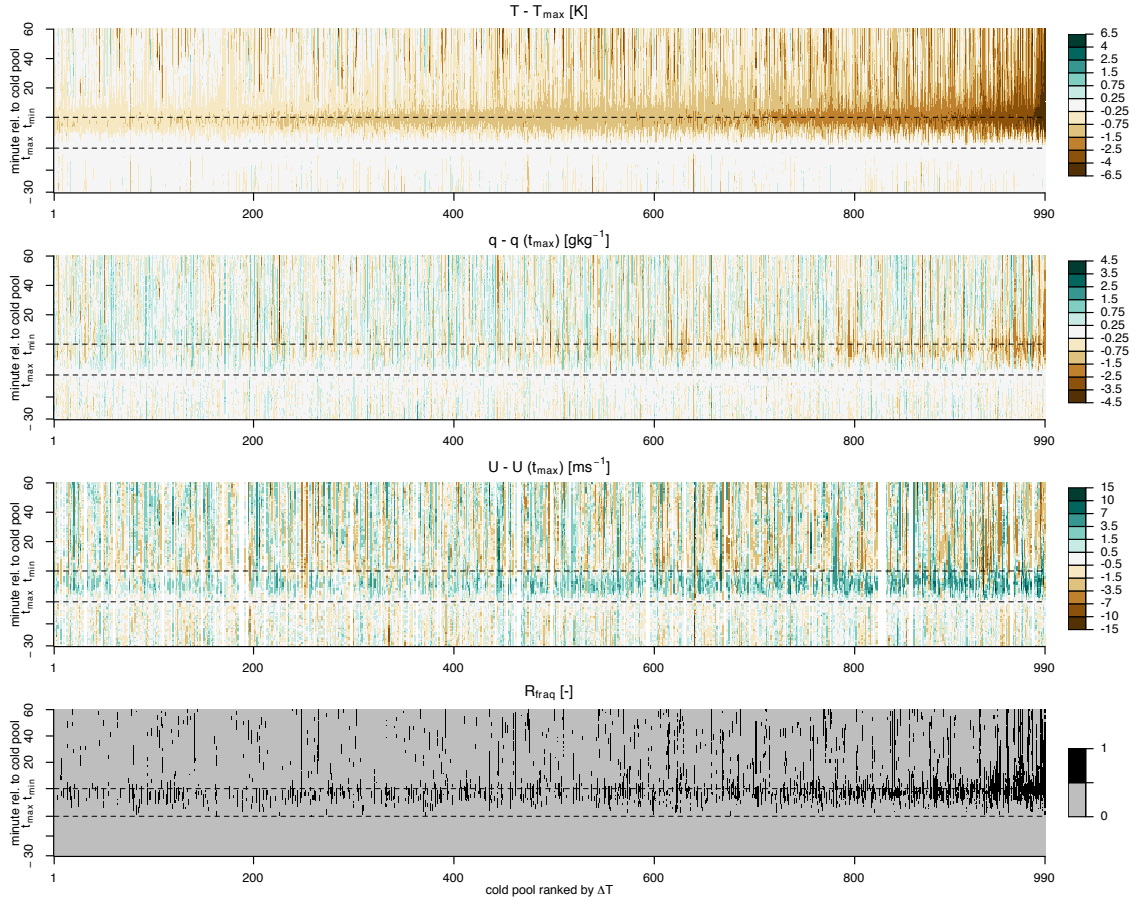

Figure 4.8.: Temporal structure of individual cold pools at RP ranked according to their ΔT. Shown are temperature, specific humidity, wind speed, and rain frequency anomalies relative to $t_{\max}$. Only every 4th cold pool of the ranked sample is shown.

itation, and apply the additional criterion of no precipitation and no previous cold-pool wake in the hour prior to the cold-pool onset.

The composite mean cloud cover in Fig. 4.9b (black) increases before the front and maximizes at the edge of the front. Inside the cold-pool front, cloud cover decreases and remains at a slightly elevated level in the cold-pool wake compared to the hour before the cold-pool onset. The increase in cloud cover before the cold-pool front is due to a 25 % increase in CC_{LCL}, and likely manifests the triggering of new convection at the cold-pool front. Fig. 4.9e shows that the clouds at the edge of the front are not deeper than the clouds in the hour prior to the front. Furthermore, the temporal structure of CC_{LCL} does not show a strong difference between cold pools with weak (red) and strong temperature depressions (blue). Hence, surface-forced convection at the front does not seem to depend much on the strength of the cold pool and the gust front induced.

In contrast to CC_{LCL}, CC_{ALOFT} tends to decrease before the cold-pool onset and increase in the front. CC_{ALOFT} also shows more pronounced in-front differences between weaker and stronger cold pools. Whereas CC_{ALOFT} increases in the front of the weaker cold pools, it remains at a depressed level during the entire front for the stronger cold pools. Stronger cold pools therefore have lower CC_{ALOFT} in the front than the weaker cold pools despite clouds being on average about 800 m deeper (Fig. 4.9e). Increases in CC_{ALOFT} can be either due to clouds deeper than 1 km having irregular shapes or being sheared, or due to stratiform cloud layers (*Nuijens et al.*, 2014). The more pronounced sensitivity of in-front CC_{ALOFT} to the cold-pool strength might therefore reflect the LES result that stratiform cloud layers are less frequent when much deeper convection weakens the inversion and inhibits radiative feedbacks that promote and maintain the stratiform layers (see Figures 3.5 and 3.6).

Overall, cloud cover is enhanced compared to the 5-year mean when cold pools are present. Cloud cover during the entire period from one hour before to one hour after the cold-pool front is on average 55 %, compared to about 34 % cloud cover in the yearly mean (see the dashed lines in Fig. 4.9b-d). That the CC_{LCL} in the hour after the cold-pool front tends to be about as large as the longterm mean is remarkable, as convection might be expected to be suppressed in the cold-pool wake. The satellite images in Fig. 4.2b–c and Fig. 4.5b–c with their vast cloud decks might therefore be more representative for periods of cold-pool activity than the more classical picture of mesoscale cold-pool arcs enclosing broad clear-sky regions (as in the satellite image in Fig. 1.2 of the introduction). One reason for cold-pool periods being very cloudy is that they often occur within larger cloud systems (as for example on 15 February 2012 in Fig. 4.3), in which they are mostly dragged along with the system, rather than contributing to organizing the convection. The large CC_{LCL} in the hour after the cold-pool front might also be due to the clouds producing the cold pool being advected over the site. Relying on measurements taken at a single site, it

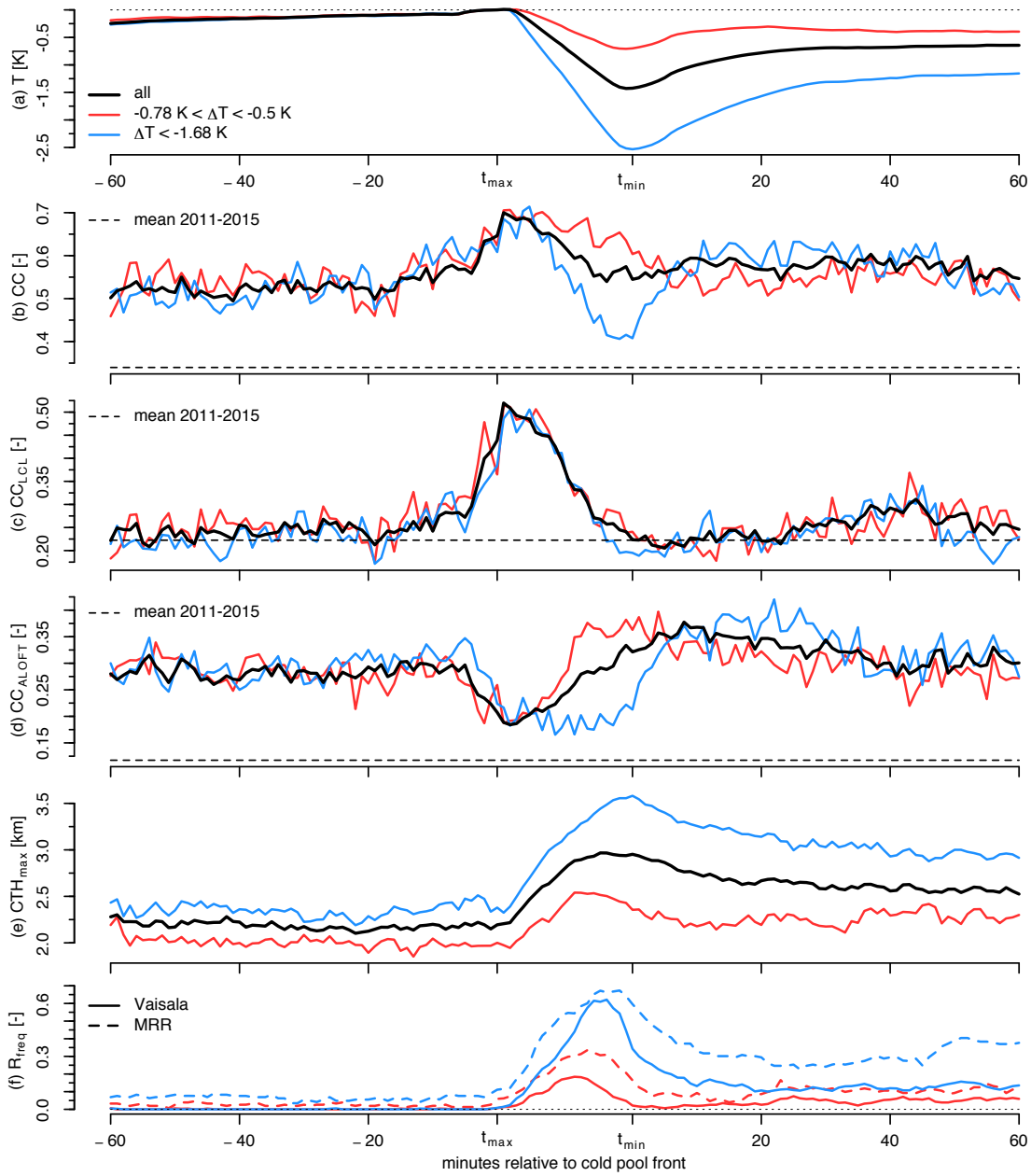

Figure 4.9.: Same as Fig. 4.7, but for cloud properties at the BCO. Shown are (a) surface temperature, (b) total low-level cloud cover, (c) $\mathrm{CC_{LCL}}$, (d) $\mathrm{CC_{ALOFT}}$, (e) $\mathrm{CTH_{max}}$, and (f) the rain frequency both at the surface (from the Vaisala sensor) and from the MRR (dashed). For the cloud properties in panels (b)-(e), we do not show the anomaly relative to $t_{\max}$, but the absolute values. Only the 625 cold pools are used with at least 70 min of both ceilometer and radar data before, inside, and after the cold-pool front (156 for the quartiles in red and blue, respectively). The dashed lines in panels b–d indicate the respective sample mean cloud cover for the entire operation period of the ceilometer (January 2011 to June 2015).

is in general hard to distinguish between new clouds triggered at the cold-pool front and the clouds that triggered the cold pool being advected over the site.

4.4.2.2. Vertical humidity structure

In this section we discuss anomalies in the vertical humidity structure relative to the cold-pool onset. The mean temporal structure of surface humidity changes is similar to the structure of mixed-layer humidity changes at 400 m (Fig. 4.10b-c). For both, the humidity increases before the cold-pool onset, decreases in the front, and tends to recover afterwards. The pre-front humidity increase and the in-front humidity decrease are somewhat more pronounced at 400 m than at the surface (note the different scale of Figs 4.10b and 4.10c). The humidity at 400 m does not recover as rapidly after the frontal passage as the surface humidity, which might be explained by the gradual deepening of a newly developing mixed layer during the recovery process (as sketched in Figure 19 of *Zuidema et al.* (2012)).

In the lower cloud layer around 1 km (Fig. 4.10d), the humidity increases before the cold-pool onset, maximizes in the front and decreases afterwards. The temporal structure at 2 km is similar to the structure at 1 km, but the humidity maximum is shifted towards the end of the front. The humidity at 2 km remains above its pre-front value for more than an hour after the front. The increase in cloud-layer humidity in the front is consistent with the deepening of clouds evident in Fig. 4.9e.

The different temporal structures at different height levels indicate changes in the vertical humidity stratification. The humidity becomes more homogeneously distributed in the vertical, as indicated by the smaller humidity difference between 0.4 km and 1 km (Δq_{TL}), and between 1 km and 2 km (Δq_{CL}). While the decrease in Δq_{TL} recovers relatively quickly in the cold-pool wake, the strong decrease in Δq_{CL} towards the end of the front does not recover in the hour after the front. The more well-mixed cloud layer in the hour after the cold-pool front is consistent with clouds being deeper in the hour after the front compared to the hour before the front (Fig. 4.9e). That the Δq_{CL} does not show a sign of recovery in the hour after the frontal passage suggests that the deeper and organized convection inducing the cold pool might influence the structure of the trade-wind layer on timescales longer than an hour.

The 25 % cold pools of the sample with the largest temperature depressions (blue) have stronger humidity depressions at the surface and around 400 m, and a stronger increase in cloud-layer humidity in the front than cold pools with the smallest 25 % of temperature depressions (red). This likely reflects deeper and larger clouds transporting more moisture into the cloud layer, and generating more precipitation and stronger downdrafts (as in Fig. 4.9e-f for the 75 % quantile).

Cold pools from the LES show a similar coincidence of dry anomalies in the mixed layer at 400 m and moist anomalies in the cloud layer at 2.9 km (see Fig. A.2 in the appendix).

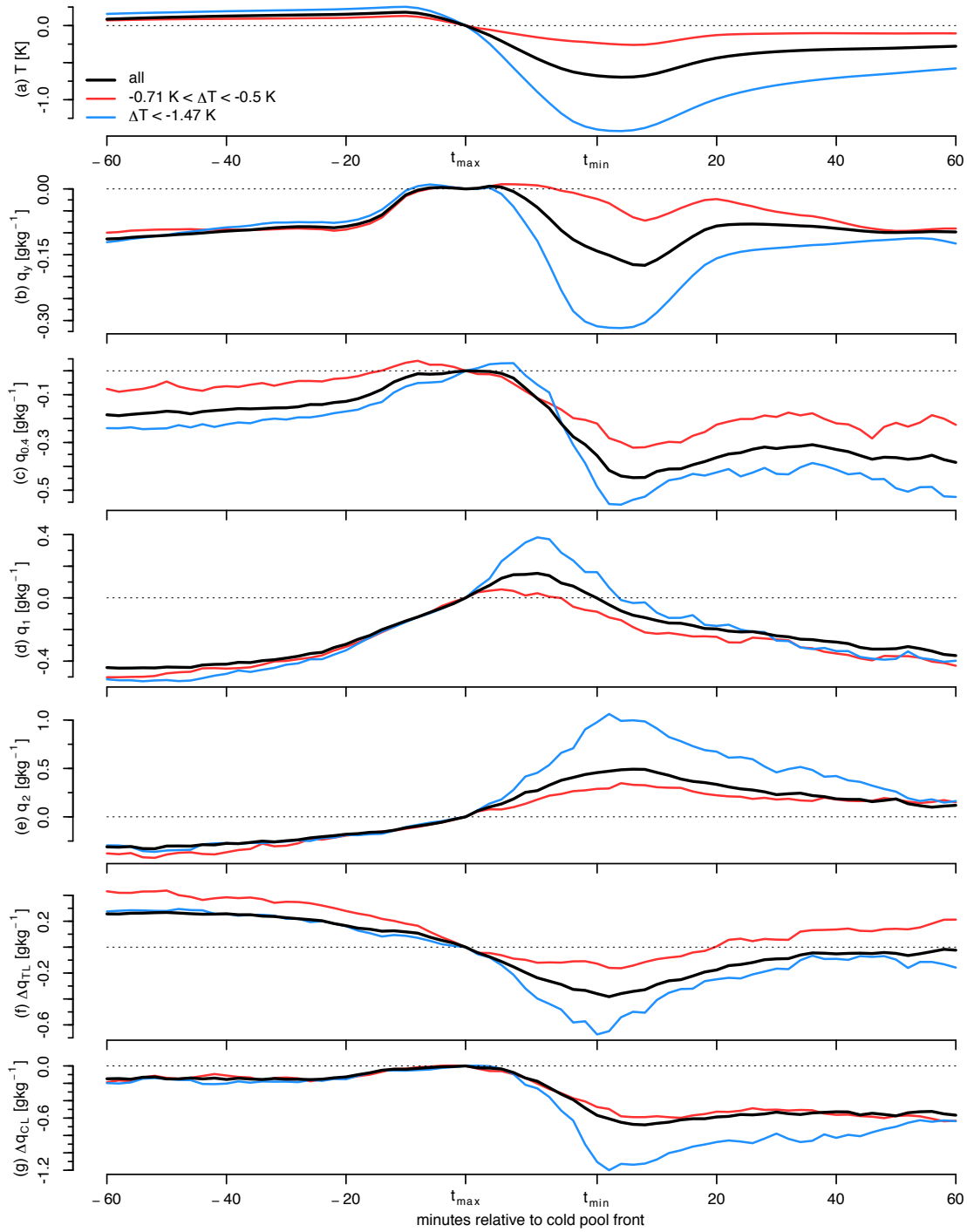

Figure 4.10.: Same as Fig. 4.7, but for the vertical humidity structure at the BCO. Shown are (a) surface temperature and (b) surface specific humidity, both smoothed with a 30 min centered filter to match the resolution of the lidar. $q_{0.4}$, q_1 and q_2 in panels (c)–(e) refer to the lidar specific humidity averaged over 5 range bins (equivalent to 240 m) centered at 380 m, 980 m and 2 km. Δq_{TL} and Δq_{CL} in panels (f) and (g) refer to the humidity change across the transition layer (cloud layer), defined here as $q_{0.4}$-q_1 and q_1-q_2. Δq_{TL} gives a sense of how well-mixed the lower trade-wind layer is, but the 600 m window cannot resolve the sharp jump in humidity across the transition layer. The broad window is used to facilitate the comparison of different cold pools. Only the 860 cold pools are used with at least 1 h of humidity data at 380 m and 980 m before, inside, and after the cold-pool front (215 for the quartiles in red and blue, respectively).

4.5. Conclusions

The large-eddy simulations (LES) presented in the previous chapters of this thesis highlight the strong influence of deeper and organized shallow convection on cloudiness and the vertical humidity structure in the trades. Here we present an analysis of the statistics of spatial organization of shallow convection as identified by cold pools in 9.5 years of surface weather data at Barbados. The analysis of the structure and seasonal variability of cold-pool characteristics is supported by more than 5 years of coincident ground-based remote sensing of clouds and the vertical humidity structure from the Barbados Cloud Observatory (BCO). The long timeseries allows us to explore changes in the surface meteorology, in the vertical humidity structure, in cloud depth and in cloud cover relative to the passage of cold-pool fronts.

Cold pools are ubiquitous at Barbados. 70 % of the days analyzed are subject to modifications in the lower troposphere associated with the passage of cold-pool fronts. Cold pools with stronger temperature depressions in the cold-pool front tend to be associated with stronger in-front increases in cloud-top height and wind speed, higher precipitation frequencies, stronger surface humidity drops, and a more homogeneously mixed vertical humidity structure. A comparison of seasonal differences reveals that cold pools in the wet summer regime occur slightly more frequently and induce slightly stronger humidity drops, in line with the more frequent deep convection and the more frequent and more intense precipitation in the summer regime (see Fig. 1.3). We find no seasonal differences in the strength and variability of associated in-front temperature depressions and wind speed increases. The temporal structure of changes in surface properties induced by cold pools at Barbados resembles the temporal structure of a smaller sample of deep convective cold pools as observed during the DYNAMO experiment over the central Indian Ocean (*de Szoeke et al.*, 2017). The statistics agree with the cold pools sampled during 2-weeks of the RICO field campaign (*Zuidema et al.*, 2012). The size and structure of the observed cold pools also compares well with the simulated cold pools from the LES.

We also analyze changes in cloud properties relative to the cold-pool onset. Cloud cover peaks at the edge of the cold-pool front due to a 25 % absolute increase in clouds forming near the lifting condensation level (CC_{LCL}). Interestingly, the increase in CC_{LCL} before the front is independent of the strength of the in-front temperature depression. Hence, the new convection triggered by the thermodynamic and dynamic perturbations associated with the cold-pool front does not seem to depend much on the strength of the cold pool. Contrastingly, the cold-pool strength influences the contribution to total cloud cover from cloudiness at cumulus tops near the trade-wind inversion (CC_{ALOFT}). CC_{ALOFT} is about 15 % lower in those cold-pool fronts with strong temperature drops as compared to weak temperature drops, despite clouds being on average 800 m deeper.

In the presence of cold pools, cloud cover is enhanced compared to the 5-year mean.

Furthermore, the composite-mean CC_{LCL} in the hour after the cold-pool front tends to be about as large as the longterm mean. This is a somewhat surprising result because one might expect convection to be suppressed in the wake of cold-pool fronts, as satellite images of mesoscale arcs tend to suggest (see the broad clear-sky area in the satellite image in Fig. 1.2). But the cold pools often occur within larger cloud systems, in which they do not have a strong effect on the organization of convection (reflecting observations of stratocumulus cold pools described in *Wilbanks et al.* (2015)). The analyses presented in this chapter focus on the instantaneous influence of cold pools, and therefore do not address the influence of organized shallow convection on cloudiness and the vertical humidity structure on longer timescales. Because of the important implications shallow-convective organization might have for the albedo in the trade-wind region, it is important to understand how the relationships between cloudiness and shallow-convective organization translate to longer temporal and spatial scales.

Chapter 5

Conclusions

Shallow trade-wind cumuli cover large parts of the worlds oceans and exert an important influence on Earths radiation budget and the atmospheric energy cycle. The uncertain response of shallow cumuli to climate change is a major cause of model spread in predicted climate sensitivity. The diversity of model responses reflects a poor understanding of the factors controlling the strength of shallow-convective mixing. Factors controlling shallow convection do not only pertain to the large-scale meteorological environment, but also to precipitation and the spatial organization of convection, which are modulated by shallow convection itself.

In this thesis we use large-eddy simulation (LES) and ground-based remote sensing observations from the Barbados Cloud Observatory (BCO) to understand how precipitation and the organization of shallow convection into larger and deeper clusters influences the structure of the trade-wind layer and the vertical distribution of cloudiness. Numerical experiments are performed to investigate how the modifications introduced by precipitation and convective organization influences the response of shallow convection to perturbations in the large-scale environment. In the last chapter of the thesis, BCO observations are used to study the statistics of spatial organization as identified by the occurrence of cold pools.

In our large-domain LES representative of conditions in the downstream trades, precipitating shallow convection spontaneously organizes into larger and deeper cloud clusters. While moisture is mixed over a deep layer in the organized clusters, substantial precipitation and compensating subsidence induced by the cluster dries the cloud layer in the surrounding. In the presence of deeper and organized cloud clusters, the domain-average trade-wind layer is much shallower, drier and warmer. Cloud fractions decrease strongly in

the lowest 3.5 km, reducing projected cloud cover and albedo by more than 30% relative to a small-domain control simulation without organization. In the presence of convective organization, the shallow cumulus clouds do not deepen uniformly, but a few large and deep cloud clusters develop that suppress the rest of the cloud field. We find that the broader distribution of cloud-top heights in the presence of organization also implies a broader distribution of detrainment levels, which smooths the humidity structure and weakens the inversion compared to a cloud field with more homogeneously distributed cloud-top heights. The weaker inversion leads to decreased cloud cover because the formation of stratiform outflow layers is inhibited.

In Chapter 2 we also perform idealized climate change experiments with a uniform 4 K warming at constant relative humidity to investigate the influence of precipitation and organization on the warming response. In non-precipitating LES, the stronger surface latent heat flux deepens the cloud layer in the warmer climate, increasing the entrainment drying of the cloud layer and resulting in reduced cloud fractions between 1.5 and 4 km (as in *Rieck et al.* (2012)). Here we show that precipitation and shallow-convective organization limit the deepening and thus the drying of the cloud layer in the warmer climate state. Cloud fractions near cumulus tops nevertheless decrease slightly with warming, because of the weaker inversion and because updrafts become more concentrated. But we find the positive feedback in all cases to be small, especially due to an insensitivity of cloud fractions near cumulus bases to changes in the large-scale environment. Our simulations suggest that the increase of domain size and thus the spatial organization of shallow convection into larger and deeper clusters has a much stronger effect on the trade-wind layer than the 4 K warming.

The deepening of shallow convection is also important to capture the observed shift from less precipitation and more cloud cover in winter, to more precipitation and less cloud cover in summer. In Chapter 3 we show how this shift is reproduced in LES by prescribing a 2 K increase in sea-surface temperature (SST) and a 20% decrease in large-scale subsidence. The SST increase and subsidence decrease deepens maximum cloud-top heights by 4 km, quadruples precipitation, weakens the trade inversion, and reduces cloud cover compared to a more winter-like control simulation. Contrastingly, the shallow trade-wind layer in the winter-like simulation maintains a strong inversion with large cloud fractions near cumulus tops. The large cloud fractions are due to thin stratiform outflow layers, which develop from condensate-detrainment of larger and deeper precipitating cloud clusters. The simulations suggest that precipitation and compensating subsidence from the deeper clusters induce a strong drying above the cloud layer, which locally strengthens the inversion. Furthermore, strong longwave cooling at cloud tops and across sharp moisture gradients is necessary to form and maintain the outflow layers. Hence, once sustained deeper convection substantially weakens the inversion structure, and the vertical profile of

radiative cooling becomes more uniform, the outflow layers cease to develop. This occurs in simulations with stronger winds, additional horizontal advective cooling, and under a drier free troposphere—all of which are perturbations in the large-scale forcings associated with the winter regime. The dominant influence of convective deepening on weakening the inversion and inhibiting stratiform layers is largely independent of the specific forcings and model choices which caused the deepening. Because cloudiness near cumulus bases is relatively constant across the different simulations, the reduction of inversion cloud that occurs when shallow convection deepens suggests a negative relationship between the depth of shallow convection and cloud cover.

In summary, the numerical experiments performed in Chapter 2 and Chapter 3 of this thesis reveal a strong influence of the organization and deepening of precipitating shallow convection on the structure of the trades, which has potentially important implications for the atmospheric energy cycle and the radiation budget. Previous studies have shown that convection further downstream is particularly sensitive to the thermodynamic properties of air it entrains at altitudes near 2 km (*Holloway and Neelin*, 2009; *Nuijens et al.*, 2009). Here we demonstrate that both precipitation and shallow-convective organization reduce the moisture accumulated under the trade inversion—either by precipitating it out, by mixing it over a deeper layer, or by redistributing it to lower levels where it can limit the surface moisture flux. Most of the changes in the cloud profile in response to precipitation, to shallow-convective organization, and to changes in the large-scale environment occur in the upper cloud layer near the trade inversion. Cloud fractions near the base of the cumulus clouds instead are relatively insensitive to the perturbations in the large-scale environment. This is in line with observations at Barbados (*Nuijens et al.*, 2014; 2015a). But in contrast to those climate models that strongly reduce cloudiness near cumulus bases under stronger shallow-convective mixing, and therefore have a high climate sensitivity (*Brient et al.*, 2015).

In the observational component of the thesis (Chapter 4), an analysis of the statistics of spatial organization as identified by cold pools is performed. Cold pools modify the lower troposphere at Barbados on 70% of the days analysed. A comparison of changes before and after the cold-pool front reveals that cold pools with stronger temperature depressions in the cold-pool front also tend to be associated with stronger in-front increases in cloud-top height, higher precipitation frequencies, and stronger surface humidity decreases compared to weaker cold pools. But despite the clouds being deeper, the contribution from cloudiness near cumulus tops to projected cloud cover is lower in the front of stronger cold pools. Humidity in the front and the wake of stronger cold pools is also more homogeneously distributed in the vertical, indicative of stronger shallow-convective mixing and stronger penetrative downdrafts, which dry the lowest layers. Overall, periods of cold pools are very cloudy. Although cloud cover decreases in the cold-pool front after a strong

peak at the cold-pool onset, cloud cover in the cold-pool wake remains strongly enhanced compared to the longterm mean. The observations could be used to study relationships between cold-pool activity and cloud cover on longer timescales, but it will be challenging to control the influence of other cloud-controlling factors in the observations. Overall, the frequent occurrence of cold pools at Barbados manifests the importance of precipitation and shallow-convective organization for the trades.

One important hypothesis emerging from this thesis is that the inversion structure and thus inversion cloudiness at Barbados might be more strongly controlled by deeper convection and precipitation upstream, than by the specific combination of large-scale forcings encountered along the trade-wind trajectory. There are interesting opportunities to test the hypothesis generated by the idealized numerical experiments with observations and in more realistic model setups. New computational capabilities not only render possible the LES performed in this thesis, but also high-resolution simulations for the entire tropical Atlantic with the ICOsahedral Non-hydrostatic (ICON) model (*Zängl et al.*, 2015). These ICON simulations allow to investigate the influence of shallow-convective organization on the trade-wind layer structure in a more realistic setting including disturbances like easterly waves. Furthermore, they can provide a better understanding of the frequency with which specific combinations of large-scale forcings occur. In particular, the LES in this thesis would benefit from better estimates of the magnitude and variability of horizontal advective moistening and cooling tendencies.

The LES performed highlight the insensitivity of cloudiness near the base of the cumulus layer to changes in the large-scale environment. However, cloud fractions in the LES are strongly underestimated compared to the observations at Barbados, and we have to rely on the LES to adequately capture the qualitative relationships between cloudiness and the large-scale environment. This limitation of the LES motivates attempts to observationally constrain the sensitivity of near-base cloud fractions to changes in the large-scale environment and to the organization of shallow convection. During the upcoming EUREC^{4}A field campaign, aircraft observations will be used to infer the convective mass flux at cumulus bases from the sub-cloud layer mass budget (*Bony et al.*, 2017). An initial analysis with my LES shows that the mass flux estimated from the mass budget agrees reasonably well with the mass flux diagnosed directly from the LES (see *Bony et al.* (2017)). A refinement of the estimation method will show whether the method captures the dependency of the mass flux to changes in the large-scale environment and in the convective organization.

In conclusion, the expected perturbations in large-scale meteorology associated with climate change likely favour the deepening and organization of shallow convection. This thesis underlines the important consequences this might have for cloudiness and the thermodynamic structure in the trades.

Appendix

A. Development of Deep Convection in the Absence of Cold Pools

We mentioned in Section 2.5.1 that cold-pool dynamics and moisture-convection feedbacks lead to the organization and deepening of precipitating and non-precipitating shallow convection respectively. Here we explore some factors that might explain why the development of deep convection appears to be so sensitive to domain size. But before doing so, it is worth pointing out that the basic sensitivity to domain size likely reflects the marginal sensitivity of the basic setup. Simulations with interactive radiation, or perhaps with a more realistic profile of imposed warming, may not show similar sensitivities.

Whereas the mean cloud core velocity and mass-flux are initially the same across the simulations on the different domains (not shown), the maximum updraft speed $w_{\max}$ is systematically larger in the large domain simulations from its start, independent of precipitation (Figure 2.8 c). There are two possible explanations for this, (a) updrafts interact differently on the large domain (dynamical argument), or (b) the presence of $16\times$ more updrafts on a sixteen-fold larger domain may allow for a better sampling of the vertical velocity probability density function (pdf), the tail of which is represented by $w_{\max}$ (sampling argument). To test explanation (b) we perform three additional precipitating simulations on the small domain with different random seeds (see Table 2.1 for details). By always picking the maximum $w_{\max}$ out of the four realizations, we construct a $w_{\max}$ timeseries of a composite $25.6\times25.6\,\mathrm{km}^2$ domain simulation which neglects the interaction of updrafts on the four times larger length scale, but better samples the pdf. The timeseries in Figure A.1 (a) shows $w_{\max}$ timeseries of the precipitating simulations on the first half day. A gradual increase of the mean $w_{\max}$ from the small domain cases to the composite $25.6\times25.6\,\mathrm{km}^2$ case, the large domain $51.2\times51.2\,\mathrm{km}^2$ and an even larger $102.4\times102.4\,\mathrm{km}^2$ domain case (Table 2.1) is evident. Note that a running average is applied to smooth

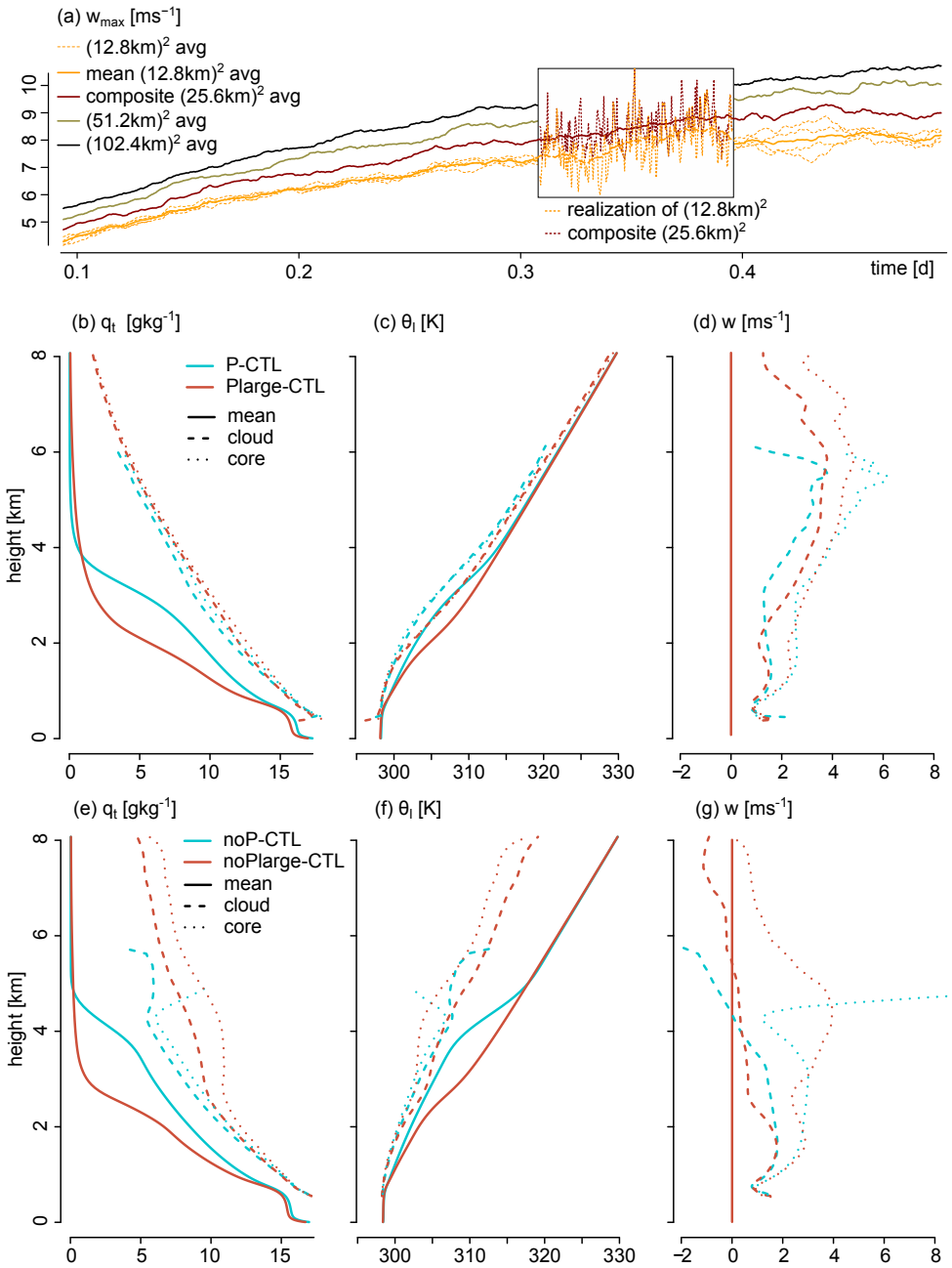

Figure A.1.: (a) Zoom into the maximum updraft speed $w_{\max}$ timeseries of the first half day. Shown are four realizations of the small $(12.8\,\mathrm{km})^2$ domain P-CTL case with different random seeds, their mean, the composite $(25.6\,\mathrm{km})^2$ case representing the maxima of the four small domain realizations, the Plarge-CTL case on the $(51.2\,\mathrm{km})^2$ domain, and a $4\times$ larger $(102.4\,\mathrm{km})^2$ precipitating CTL case. 'avg' stands for timeseries smoothed with a 30 min running average, the timeseries highlighted in the zoom in contain the full temporal variability. (b-g) Domain (solid), cloud (dashed) and core (dotted) averaged profiles of total humidity q_t (b,e), liquid water potential temperature θ_l (c,f), and vertical velocity w (d,g) for the P-CTL and Plarge-CTL (b-d), and the noP-CTL and noPlarge-CTL simulations (e-g).

the timeseries, such that the strong temporal variability of $w_{\max}$ is only evident from the zoom in, showing how the $25.6\times25.6\,\mathrm{km}^2$ case is indeed a composite of the small domain cases. We conclude from this compositing test that it is the better sampling of the vertical velocity pdf which initially leads to larger $w_{\max}$ on a larger domain.

Bjerknes (1938) presented a simple theoretical framework for explaining the narrowness of saturated cumulus updrafts ascending through a dry-adiabatically subsiding environment (see also *Randall* (2012) for a similar derivation as follows). It may help understand why on larger domains an individual updraft can increase its buoyancy more effectively than on a small domain, where updrafts experience more competition.

Assuming that the updraft speed w_c scales with buoyancy as follows:

$$w_\mathrm{c} \sim B \sim \frac{\partial}{\partial t}\left(T_\mathrm{c} - \widetilde{T}\right), \tag{A.1}$$

where B is the buoyancy, the subscript $(\ )_\mathrm{c}$ represents cloudy and $\widetilde{(\ )}$ represents clear ambient conditions (Figure 2.8 shows how closely the $w_{\max}$ and the maximum cloud top timeseries are related, especially from about 1.2 days on). The rate of change of cloud temperature depends on the cooling experienced by the vertical ascent and the heating through condensation

$$\frac{\partial}{\partial t}T_\mathrm{c} = w_\mathrm{c}\left(\Gamma - \Gamma_\mathrm{m}\right), \tag{A.2}$$

with $\Gamma = -\dfrac{\partial T}{\partial z}$ being the background lapse rate and Γ_m the moist adiabatic lapse rate. In a clear region, the induced subsiding motion increases the temperature by working against the background stratification by

$$\frac{\partial}{\partial t}\widetilde{T} = \widetilde{w}\left(\Gamma - \Gamma_\mathrm{d}\right), \tag{A.3}$$

where Γ_d is the dry adiabatic lapse rate and $\widetilde{w} < 0$. Satisfying the constraint in LES that

$$\sigma_\mathrm{c} w_\mathrm{c} + \left(1 - \sigma_\mathrm{c}\right)\widetilde{w} = 0 \tag{A.4}$$

(σ_c is the fractional area covered by updrafts), the rate at which updrafts gain buoyancy can be written as

$$\frac{\partial}{\partial t}\left(T_\mathrm{c}-\widetilde{T}\right)=w_\mathrm{c}\left(\Gamma-\Gamma_\mathrm{m}\right)-\widetilde{w}\left(\Gamma-\Gamma_\mathrm{d}\right)=\frac{w_\mathrm{c}}{1-\sigma_\mathrm{c}}\left[\Gamma-\Gamma_\mathrm{m}-\sigma_\mathrm{c}\left(\Gamma_\mathrm{d}-\Gamma_\mathrm{m}\right)\right]. \tag{A.5}$$

In case of conditional instability ($\Gamma-\Gamma_\mathrm{m}>0$ and $\Gamma-\Gamma_\mathrm{d}<0$), updrafts can gain more buoyancy with larger w_c or weaker $\widetilde{w}$, both of which can be achieved for $\sigma_\mathrm{c}\to 0$, that is, by making the updraft narrow and the clear neighboring subsiding regions broad. Through this mechanism, updrafts of a given area may develop greater buoyancy on a larger domain, as their compensating subsidence will be spread over a larger area.

Concerning the deepening of convection in the absence of precipitation and cold-pool dynamics, moisture-convection feedbacks (*Bretherton et al.*, 2005) appear to play a role. Figure A.1 (b-g) show profiles of cloud-averaged (non-zero liquid water) and cloud core-averaged (non-zero liquid water and positively buoyant compared to slab-average) fields. Although the mean trade-wind layers are drier, the cloud and core-averaged profiles in the large-domain cases are moister than in the respective small domain cases. The differences are particularly strong in noPlarge-CTL, which shows very moist cloud and core-averaged profiles above 2.5 km. Snapshots of the humidity fields in the sub-cloud and cloud layer (Figure A.2) show that moist cloud layers are collocated with moist sub-cloud layers in noPlarge-CTL. Contrastingly, in Plarge-CTL, cold pools are dry pools located below an anomalously moist cloud layer where convection occurred earlier. Note that while moisture-convection feedbacks strengthen, the strong liquid water loading in noPlarge-CTL likely puts an upper limit to the deepening of convection. The strong liquid water loading manifests itself both in the reduced θ_l compared to the mean (Figure A.1 f) and in the reduced core-averaged vertical velocity above about 4.5 km (Figure A.1 d, g).

In summary, in the absence of cold pools (and wind shear), moist regions overlap more favorably and, via entrainment, promote the deepening of convection through positive moisture-convection feedbacks.

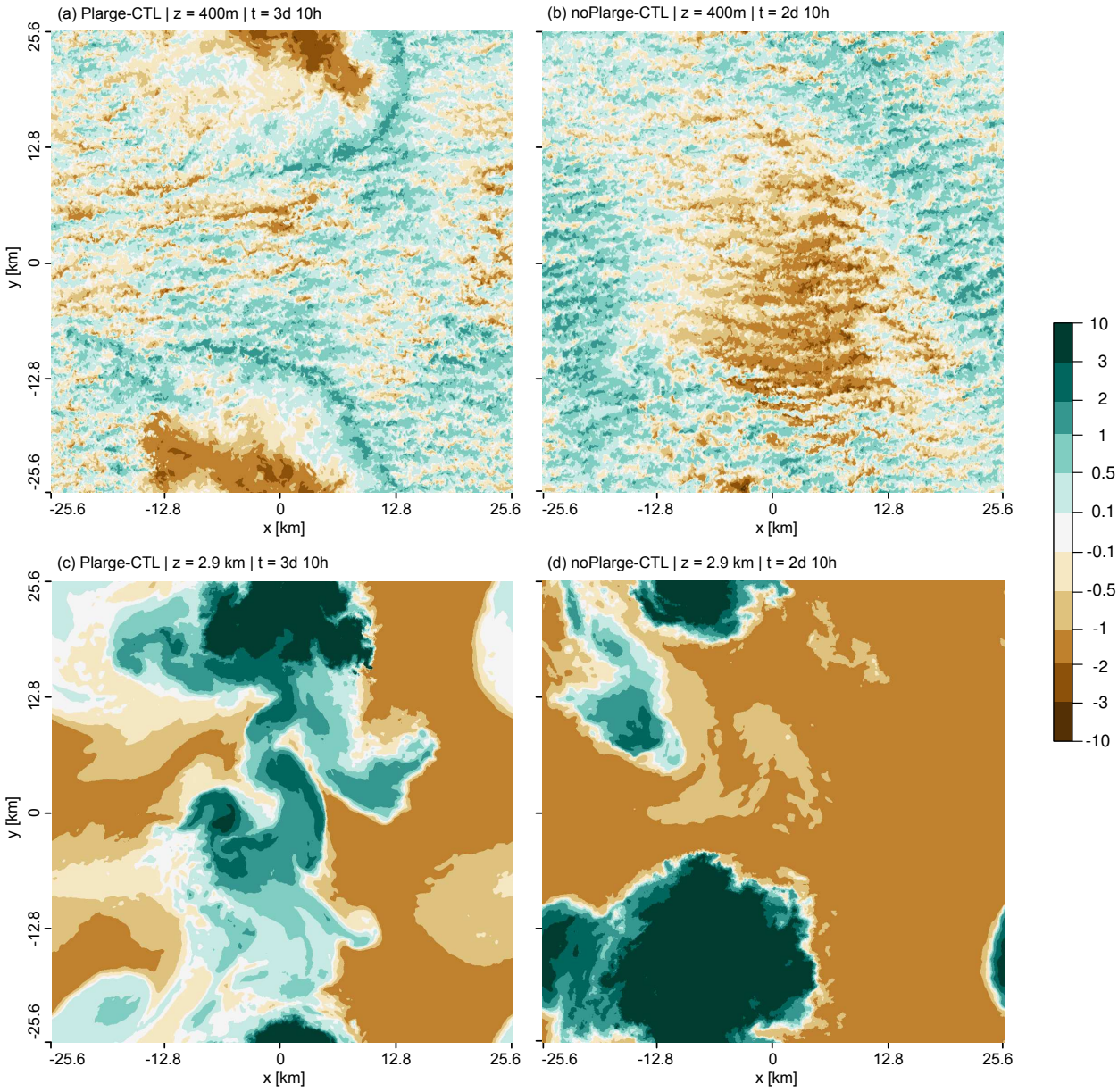

Figure A.2.: Snapshots of anomalies of total humidity q_t [in $g\,kg^{-1}$] at 400 m (a and b) and 2.9 km (c and d) for Plarge-CTL (left) and noPlarge-CTL (right). The snapshots correspond to the cloud fields in Fig. 2.9d-e respectively.

B. Robustness and uncertainties of LES studies[1]

There is a tendency to view LES as surrogate of the truth, as able to fully represent the observed characteristics of the marine boundary layer. Simulated vertical distributions of cloud fraction and, to a slightly lesser extent, of projected cloud cover tend to show relatively good agreement across different LES models in the BOMEX and RICO intercomparison cases of typical shallow trade-wind cumulus conditions (*Siebesma et al.*, 2003; *VanZanten et al.*, 2011). Also an intercomparison case of the diurnal cycle of shallow cumulus over land shows good model-to-model agreement (*Brown et al.*, 2002). The cloud distributions of the above three intercomparison cases show a strong peak in cloud fraction at cloud base, a rapid decrease in cloud fraction above cloud base, and relatively small cloud fractions near the tops of cumulus clouds under the trade inversion. Total cloud cover ranges between about 13±6% for BOMEX (*Siebesma et al.*, 2003) and 19±9% for RICO (*VanZanten et al.*, 2011), with the simulated cloud cover for RICO comparing favorably with corresponding lidar data. In simulations of an intermediate regime between stratocumulus and trade-wind cumulus, representative for the ATEX field campaign and marked by a stronger inversion, the vertical distribution of cloud fraction has its maximum near the inversion instead of near cloud base (*Stevens et al.*, 2001). In this ATEX intercomparison case, there is much larger spread in simulated total cloud cover among the participating LES (total cloud cover ranges between 20% and 80% (mean$\pm 2\sigma$)), with the spread related to the representation of stratiform cloud amount under the inversion (*Stevens et al.*, 2001). Also the CGILS intercomparison case of the response of shallow cumulus to climate change perturbations (location S6) shows the most apparent differences in the simulated cloud fraction pro

le near the top of the cloud layer under the trade-inversion (*Blossey et al.*, 2013). Whereas stratiform outflow layers are observed frequently at Barbados (*Nuijens et al.*, 2014; 2015b), LES apparently has difficulties to properly simulate detrained layers of stratiform cloud. This difficulty is likely related to a poor representation of tight feedbacks between such outflow layers with radiation and subsidence, and to very high vertical resolutions necessary to resolve sharp inversions (*Stevens et al.*, 2001). On the other hand, the range of cloud-base cloud fractions instead is quite consistent among the various intercomparison cases, with intermodel differences lying in the narrow range of about 4.5% to 8% (*Brown*, 1999; *Stevens et al.*, 2001; *Siebesma et al.*, 2003; *VanZanten et al.*, 2011; *Blossey et al.*, 2013)

The comparison of the cumulative cloud fraction—the cumulative contributions to total cloud cover from the top down to the bottom of the cloud layer—estimated from LES and

[1]The material in Appendix B is an excerpt of Vial, J., S. Bony, B. Stevens, and R. Vogel (2017), Mechanisms and model diversity of trade-wind shallow cumulus cloud feedbacks: A review, *Surveys in Geophysics*, doi:10.1007/s10712-017-9418-2.

measured by a lidar indicates that the LES may not represent the full spectrum of cloud top height distributions present in nature (Figure 7 of *VanZanten et al.* (2011)). LES on large domains of $50\times50\,\mathrm{km}^2$ (about 16-times to 32-times larger than the domain sizes used for the intercomparison cases) can represent cloud populations with a wide range of cloud top heights, but cloud fractions in the upper cloud layer tend to be underestimated (see Chapter 2 and Chapter 3). This underestimation is likely due to numerical diffusion, which is strongly related to the choice of advection scheme, the subgrid-scale model and the grid spacing. A thorough investigation of the impact of such model choices showed that cloud cover strongly decreased when a more dissipative monotone advection scheme was used instead of a centered differences scheme, or when a more dissipative subgrid formulation was used (relative decreases of cloud cover of up to 30%) (*Matheou et al.*, 2011). *Matheou et al.* (2011) also find a relative decrease of cloud cover of up to 70% when the uniform horizontal and vertical grid spacing is increased from 20 m to 80 m. These results are in qualitative agreement with sensitivity studies presented in *Stevens et al.* (2001) and *Siebesma et al.* (2003), and show that one has to be careful when comparing absolute values of cloud cover between different LES studies, and between LES and observations. The strong decrease in cloud cover with larger grid spacing in *Matheou et al.* (2011) is partly due to reductions in cloudiness under the inversion, which cannot be resolved well at a vertical grid spacing of 80 m (see the liquid water specific humidities in their Figure 11). This again highlights that cloudiness near the top of shallow cumulus under the trade-inversion is still only poorly constrained by LES.

Bibliography

Albrecht, B. A. (1993), Effects of precipitation on the thermodynamic structure of the trade wind boundary layer, *J. Geophys. Res.*, *98*(D4), 7327–7337, doi: 10.1029/93JD00027.

Augstein, E., H. Riehl, F. Ostapoff, and V. Wagner (1973), Mass and Energy Transports in an Undisturbed Atlantic Trade-Wind flow, *Monthly Weather Review*, *101*(2), 101–111.

Barnes, G. M., and M. Garstang (1982), Subcloud layer energetics of precipitating convection, *Mon. Wea. Rev.*, *110*(2), 102–117.

Beard, K. V., and H. T. Ochs (1993), Warm-rain initiation: An overview of microphysical mechanisms, *Journal of Applied Meteorology*, *32*(4), 608–625, doi:10.1175/1520-0450(1993)032¡0608:WRIAOO¿2.0.CO;2.

Bellon, G., and O. Geoffroy (2016), Stratocumulus radiative effect, multiple equilibria of the well-mixed boundary layer and transition to shallow convection, *Quart. J. Roy.Meteor.Soc.*, pp. n/a–n/a, doi:10.1002/qj.2762.

Bellon, G., and B. Stevens (2012), Using the sensitivity of large-eddy simulations to evaluate atmospheric boundary layer models, *J. Atmos. Sci.*, *69*(5), 1582–1601, doi: 10.1175/JAS-D-11-0160.1.

Betts, A., and W. Ridgeway (1989), Climatic equilibrium of the atmospheric convective boundary layer over a tropical ocean, *J. Atmos. Sci.*, *46*, 2621–2641.

Betts, A. K. (1973), Non-precipitating cumulus convection and its parameterization, *Quart. J. Roy.Meteor.Soc.*, *99*(419), 178–196, doi:10.1002/qj.49709941915.

Betts, A. K., and B. A. Albrecht (1987), Conserved variable analysis of the convective boundary layer thermodynamic structure over the tropical oceans, *J. Atmos. Sci.*, *44*(1), 83–99.

Bjerknes, J. (1938), Saturated-adiabatic ascent of air through dry-adiabatically descending environment, *Quart. J. Roy.Meteor.Soc.*, *64*, 325–330.

Blossey, P. N., C. S. Bretherton, M. Zhang, A. Cheng, S. Endo, T. Heus, Y. Liu, A. P. Lock, S. R. de Roode, and K.-M. Xu (2013), Marine low cloud sensitivity to an idealized climate change: The CGILS LES intercomparison, *J. Adv. Model. Earth Syst.*, *5*(2), 234–258, doi:10.1002/jame.20025.

Blyth, A. M., J. H. Lowenstein, Y. Huang, Z. Cui, S. Davies, and K. S. Carslaw (2013), The production of warm rain in shallow maritime cumulus clouds, *Quarterly Journal of the Royal Meteorological Society*, *139*(670), 20–31, doi:10.1002/qj.1972.

Böing, S. J., H. J. J. Jonker, A. P. Siebesma, and W. W. Grabowski (2012), Influence of the Subcloud Layer on the Development of a Deep Convective Ensemble, *J. Atmos. Sci.*, *69*(9), 2682–2698, doi:10.1175/JAS-D-11-0317.1.

Bony, S., and J.-L. Dufresne (2005), Marine boundary layer clouds at the heart of tropical cloud feedback uncertainties in climate models, *Geophys. Res. Lett.*, *32*(20), L20,806, doi:10.1029/2005GL023851.

Bony, S., J.-L. Dufresne, H. Le Treut, J.-J. Morcrette, and C. Senior (2004), On dynamic and thermodynamic components of cloud changes, *Clim. Dyn.*, *22*(2-3), 71–86.

Bony, S., B. Stevens, F. Ament, S. Bigorre, P. Chazette, S. Crewell, J. Delanoë, K. Emanuel, D. Farrell, C. Flamant, S. Gross, L. Hirsch, J. Karstensen, B. Mayer, L. Nuijens, J. H. Ruppert, I. Sandu, P. Siebesma, S. Speich, F. Szczap, J. Totems, R. Vogel, M. Wendisch, and M. Wirth (2017), Eurec4a: A field campaign to elucidate the couplings between clouds, convection and circulation, *Surveys in Geophysics*, doi:10.1007/s10712-017-9428-0.

Boucher, O., D. Randall, P. Artaxo, C. Bretherton, G. Feingold, P. Forster, V.-M. Kerminen, Y. Kondo, H. Liao, U. Lohmann, P. Rasch, S. Satheesh, S. Sherwood, B. Stevens, and X. Zhang (2013), *Clouds and Aerosols*, book section 7, pp. 571–658, Cambridge University Press, Cambridge, United Kingdom and New York, NY, USA, doi:10.1017/CBO9781107415324.016.

Bretherton, C. S., and P. N. Blossey (2014), Low cloud reduction in a greenhouse-warmed climate: Results from lagrangian les of a subtropical marine cloudiness transition, *J. Adv. Model. Earth Syst.*, *6*(1), 91–114, doi:10.1002/2013MS000250.

Bretherton, C. S., and P. N. Blossey (2017), Understanding mesoscale aggregation of shallow cumulus convection using large-eddy simulation, *J. Adv. Model. Earth Syst.*, pp. n/a–n/a, doi:10.1002/2017MS000981.

Bretherton, C. S., M. E. Peters, and L. E. Back (2004), Relationships between water vapor path and precipitation over the tropical oceans, *J. Climate*, *17*(7), 1517–1528, doi:10.1175/1520-0442(2004)017¡1517:RBWVPA¿2.0.CO;2.

Bretherton, C. S., P. N. Blossey, and M. Khairoutdinov (2005), An energy-balance analysis of deep convective self-aggregation above uniform sst, *J. Atmos. Sci.*, *62*(12), 4273–4292, doi:10.1175/JAS3614.1.

Bretherton, C. S., P. N. Blossey, and C. R. Jones (2013), Mechanisms of marine low cloud sensitivity to idealized climate perturbations: A single-LES exploration extending the CGILS cases, *J. Adv. Model. Earth Syst.*, *5*(2), 316–337, doi:10.1002/jame.20019.

Brient, F., and T. Schneider (2016), Constraints on climate sensitivity from space-based measurements of low-cloud reflection, *J. Climate*, *29*(16), 5821–5835.

Brient, F., T. Schneider, Z. Tan, S. Bony, X. Qu, and A. Hall (2015), Shallowness of tropical low clouds as a predictor of climate models response to warming, *Clim. Dyn.*, pp. 1–17, doi:10.1007/s00382-015-2846-0.

Brown, A. R. (1999), Large-eddy simulation and parametrization of the effects of shear on shallow cumulus convection, *Boundary-Layer Meteorology*, *91*(1), 65–80, doi:10.1023/A:1001836612775.

Brown, A. R., R. T. Cederwall, A. Chlond, P. G. Duynkerke, J.-C. Golaz, M. Khairoutdinov, D. C. Lewellen, A. P. Lock, M. K. MacVean, C.-H. Moeng, R. A. J. Neggers, A. P. Siebesma, and B. Stevens (2002), Large-eddy simulation of the diurnal cycle of shallow cumulus convection over land, *Quart. J. Roy.Meteor.Soc.*, *128*(582), 1075–1093, doi:10.1256/003590002320373210.

Brueck, M., L. Nuijens, and B. Stevens (2015), On the seasonal and synoptic time-scale variability of the north atlantic trade wind region and its low-level clouds, *J. Atmos. Sci.*, *72*(4), 1428–1446, doi:10.1175/JAS-D-14-0054.1.

Burdanowitz, J., L. Nuijens, B. Stevens, and C. Klepp (2015), Evaluating Light Rain from Satellite- and Ground-Based Remote Sensing Data over the Subtropical North Atlantic, *J. Appl. Meteor. Climatol.*, *54*(3), 556–572, doi:10.1175/JAMC-D-14-0146.1.

Byers, H. R., and R. K. Hall (1955), A census of cumulus-cloud height versus precipitation in the vicinity of Puerto Rico during the winter and spring of 1953-1954, doi:10.1175/1520-0469(1955)012¡0176:ACOCCH¿2.0.CO;2.

de Szoeke, S. P., E. D. Skyllingstad, P. Zuidema, and A. S. Chandra (2017), Cold pools and their influence on the tropical marine boundary layer, *J. Atmos. Sci.*, *74*(4), 1149–1168, doi:10.1175/JAS-D-16-0264.1.

Emanuel, K., A. A. Wing, and E. M. Vincent (2014), Radiative-convective instability, *J. Adv. Model. Earth Syst.*, *6*(1), 75–90, doi:10.1002/2013MS000270.

Feng, Z., S. Hagos, A. K. Rowe, C. D. Burleyson, M. N. Martini, and S. P. Szoeke (2015), Mechanisms of convective cloud organization by cold pools over tropical warm ocean during the amie/dynamo field campaign, *J. Adv. Model. Earth Syst.*, *7*(2), 357–381.

Fermepin, S., and S. Bony (2014), Influence of low-cloud radiative effects on tropical circulation and precipitation, *J. Adv. Model. Earth Syst.*, *6*(3), 513–526, doi: 10.1002/2013MS000288.

Fu, Q., and K. N. Liou (1992), On the correlated k-distribution method for radiative transfer in nonhomogeneous atmospheres, *J. Atmos. Sci.*, *49*, 2139–2156.

Holland, J. Z., and E. M. Rasmusson (1973), Measurements of the Atmospheric Mass , Energy , and Momentum Budgets Over a 500-Kilometer Square of Tropical Ocean, *Mon. Wea. Rev.*, *101*(1), 44–57.

Holloway, C. E., and J. D. Neelin (2009), Moisture Vertical Structure, Column Water Vapor, and Tropical Deep Convection, *J. Atmos. Sci.*, *66*(6), 1665–1683, doi: 10.1175/2008JAS2806.1.

Jeevanjee, N., and D. M. Romps (2013), Convective self-aggregation, cold pools, and domain size, *Geophys. Res. Lett.*, *40*(5), 994–998, doi:10.1002/grl.50204.

Jiang, H., G. Feingold, and A. Sorooshian (2010), Effect of aerosol on the susceptibility and efficiency of precipitation in warm trade cumulus clouds, *J. Atmos. Sci.*, *67*(11), 3525–3540, doi:10.1175/2010JAS3484.1.

Khairoutdinov, M., and D. Randall (2006), High-Resolution Simulation of Shallow-to-Deep Convection Transition over Land, *J. Atmos. Sci.*, *63*(12), 3421–3436, doi: 10.1175/JAS3810.1.

Klein, S. A. (1997), Synoptic Variability of Low-Cloud Properties and Meteorological Parameters in the Subtropical Trade Wind Boundary Layer, *J. Climate*, *10*, 2018–2039.

Klein, S. A., and D. L. Hartmann (1993), The seasonal cycle of low stratiform clouds, *J. Climate*, *6*(8), 1587–1606, doi:10.1175/1520-0442(1993)006¡1587:TSCOLS¿2.0.CO;2.

Knight, C. A., and L. J. Miller (1998), Early radar echoes from small, warm cumulus: Bragg and hydrometeor scattering, *J. Atmos. Sci.*, *55*(18), 2974–2992, doi: 10.1175/1520-0469(1998)055¡2974:EREFSW¿2.0.CO;2.

Kuang, Z., and C. S. Bretherton (2006), A mass flux scheme view of a high-resolution simulation of transition from shallow to deep cumulus convection, *J. Atmos. Sci.*, *63*, 1895–1909.

Kubar, T. L., D. L. Hartmann, and R. Wood (2009), Understanding the importance of microphysics and macrophysics for warm rain in marine low clouds. part i: Satellite observations, *Journal of the Atmospheric Sciences*, *66*(10), 2953–2972, doi: 10.1175/2009JAS3071.1.

Lamer, K., P. Kollias, and L. Nuijens (2015), Observations of the variability of shallow trade wind cumulus cloudiness and mass flux, *Journal of Geophysical Research: Atmospheres*, *120*(12), 6161–6178, doi:10.1002/2014JD022950.

Langhans, W., and D. M. Romps (2015), The origin of water vapor rings in tropical oceanic cold pools, *Geophysical Research Letters*, *42*(18), 7825–7834.

Li, Z., P. Zuidema, P. Zhu, and H. Morrison (2015), The sensitivity of simulated shallow cumulus convection and cold pools to microphysics, *J. Atmos. Sci.*, *72*(9), 3340–3355, doi:10.1175/JAS-D-14-0099.1.

Lonitz, K., B. Stevens, and A. Horváth (2014), Susceptibility of trade wind cumulus clouds to precipitation, Ph.D. thesis, Universität Hamburg Hamburg.

Malkus, J. S. (1954), Some results of a trade-cumulus cloud investigation, *Journal of Meteorology*, *11*(3), 220–237, doi:10.1175/1520-0469(1954)011¡0220:SROATC¿2.0.CO;2.

Malkus, J. S. (1956), On the maintenance of the trade winds, *Tellus*, *8*(3), 335–350, doi: 10.3402/tellusa.v8i3.9015.

Malkus, J. S. (1958), On the structure of the trade wind moist layer, *Papers in physical oceanography and meteorology*, *13*(2), 1–47.

Matheou, G., D. Chung, L. Nuijens, B. Stevens, and J. Teixeira (2011), On the Fidelity of Large-Eddy Simulation of Shallow Precipitating Cumulus Convection, *Mon. Wea. Rev.*, *139*(9), 2918–2939, doi:10.1175/2011MWR3599.1.

Medeiros, B., and L. Nuijens (2016), Clouds at barbados are representative of clouds across the trade wind regions in observations and climate models, *Proceedings of the National Academy of Sciences*, *113*(22), E3062–E3070, doi:10.1073/pnas.1521494113.

Muller, C., and S. Bony (2015), What favors convective aggregation and why?, *Geophys. Res. Lett.*, *42*(13), 5626–5634, doi:10.1002/2015GL064260.

Muller, C. J., and I. M. Held (2012), Detailed investigation of the self-aggregation of convection in cloud-resolving simulations, *J. Atmos. Sci.*, *69*(8), 2551–2565, doi: 10.1175/JAS-D-11-0257.1.

Myers, T. A., and J. R. Norris (2013), Observational evidence that enhanced subsidence reduces subtropical marine boundary layer cloudiness, *J. Climate*, *26*(19), 7507–7524.

Neggers, R., B. Stevens, and J. D. Neelin (2006), A simple equilibrium model for shallow-cumulus-topped mixed layers, *Theor. and Comp. Fluid. Dyn.*, *20*(5-6), 305–322, doi: 10.1007/s00162-006-0030-1.

Nitta, T., and S. Esbensen (1974), Heat and moisture budget analyses using BOMEX data, *Mon. Wea. Rev.*, *102*, 17–28.

Nuijens, L., and B. Stevens (2012), The Influence of Wind Speed on Shallow Marine Cumulus Convection, *J. Atmos. Sci.*, *69*(1), 168–184, doi:10.1175/JAS-D-11-02.1.

Nuijens, L., B. Stevens, and A. P. Siebesma (2009), The environment of precipitating shallow cumulus convection, *J. Atmos. Sci.*, *66*, 1962–1979.

Nuijens, L., I. Serikov, L. Hirsch, K. Lonitz, and B. Stevens (2014), The distribution and variability of low-level cloud in the north atlantic trades, *Quart. J. Roy.Meteor.Soc.*, *140*(684), 2364–2374, doi:10.1002/qj.2307.

Nuijens, L., B. Medeiros, I. Sandu, and M. Ahlgrimm (2015a), Observed and modeled patterns of covariability between low-level cloudiness and the structure of the trade-wind layer, *J. Adv. Model. Earth Syst.*, *7*(4), 1741–1764, doi:10.1002/2015MS000483.

Nuijens, L., B. Medeiros, I. Sandu, and M. Ahlgrimm (2015b), The behavior of trade-wind cloudiness in observations and models: The major cloud components and their variability, *J. Adv. Model. Earth Syst.*, *7*(2), 600–616, doi:10.1002/2014MS000390.

Nuijens, L., K. Emanuel, H. Masunaga, and T. L'Ecuyer (2017), Implications of warm rain in shallow cumulus and congestus clouds for large-scale circulations, *Surveys in Geophysics*, doi:10.1007/s10712-017-9429-z.

Pincus, R., and B. Stevens (2009), Monte carlo spectral integration: a consistent approximation for radiative transfer in large eddy simulations, *J. Adv. Model. Earth Syst.*, *1*(2), n/a–n/a, doi:10.3894/JAMES.2009.1.1.

Prospero, J. M., and P. J. Lamb (2003), African droughts and dust transport to the caribbean: Climate change implications, *Science*, *302*(5647), 1024–1027, doi: 10.1126/science.1089915.

Randall, D. A. (2012), Why are cumulus updrafts narrow?, *http://kiwi.atmos.colostate.edu/group/dave/at745/Cumulus_Updrafts_Narrow.pdf*, accessed on 2015-09-21.

Rauber, R. M., H. T. Ochs, L. D. Girolamo, S. Göke, E. Snodgrass, B. Stevens, C. Knight, J. B. Jensen, D. H. Lenschow, R. A. Rilling, D. C. Rogers, J. L. Stith, B. A. Albrecht, P. Zuidema, A. M. Blyth, C. W. Fairall, W. A. Brewer, S. Tucker, S. G. Lasher-Trapp, O. L. Mayol-Bracero, G. Vali, B. Geerts, J. R. Anderson, B. A. Baker, R. P. Lawson, A. R. Bandy, D. C. Thornton, E. Burnet, J.-L. Brenguier, L. Gomes, P. R. A. Brown, P. Chuang, W. R. Cotton, H. Gerber, B. G. Heikes, J. G. Hudson, P. Kollias, S. K. Krueger, L. Nuijens, D. W. O'Sullivan, A. P. Siebesma, and C. H. Twohy (2007), Rain in Shallow Cumulus Over the Ocean: The RICO Campaign, *Bull. Amer. Meteor. Soc.*, *88*(12), 1912–1928, doi:10.1175/BAMS-88-12-1912.

Raymond, D. J., and X. Zeng (2005), Modelling tropical atmospheric convection in the context of the weak temperature gradient approximation, *Quart. J. Roy.Meteor.Soc.*, *131*(608), 1301–1320, doi:10.1256/qj.03.97.

Rieck, M., L. Nuijens, and B. Stevens (2012), Marine Boundary Layer Cloud Feedbacks in a Constant Relative Humidity Atmosphere, *J. Atmos. Sci.*, *69*(8), 2538–2550, doi:10.1175/JAS-D-11-0203.1.

Riehl, H., and J. S. Malkus (1957), On the heat balance and maintenance of circulation in the trades, *Quart. J. Roy.Meteor.Soc.*, *83*(355), 21–29.

Riehl, H., T. Yeh, J. S. Malkus, and N. E. La Seur (1951), The north-east trade of the pacific ocean, *Quart. J. Roy.Meteor.Soc.*, *77*(334), 598–626.

Sandu, I., and B. Stevens (2011), On the factors modulating the stratocumulus to cumulus transitions, *J. Atmos. Sci.*, *68*(9), 1865–1881.

Savic-Jovcic, V., and B. Stevens (2008), The structure and mesoscale organization of precipitating stratocumulus, *J. Atmos. Sci.*, *65*(5), 1587–1605, doi:10.1175/2007JAS2456.1.

Schlemmer, L., and C. Hohenegger (2014), The Formation of Wider and Deeper Clouds as a Result of Cold-Pool Dynamics, *J. Atmos. Sci.*, *71*(8), 2842–2858, doi:10.1175/JAS-D-13-0170.1.

Schlemmer, L., C. Hohenegger, J. Schmidli, C. S. Bretherton, and C. Schr (2011), An idealized cloud-resolving framework for the study of midlatitude diurnal convection over land, *J. Atmos. Sci.*, *68*(5), 1041–1057, doi:10.1175/2010JAS3640.1.

Seifert, A., and K. D. Beheng (2001), A double-moment parameterization for simulating autoconversion, accretion and selfcollection, *Atmos. Res.*, *59–60*, 265–281.

Seifert, A., and K. D. Beheng (2006), A two-moment cloud microphysics parameterization for mixed-phase clouds. part 1: Model description, *Meteorology and Atmospheric Physics*, *92*(1-2), 45–66, doi:10.1007/s00703-005-0112-4.

Seifert, A., and T. Heus (2013), Large-eddy simulation of organized precipitating trade wind cumulus clouds, *Atmos. Chem. Phys.*, *13*(11), 5631–5645, doi:10.5194/acp-13-5631-2013.

Seifert, A., T. Heus, R. Pincus, and B. Stevens (2015), Large-eddy simulation of the transient and near-equilibrium behavior of precipitating shallow convection, *J. Adv. Model. Earth Syst.*, *7*(4), 1918–1937, doi:10.1002/2015MS000489.

Sherwood, S. C., S. Bony, and J.-L. Dufresne (2014), Spread in model climate sensitivity traced to atmospheric convective mixing, *Nature*, *505*(7481), 37–42, doi:10.1038/nature12829.

Short, D. A., and K. Nakamura (2000), TRMM radar observations of shallow precipitation over the tropical oceans, *J. Climate*, *13*(23), 4107–4124, doi:10.1175/1520-0442(2000)013¡4107:TROOSP¿2.0.CO;2.

Siebert, H., M. Beals, J. Bethke, E. Bierwirth, T. Conrath, K. Dieckmann, F. Ditas, A. Ehrlich, D. Farrell, S. Hartmann, M. A. Izaguirre, J. Katzwinkel, L. Nuijens, G. Roberts, M. Schäfer, R. A. Shaw, T. Schmeissner, I. Serikov, B. Stevens, F. Stratmann, B. Wehner, M. Wendisch, F. Werner, and H. Wex (2013), The fine-scale structure of the trade wind cumuli over Barbados—an introduction to the CARRIBA project, *Atmos. Chem. Phys.*, *13*(19), 10,061–10,077, doi:10.5194/acp-13-10061-2013.

Siebesma, A., and J. Cuijpers (1995), Evaluation of parametric assumptions for shallow cumulus convection, *J. Atmos. Sci.*, *52*(6), 650–666.

Siebesma, A. P., C. S. Bretherton, A. Brown, A. Chlond, J. Cuxart, P. G. Duynkerke, H. Jiang, M. Khairoutdinov, D. Lewellen, C.-H. Moeng, E. Sanchez, B. Stevens, and D. E. Stevens (2003), A Large Eddy Simulation Intercomparison Study of Shallow Cumulus Convection, *J. Atmos. Sci.*, *60*(10), 1201–1219, doi:10.1175/1520-0469(2003)60¡1201:ALESIS¿2.0.CO;2.

Snodgrass, E. R., L. Di Girolamo, and R. M. Rauber (2009), Precipitation Characteristics of Trade Wind Clouds during RICO Derived from Radar, Satellite, and Aircraft Measurements, *J. Appl. Meteor. Climatol.*, *48*, 464–483.

Sobel, A. H., and C. S. Bretherton (2000), Modeling tropical precipitation in a single column, *J. Climate*, *13*(24), 4378–4392, doi:10.1175/1520-0442(2000)013¡4378:MTPIAS¿2.0.CO;2.

Stevens, B. (2007), On the growth of layers of nonprecipitating cumulus convection, *J. Atmos. Sci.*, *64*(8), 2916–2931, doi:10.1175/JAS3983.1.

Stevens, B., and A. Seifert (2008), Understanding macrophysical outcomes of microphysical choices in simulations of shallow cumulus convection, *J. Meteorol. Soc. Japan*, *86A*, 143–162, doi:10.2151/jmsj.86A.143.

Stevens, B., A. S. Ackerman, B. A. Albrecht, A. R. Brown, A. Chlond, J. Cuxart, P. G. Duynkerke, D. C. Lewellen, M. K. Macvean, R. A. J. Neggers, E. Snchez, A. P. Siebesma, and D. E. Stevens (2001), Simulations of Trade Wind Cumuli under a Strong Inversion, *J. Atmos. Sci.*, *58*(14), 1870–1891, doi:10.1175/1520-0469(2001)058¡1870:SOTWCU¿2.0.CO;2.

Stevens, B., C.-H. Moeng, A. Ackerman, C. Bretherton, A. Chlond, S. de Roode, J. Edwards, J.-C. Golaz, H. Jiang, M. Khairoutdinov, M. Kirkpatrick, D. Lewellen, A. Lock, F. Müller, D. Stevens, E. Whelan, and P. Zhu (2005), Evaluation of Large-Eddy Simulations via Observations of Nocturnal Marine Stratocumulus, *Mon. Wea. Rev.*, *133*(6), 1443–1462, doi:10.1175/MWR2930.1.

Stevens, B., D. Farrell, L. Hirsch, F. Jansen, L. Nuijens, I. Serikov, B. Brügmann, M. Forde, H. Linne, K. Lonitz, and J. M. Prospero (2016), The Barbados Cloud Observatory – Anchoring Investigations of Clouds and Circulation on the Edge of the ITCZ, *Bull. Amer. Meteor. Soc.*, *0*(0), null, doi:10.1175/BAMS-D-14-00247.1.

Tan, Z., T. Schneider, J. Teixeira, and K. G. Pressel (2016), Large-eddy simulation of subtropical cloud-topped boundary layers: 2. cloud response to climate change, *J. Adv. Model. Earth Syst.*, pp. n/a–n/a, doi:10.1002/2016MS000804.

Tiedtke, M. (1989), A comprehensive mass flux scheme for cumulus parameterization in large-scale models, *Mon. Wea. Rev.*, *117*, 1779–1800.

Tobin, I., S. Bony, and R. Roca (2012), Observational evidence for relationships between the degree of aggregation of deep convection, water vapor, surface fluxes, and radiation, *J. Climate*, *25*(20), 6885–6904, doi:10.1175/JCLI-D-11-00258.1.

Tompkins, A. M. (2001), Organization of Tropical Convection in Low Vertical Wind Shears: The Role of Cold Pools, *J. Atmos. Sci.*, *58*(6), 1650–1672, doi:10.1175/1520-0469(2001)058¡0529:OOTCIL¿2.0.CO;2.

Torri, G., and Z. Kuang (2016), Rain evaporation and moist patches in tropical boundary layers, *Geophys. Res. Lett.*, *43*(18), 9895–9902.

Torri, G., Z. Kuang, and Y. Tian (2015), Mechanisms for convection triggering by cold pools, *Geophys. Res. Lett.*, *42*(6), 1943–1950, doi:10.1002/2015GL063227.

VanZanten, M. C., B. Stevens, L. Nuijens, A. P. Siebesma, A. S. Ackerman, F. Burnet, A. Cheng, F. Couvreux, H. Jiang, M. Khairoutdinov, Y. Kogan, D. C. Lewellen, D. Mechem, K. Nakamura, A. Noda, B. J. Shipway, J. Slawinska, S. Wang, and A. Wyszogrodzki (2011), Controls on precipitation and cloudiness in simulations of trade-wind cumulus as observed during RICO, *J. Adv. Model. Earth Syst.*, *3*(2), doi: 10.1029/2011MS000056.

Vial, J., J. L. Dufresne, and S. Bony (2013), On the interpretation of inter-model spread in CMIP5 climate sensitivity estimates, *Clim. Dyn.*, pp. 3339–3362, doi:10.1007/s00382-013-1725-9.

Vial, J., S. Bony, J.-L. Dufresne, and R. Roehrig (2016), Coupling between lower-tropospheric convective mixing and low-level clouds: Physical mechanisms and dependence on convection scheme, *J. Adv. Model. Earth Syst.*, *8*(4), 1892–1911, doi: 10.1002/2016MS000740.

Vial, J., S. Bony, B. Stevens, and R. Vogel (2017), Mechanisms and model diversity of trade-wind shallow cumulus cloud feedbacks: A review, *Surveys in Geophysics*, doi: 10.1007/s10712-017-9418-2.

von Salzen, K., N. McFarlane, and M. Lazare (2005), The role of shallow convection in the water and energy cycles of the atmosphere, *Climate Dynamics*, *25*(7-8), 671–688, doi:10.1007/s00382-005-0051-2.

Wilbanks, M. C., S. E. Yuter, S. P. De Szoeke, W. A. Brewer, M. A. Miller, A. M. Hall, and C. D. Burleyson (2015), Near-surface density currents observed in the southeast pacific stratocumulus-topped marine boundary layer, *Mon. Wea. Rev.*, *143*(9), 3532–3555.

Yanai, M., S. Esbensen, and J.-H. Chu (1973), Determination of Bulk Properties of Tropical Cloud Clusters from Large-Scale Heat and Moisture Budgets, *J. Atmos. Sci.*, *30*, 611–627.

Young, G. S., S. M. Perugini, and C. W. Fairall (1995), Convective Wakes in the Equatorial Western Pacific during TOGA, *Monthly Weather Review*, *123*, 110, doi:10.1175/1520-0493(1995)123¡0110:CWITEW¿2.0.CO;2.

Zängl, G., D. Reinert, P. Rípodas, and M. Baldauf (2015), The icon (icosahedral non-hydrostatic) modelling framework of dwd and mpi-m: Description of the non-hydrostatic dynamical core, *Quart. J. Roy.Meteor.Soc.*, *141*(687), 563–579.

Zhang, Y., B. Stevens, and M. Ghil (2005), On the diurnal cycle and susceptibility to aerosol concentration in a stratocumulus-topped mixed layer, *Quart. J. Roy.Meteor.Soc.*, *131*(608), 1567–1583, doi:10.1256/qj.04.103.

Zhao, M. (2014), An Investigation of the Connections among Convection, Clouds, and Climate Sensitivity in a Global Climate Model, *J. Climate*, *27*(5), 1845–1862, doi: 10.1175/JCLI-D-13-00145.1.

Zuidema, P., and G. Torri (2017), Precipitation-induced oceanic cold pools and their interactions with the larger-scale environment, submitted to *Surveys in Geophysics*.

Zuidema, P., Z. Li, R. J. Hill, L. Bariteau, B. Rilling, C. Fairall, W. A. Brewer, B. Albrecht, and J. Hare (2012), On Trade Wind Cumulus Cold Pools, *J. Atmos. Sci.*, *69*(1), 258–280, doi:10.1175/JAS-D-11-0143.1.

Acknowledgements

I enjoyed three stimulating, instructive and joyful years as a PhD candidate at the MPI owing to the interaction with colleagues from the institute and the atmospheric science community. Im very grateful to my advisor Louise Nuijens for all the support, inspiration and expertise, but also for a lot of freedom to develop and follow my own ideas. Thank you for providing me the opportunity to spend a stimulating visit at MIT—and for passing on your amazing flat to us.

I wish to thank my co-advisor Bjorn Stevens for asking challenging questions, for demonstrating that one can always discover interesting features when looking at the Barbados Blog, and for making the Atmosphere such a stimulating department. I thank Hartmut Grassl for being a dedicated panel chair. I would also like to thank Stefan Buehler for offering to officially review my thesis, and Johanna Baehr, Matthias Hort, and Felix Ament for the willingness to serve as committee members.

I would like to thank Paquita Zuidema for sharing her vast knowledge about cold pools and for serving as constructive reviewer of Chapter 2. I also thank Paquita and Brian for hosting me during my visit at RSMAS. I'm grateful to Sandrine Bony for making me aware of interesting differences between LES and GCM simulated low-cloud feedbacks, for sharing many good ideas, and for making sure that new challenges are awaiting. Axel Seifert is thanked for interesting discussions about the LES and for sharing his interactive radiation implementation, and James Ruppert is thanked for helpful suggestions regarding the WTG setup. I thank Linda Schlemmer for supporting my first steps with the LES and for advice on any aspect of modeling clouds and convection. I acknowledge Miguel Angel Izaguirre from the University of Miami for sharing the Ragged Point data. Many thanks go to Ann Kristin for reviewing parts of this thesis and for sharing this latex template. I'm also grateful to Jörg Burdanowitz and Juan-Pedro Mellado for providing feedback on parts of this thesis.

Many thanks go to the entire Barbados group for making this fantastic dataset available, and for supporting me in its use. I'm also grateful to Cathy Hohenegger and the HErZ group for letting me join their group meetings. Special thanks go to Stefan Kinne for providing me with the opportunity to join a research cruise aboard R/V Meteor, which allowed me to observe shallow cumulus clouds in their natural habitat. The IMPRS office and Christina Rieckers are thanked for all the organisational, mental, and financial

support. Thank you, Matthias and Katherine, for being great office mates.

I also very much thank Elly and Uwe for making me feel at home in Hamburg from the very beginning. I deeply thank my parents, my sister Rebekka, as well as Christoph, Maria, Toni and Livio for encouragement, support, and many visits in Hamburg and its surroundings. I'm especially grateful to Michael, for your love, for joining me in Hamburg, and for the wonderful Huismuisig.

List of Publications

Parts of this thesis have been published as scientific papers:

Chapter 2: **Vogel, R.**, L. Nuijens, and B. Stevens (2016), The role of precipitation and spatial organization in the response of trade-wind clouds to warming, *J. Adv. Model. Earth Syst.*, *8*(2), 843–862, doi:10.1002/2015MS000568.

Appendix B: Vial, J., S. Bony, B. Stevens, and **R. Vogel** (2017), Mechanisms and model diversity of trade-wind shallow cumulus cloud feedbacks: A review, Surveys in Geophysics, doi:10.1007/s10712-017-9418-2.

I further contributed analyses for the following paper:

Bony, S., B. Stevens, F. Ament, S. Bigorre, P. Chazette, S. Crewell, J. Delanoë, K. Emanuel, D. Farrell, C. Flamant, S. Gross, L. Hirsch, J. Karstensen, B. Mayer, L. Nuijens, J. H. Ruppert, I. Sandu, P. Siebesma, S. Speich, F. Szczap, J. Totems, **R. Vogel**, M. Wendisch, and M. Wirth (2017), EUREC^{4}A: A field campaign to elucidate the couplings between clouds, convection and circulation, *Surveys in Geophysics*, doi:10.1007/s10712-017-9428-0.

Eidesstattliche Versicherung

Declaration on oath

Hiermit erkläre ich an Eides statt, dass ich die vorliegende Dissertationsschrift selbst verfasst und keine anderen als die angegebenen Quellen und Hilfsmittel benutzt habe.

I hereby declare, on oath, that I have written the present dissertation by myself and have not used other than the acknowledged resources and aids.
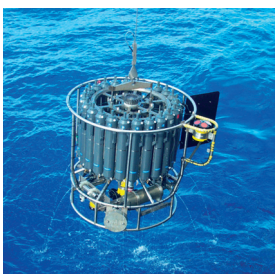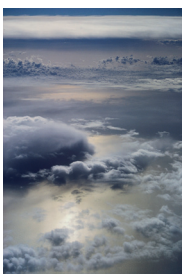
Hamburg, den 3. Mai 2017